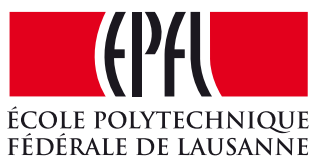


# **Measurement of time-dependent $CP$ violation in $B^0 \rightarrow D^\mp\pi^\mp$ decays and optimisation of Flavour Tagging algorithms at LHCb**

Thèse n. XXXX  
présentée le XX xxxx 2018  
à la Faculté des Sciences de Base  
Laboratoire de physique des hautes énergies  
Programme doctoral en Physique  
École Polytechnique Fédérale de Lausanne



pour l'obtention du grade de Docteur ès Sciences  
par

Vincenzo Battista

acceptée sur proposition du jury:  
Prof. Olivier Schneider, directeur de thèse

Lausanne, EPFL, 2018



*The ability to quote is a serviceable substitute for wit*  
W. S. Maugham



# Abstract

Keywords:  $B$  physics, LHCb, LHC.



# Résumé

Mots clefs : Physique du  $B$ , LHCb, LHC.



# Sommario

Parole chiave: fisica del mesone  $B$ , LHCb, LHC.



# Acknowledgements

*Lausanne, XX XXXX 2018*

V. B.



# Contents

<b>Abstract (English/Français/Italian)</b>	<b>v</b>
<b>Acknowledgements</b>	<b>xi</b>
<b>1 The Standard Model of particle physics and <math>B</math> physics</b>	<b>1</b>
1.1 The Standard Model of particle physics . . . . .	2
1.2 The Cabibbo-Kobayashi-Maskawa matrix . . . . .	4
1.3 Physics of neutral $B$ mesons . . . . .	7
1.3.1 Oscillation of neutral mesons . . . . .	7
1.3.2 Decay of neutral mesons . . . . .	9
1.3.3 CP-violation in neutral meson systems . . . . .	11
<b>2 The Large Hadron Collider and the LHCb experiment</b>	<b>15</b>
2.1 The Large Hadron Collider . . . . .	16
2.2 The LHCb experiment . . . . .	18
2.2.1 The tracking system . . . . .	19
2.3 Particle Identification (PID) . . . . .	22
2.3.1 The trigger system . . . . .	24
2.3.2 Event reconstruction, simulation and software . . . . .	27
2.3.3 Data collected by LHCb . . . . .	28
<b>3 Flavour Tagging algorithms and optimisation of the opposite-side electron tagger</b>	<b>31</b>
<b>4 Measurement of CP violation in <math>B^0 \rightarrow D^\mp \pi^\pm</math> decays</b>	<b>33</b>
4.1 Introduction . . . . .	34
4.2 Data sample and selection . . . . .	36
4.2.1 Stripping and trigger requirements . . . . .	36
4.2.2 Preselection and samples definition . . . . .	37
4.2.3 Vetoos for physics backgrounds . . . . .	38
4.2.4 Wrongly associated PVs . . . . .	41
4.2.5 Development of an MVA classifier . . . . .	43
4.2.6 BDT selection optimisation . . . . .	45
4.2.7 Multiple candidates . . . . .	45

## Contents

---

4.2.8	Selection performance . . . . .	46
4.3	Simulation and expected sample composition . . . . .	48
4.3.1	PIDK correction . . . . .	48
4.3.2	Surviving physics backgrounds . . . . .	49
4.4	Fits to the $B^0$ invariant mass . . . . .	51
4.4.1	Probability density functions . . . . .	52
4.4.2	Fit to data . . . . .	53
4.4.3	$sWeight$ calculation . . . . .	57
4.4.4	Fit split by subsample . . . . .	59
<b>Appendix</b>		<b>63</b>
4.5	Selection studies . . . . .	64
4.5.1	BDT input features . . . . .	64
4.5.2	Multiple candidates . . . . .	64
4.6	Particle Identification plots . . . . .	68
4.7	Invariant mass fit studies . . . . .	71
4.8	PDFs definitions . . . . .	72
References	. . . . .	74

# 1 The Standard Model of particle physics and $B$ physics

### 1.1 The Standard Model of particle physics

The *Standard Model* (SM) of particle physics [1, 2, 3] is a *non-abelian, Yang-Mills quantum field theory* based on the  $SU(3) \times SU(2) \times U(1)$  gauge symmetry group. This model provides a coherent, unified and experimentally-established picture of electromagnetic, weak and strong interactions, as well as a description of the known elementary particles (quarks, leptons, gauge bosons and Higgs boson, Fig. 1.1).

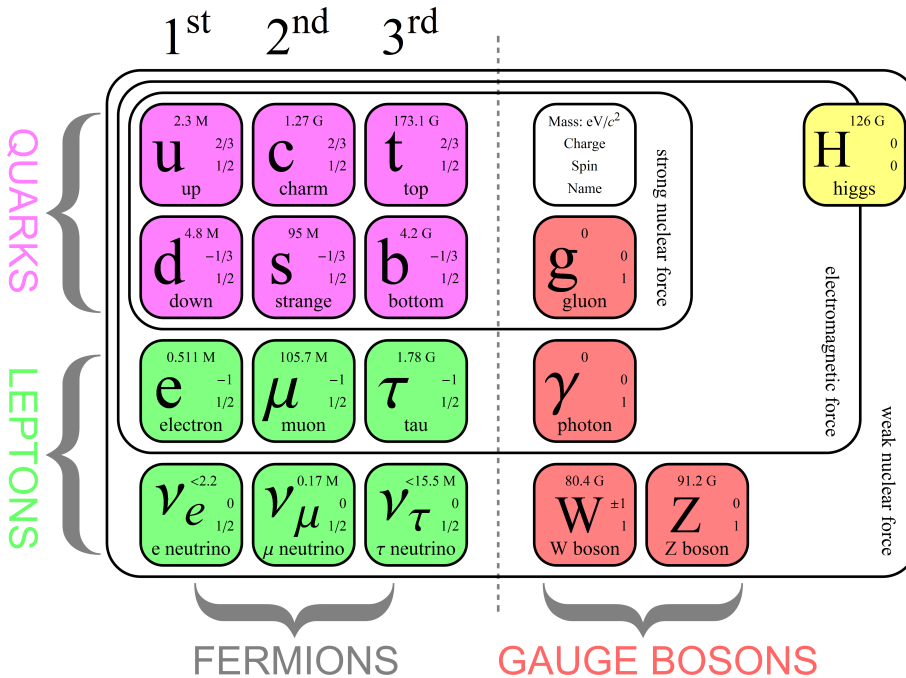


Figure 1.1 – Elementary particles described by the SM.

All particles are either *fermions* or *bosons*. The fermions (leptons, quarks) have half-integer spin and follow the Fermi-Dirac statistics [4, 5], whereas Bosons (gauge bosons, Higgs boson) have integer spin and follow the Bose-Einstein statistics [6].

Leptons (spin- $\frac{1}{2}$ ) include three charged <sup>1</sup>, massive particles (electron  $e^-$ , muon  $\mu^-$  and tau  $\tau^-$ ), which interact via the electromagnetic and weak interactions, and three neutral, (nearly) massless particles, called *neutrinos* ( $\nu_e$ ,  $\nu_\mu$  and  $\nu_\tau$ ), which only experience weak interactions.

Six different types of quarks (spin- $\frac{1}{2}$ ) exist: the *up-type* quarks up ( $u$ ), charm ( $c$ ) and top/truth ( $t$ ), having charge  $\frac{2}{3}$ , and the *down-type* quarks down ( $d$ ), strange ( $s$ ), and bottom/beauty ( $b$ ), which have charge  $-\frac{1}{3}$ . They can interact via electromagnetic, weak and strong interactions, and they are all massive.

<sup>1</sup>Electric charge is always intended in units of the fundamental charge of the electron

- 20 The fundamental interactions are *mediated* by gauge bosons (spin-1). The photon ( $\gamma$ ) is  
21 responsible for the electromagnetic interaction, whereas  $Z^0$  and  $W^\pm$  bosons are mediators  
22 for the weak interaction. These two forces are considered to be different manifestations  
23 of a single *electroweak* interaction, which is responsible for all electric and magnetic  
24 phenomena as well as some radioactive decays. The strong interaction among quarks is  
25 mediated by the gluons  $g$ . Photon and gluons are massless, whereas the weak force gauge  
26 bosons have a non-zero mass.
- 27 For all the particles mentioned so far, an *antiparticle* exist. Each antiparticle has the  
28 same mass of the corresponding particle, but opposite quantum numbers (electric charge,  
29 lepton number etc...).
- 30 Quarks do not exist in a free state: they can only be bound inside *hadrons* via the  
31 *confinement* mechanism, a feature of the strong interaction. A hadron can be composed  
32 by a quark-antiquark pair (*meson*), or by three quarks or antiquarks (*baryons*). Examples  
33 of mesons include the  $B^0$  ( $\bar{b}d$ ) and  $D^+$  ( $c\bar{d}$ ) mesons, whereas proton ( $uud$ ) and neutron  
34 ( $udd$ ) are examples of baryons. Recently, there have been evidences for more complex  
35 states (tetraquarks [7], pentaquarks [8]).
- 36 The non-zero mass of leptons, quarks and weak force gauge bosons would require a  
37 gauge symmetry breaking term in the SM Lagrangian density. The *Brout-Englert-Higgs*  
38 *mechanism* [9, 10, 11] introduces a scalar (spin-0) field, called Higgs field, and a potential  
39 which allows the Higgs field to have a non-zero vacuum expectation value. This implies  
40 that the Gauge symmetry is broken *dynamically*, and that the masses of the particles  
41 arise from the resulting interaction with the Higgs field. The quantum of the Higgs field  
42 is known as Higgs boson, the last SM particle to be discovered experimentally [12, 13].
- 43 All massive particles experience the fourth fundamental interaction, the gravitational  
44 force, but this is described by another field theory, the General Relativity (GR), currently  
45 not unified with the SM.
- 46 Any experimental signature that is not described by the SM would be a hint for *new*  
47 *physics* (NP). Altought the SM is known to be an incomplete theory because of different  
48 unsolved problems, such as dark matter, *naturalness*, matter-antimatter asymmetry, lack  
49 of SM-GR unification etc..., no evidence for NP has been found so far.

<sup>50</sup> **1.2 The Cabibbo-Kobayashi-Maskawa matrix**

The lagrangian density describing the interactions between quarks and  $W^\pm$  (*charged current interaction*) can be written as follows:

$$\mathcal{L}_{cc} = \frac{g}{\sqrt{2}} \begin{pmatrix} \bar{u} & \bar{c} & \bar{t} \end{pmatrix} V_{CKM} \gamma^\mu \frac{(1 - \gamma^5)}{2} \begin{pmatrix} d \\ s \\ b \end{pmatrix} W_\mu^+ + h.c., \quad (1.1)$$

where  $g$  is a coupling constant,  $\gamma^\mu$  are Dirac matrices and  $V_{CKM}$ , known as Cabibbo-Kobayashi-Maskawa (CKM) matrix [14, 15], couples the *flavour* eigenstates  $d$ ,  $s$  and  $b$  to the *mass* (or *physical*) eigenstates  $d'$ ,  $s'$  and  $b'$ :

$$V_{CKM} = \begin{pmatrix} V_{ud} & V_{us} & V_{ub} \\ V_{cd} & V_{cs} & V_{cb} \\ V_{td} & V_{ts} & V_{tb} \end{pmatrix}. \quad (1.2)$$

- <sup>51</sup> The CKM matrix is unitary ( $V_{CKM}^\dagger V_{CKM} = 1$ ), so it can be written in terms of four  
<sup>52</sup> independent parameters, namely three angles and a *weak phase*  $\delta$ . The latter is the  
<sup>53</sup> source of all *CP-violating* phenomena in the SM, i.e. asymmetries between particles and  
<sup>54</sup> anti-particles; in fact, the *complexity* of  $V_{CKM}$  implies that the SM lagrangian density is  
<sup>55</sup> non CP-invariant, in agreement with the experimentally observed CP-violation.

A first, standard parameterisation of the CKM matrix [16] gives:

$$V_{CKM} = \begin{pmatrix} c_{12}c_{13} & s_{12}c_{13} & s_{13}e^{-i\delta} \\ -s_{12}c_{23} - c_{12}s_{23}s_{13}e^{i\delta} & c_{12}c_{23} - s_{12}s_{23}s_{13}e^{i\delta} & s_{23}c_{13} \\ s_{12}s_{23} - c_{12}c_{23}s_{13}e^{i\delta} & -c_{12}s_{23} - s_{12}c_{23}s_{13}e^{i\delta} & c_{23}c_{13} \end{pmatrix}, \quad (1.3)$$

- <sup>56</sup> where  $s_{ij} = \sin \theta_{ij}$  and  $c_{ij} = \cos \theta_{ij}$ .

Another, useful parameterisation is given by *Wolfenstein* [17] and points out the order of magnitude of each matrix element. By defining the following quantities:

$$s_{12} = \lambda = \frac{|V_{us}|}{\sqrt{|V_{ud}|^2 + |V_{us}|^2}}, \quad s_{23} = A\lambda^2 = A \left| \frac{V_{cb}}{V_{us}} \right|, \quad (1.4)$$

$$s_{13}e^{i\delta} = V_{ub}^* = A\lambda^3(\rho + i\eta), \quad (1.5)$$

the matrix  $V_{CKM}$  can be rewritten as a series expansion in powers of  $\lambda$ , given that  $\lambda$  is a small number:

$$V_{CKM} = \begin{pmatrix} 1 - \lambda^2/2 & \lambda & A\lambda^3(\rho - i\eta) \\ -\lambda & 1 - \lambda^2/2 & A\lambda^2 \\ A\lambda^3(1 - \rho - i\eta) & -A\lambda^2 & 1 \end{pmatrix} + \mathcal{O}(\lambda^4). \quad (1.6)$$

- 57 From 1.6, one can see that quark transitions within the same family (e.g.  $u \rightarrow d$ ) are more  
 58 probable, whereas transitions between different families (e.g.  $b \rightarrow c$ ) are more suppressed.  
 59 CP-violation is a consequence of  $\eta \neq 0$ .

The unitarity condition  $V_{\text{CKM}}^\dagger V_{\text{CKM}} = 1$  can be rewritten in terms of six scalar equations. Two of them are particularly relevant for the  $b$ -hadrons phenomenology:

$$V_{ud}V_{ub}^* + V_{cd}V_{cb}^* + V_{td}V_{tb}^* = 0, \quad (1.7)$$

$$V_{us}V_{ub}^* + V_{cs}V_{cb}^* + V_{ts}V_{tb}^* = 0. \quad (1.8)$$

These two equations can be graphically represented as *triangles* in the  $(\bar{\rho}, \bar{\eta})$  complex plane. Having defined the following angles:

$$\alpha = \phi_2 = \arg \left[ -\frac{V_{td}V_{tb}^*}{V_{ud}V_{ub}^*} \right], \quad \beta = \phi_1 = \arg \left[ -\frac{V_{cd}V_{cb}^*}{V_{td}V_{tb}^*} \right], \quad (1.9)$$

$$\gamma = \phi_3 = \arg \left[ -\frac{V_{ud}V_{ub}^*}{V_{cd}V_{cb}^*} \right], \quad \beta_s = \chi = \arg \left[ -\frac{V_{cb}V_{cs}^*}{V_{tb}V_{ts}^*} \right]. \quad (1.10)$$

- 60 the triangles given by Eq. 1.7 and Eq. 1.8 can be depicted as shown in Fig. 1.2. The first  
 61 triangle, defined by Eq. 1.7, is known as *Unitarity Triangle* (UT) and its elements can  
 62 be measured from analyses of  $B^0$  and  $B^\pm$  decays. The other triangle (Eq. 1.8) can be  
 63 studied from decays of  $B_s^0$  mesons. These measurements allow to test the CKM paradigm  
 64 for CP-violation in the SM. Any deviation from unitarity would be a signature of new  
 65 physics beyond the SM.

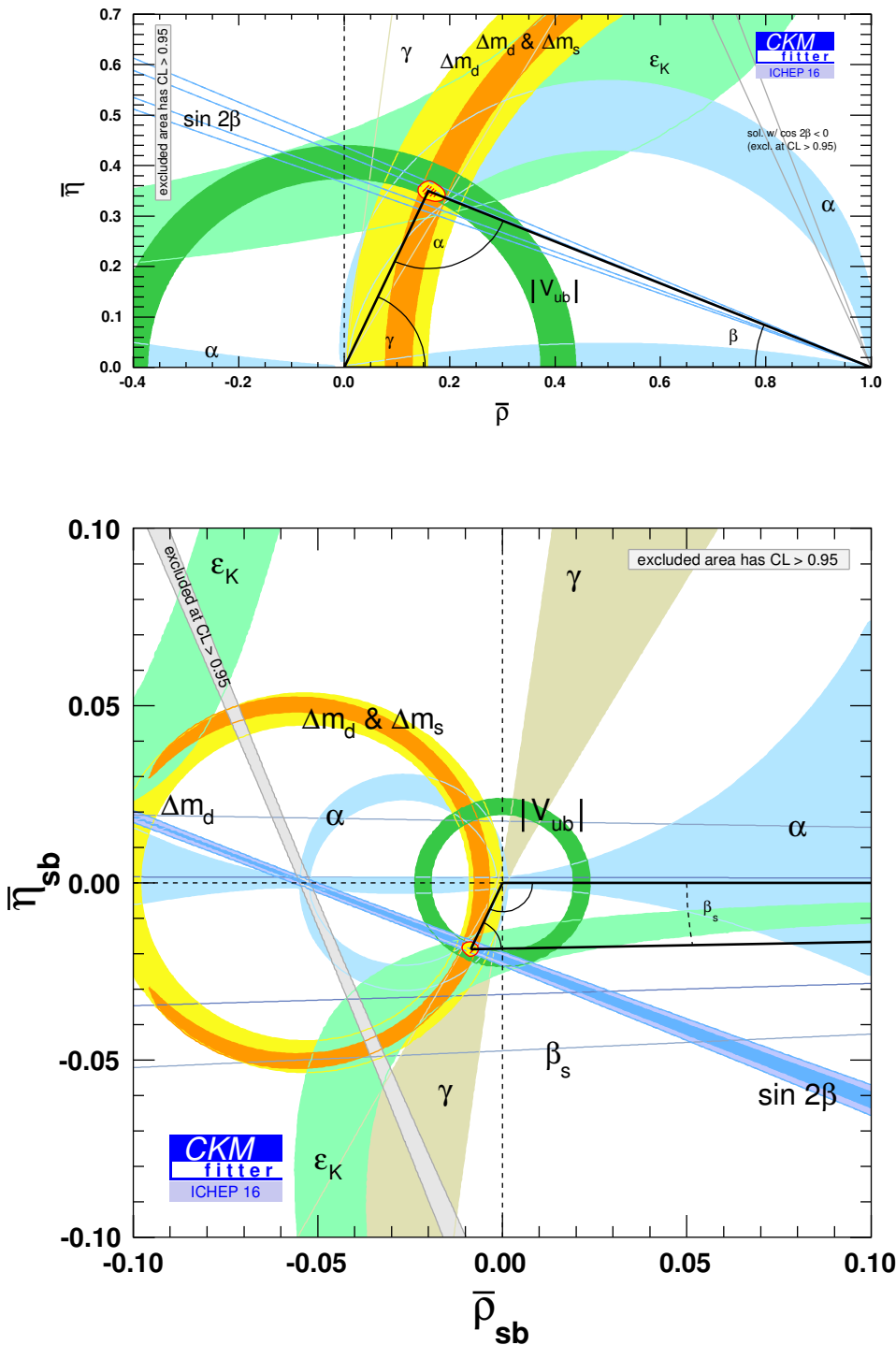


Figure 1.2 – Graphical representation of two of the six unitarity conditions of the CKM matrix, superimposed with the current experimental constraints [18].

---

## 66 1.3 Physics of neutral $B$ mesons

67 The theory of neutral  $B$  meson oscillation, decays and CP-violation presented here is  
 68 derived from Ref. [19] and [20].

### 69 1.3.1 Oscillation of neutral mesons

Neutral  $B$  meson states are characterised by the following quark content:

$$|B^0\rangle = |d\bar{b}\rangle, \quad |\bar{B}^0\rangle = |\bar{d}b\rangle, \quad (1.11)$$

$$|B_s^0\rangle = |s\bar{b}\rangle, \quad |\bar{B}_s^0\rangle = |\bar{s}b\rangle. \quad (1.12)$$

All neutral mesons will be denoted as  $P^0$  or  $\bar{P}^0$  hereafter. These states are eigenstates of the CP operator with eigenvalues  $\pm$  up to an arbitrary phase factor  $e^{i\phi_{CP}}$ . Since charged-currents do not conserve flavour quantum numbers (e.g. strangeness, beauty etc...), a neutral meson can transform itself into its own anti-meson, and viceversa. So, the time evolution of a neutral  $B$  meson system can be generally written as follows:

$$|\Psi(t)\rangle = a(t)|P^0\rangle + b(t)|\bar{P}^0\rangle + \sum_i c_i(t)|f_i\rangle, \quad (1.13)$$

70 where  $|f_i\rangle$  are all the possible final state, and  $c(0) = 0$  as initial condition.

Since the typical time scales of weak interactions are much longer than strong interaction timescales, we can neglect all weak interactions among final states (*Weisskopf-Wigner approximation*). So, we can write the Schroedinger equation for  $|\Psi(t)\rangle$  in terms of an effective, non-hermitian hamiltonian  $\mathcal{H}$ :

$$i\partial_t \begin{pmatrix} a(t) \\ b(t) \end{pmatrix} = \mathcal{H} \begin{pmatrix} a(t) \\ b(t) \end{pmatrix} = \begin{pmatrix} H_{11} & H_{12} \\ H_{21} & H_{22} \end{pmatrix} \begin{pmatrix} a(t) \\ b(t) \end{pmatrix}. \quad (1.14)$$

The  $\mathcal{H}$  matrix can be rewritten as the sum of two hermitian matrices  $M$  and  $\Gamma$ :

$$\mathcal{H} = M - \frac{i}{2}\Gamma = \begin{pmatrix} M_{11} & M_{12} \\ M_{21} & M_{22} \end{pmatrix} - \frac{i}{2} \begin{pmatrix} \Gamma_{11} & \Gamma_{12} \\ \Gamma_{21} & \Gamma_{22} \end{pmatrix}. \quad (1.15)$$

Assuming CPT-invariance ( $H_{11} = H_{22} = H_0$ ,  $M_{11} = M_{22} = M_0$ ,  $\Gamma_{11} = \Gamma_{22} = \Gamma_0$ ), the

eigenvalues of  $\mathcal{H}$  are:

$$\lambda_L = m_L - \frac{i}{2}\Gamma_L = H_0 + \sqrt{H_{12}H_{21}} = H_0 + \sqrt{\left(M_{12} - \frac{i}{2}\Gamma_{12}\right)\left(M_{12}^* - \frac{i}{2}\Gamma_{12}^*\right)}, \quad (1.16)$$

$$\lambda_H = m_H - \frac{i}{2}\Gamma_H = H_0 - \sqrt{H_{12}H_{21}} = H_0 - \sqrt{\left(M_{12} - \frac{i}{2}\Gamma_{12}\right)\left(M_{12}^* - \frac{i}{2}\Gamma_{12}^*\right)}. \quad (1.17)$$

where L ("light") and H ("heavy") refer to the value of the mass for each eigenstate. The corresponding eigenvectors are:

$$|P_L\rangle = p|P^0\rangle + q|\bar{P}^0\rangle, \quad |P_H\rangle = p|P^0\rangle - q|\bar{P}^0\rangle \quad (1.18)$$

where  $p$  and  $q$  satisfy  $|p|^2 + |q|^2 = 1$  and are given by:

$$\frac{q}{p} = \sqrt{\frac{H_{21}}{H_{12}}} = \sqrt{\frac{M_{21} - \frac{i}{2}\Gamma_{21}}{M_{12} - \frac{i}{2}\Gamma_{12}}} = \sqrt{\frac{M_{21}^* - \frac{i}{2}\Gamma_{21}^*}{M_{12}^* - \frac{i}{2}\Gamma_{12}^*}}. \quad (1.19)$$

It can be shown that, assuming CP-violation in weak interactions and choosing  $\phi_{\text{CP}} = \pi$ , we have:

$$M_{12} = |M_{12}|e^{i\phi_M}, \quad \Gamma_{12} = |\Gamma_{12}|e^{i(\phi_L - \pi)}, \quad (1.20)$$

where  $\phi_M$  and  $\phi_\Gamma$  are extra phases (*mixing* and *decay* phases respectively) appearing because of CP-violation:

$$M_{12} = M_{12}^*e^{2i\phi_M}, \quad \Gamma_{12} = \Gamma_{12}^*e^{2i\phi_\Gamma}. \quad (1.21)$$

For the neutral  $B$  meson system, the ratio  $|\Gamma_{12}/M_{12}|$  is expected to be small in the SM; as a consequence, it can be shown that

$$\frac{q}{p} = -e^{-i\phi_M} \left[ 1 - \frac{1}{2} \left| \frac{\Gamma_{12}}{M_{12}} \right| \sin(\phi_M - \phi_\Gamma) + \mathcal{O} \left( \left| \frac{\Gamma_{12}}{M_{12}} \right|^2 \right) \right], \quad (1.22)$$

<sup>71</sup> where  $\phi_M - \phi_\Gamma = 0 + \mathcal{O}(m_c^2/m_b^2)$ .

The difference and the average of mass and width between mass eigenstates can be defined as:

$$\Delta m = m_H - m_L = \Re(\lambda_H - \lambda_L), \quad m = \frac{m_L + m_H}{2} = \frac{\Re(\lambda_H + \lambda_L)}{2}, \quad (1.23)$$

$$\Delta\Gamma = \Gamma_L - \Gamma_H = -2\Im(\lambda_L - \lambda_H), \quad \Gamma = \frac{\Gamma_L + \Gamma_H}{2} = -\frac{\Im(\lambda_H + \lambda_L)}{4}. \quad (1.24)$$

- <sup>72</sup> The sign convention for  $\Delta\Gamma$  is chosen to have a positive-definite experimental value for  
<sup>73</sup> the  $B_s^0$  system (for  $B^0$ , experiments give a result compatible with zero, in agreement with  
<sup>74</sup> the SM).

The time evolution of the states  $|P^0(t)\rangle$  and  $|\bar{P}^0(t)\rangle$  when they are initially produced as  $|P^0(0)\rangle$  and  $|\bar{P}^0(0)\rangle$  can be obtained from the effective hamiltonian:

$$|P^0(t)\rangle = g_+(t)|P^0(t)\rangle + \frac{q}{p}g_-(t)|\bar{P}^0(t)\rangle, \quad (1.25)$$

$$|\bar{P}^0(t)\rangle = g_+(t)|\bar{P}^0(t)\rangle + \frac{p}{q}g_-(t)|P^0(t)\rangle. \quad (1.26)$$

$$(1.27)$$

The functions  $g_{\pm}(t)$  are built in terms of the eigenvalues:

$$g_{\pm} = \frac{1}{2} \left( e^{-im_H t - \frac{1}{2}\Gamma_H t} \pm e^{-im_L t - \frac{1}{2}\Gamma_L t} \right). \quad (1.28)$$

The probabilities that a state initially produced as  $|P^0(0)\rangle$  or  $|\bar{P}^0(0)\rangle$  becomes a  $|P^0(t)\rangle$  or  $|\bar{P}^0(t)\rangle$  are the following:

$$|\langle P^0(0)|P^0(t)|\rangle|^2 = |g_+(t)|^2 = \frac{e^{-\Gamma t}}{2} \left( \cosh \frac{\Delta\Gamma t}{2} + \cos \Delta m t \right), \quad (1.29)$$

$$|\langle \bar{P}^0(0)|P^0(t)|\rangle|^2 = \left| \frac{q}{p} \right|^2 |g_-(t)|^2 = \left| \frac{q}{p} \right|^2 \frac{e^{-\Gamma t}}{2} \left( \cosh \frac{\Delta\Gamma t}{2} - \cos \Delta m t \right), \quad (1.30)$$

$$|\langle P^0(0)|\bar{P}^0(t)|\rangle|^2 = \left| \frac{p}{q} \right|^2 |g_-(t)|^2 = \left| \frac{p}{q} \right|^2 \frac{e^{-\Gamma t}}{2} \left( \cosh \frac{\Delta\Gamma t}{2} - \cos \Delta m t \right), \quad (1.31)$$

$$|\langle \bar{P}^0(0)|\bar{P}^0(t)|\rangle|^2 = |g_+(t)|^2 = \frac{e^{-\Gamma t}}{2} \left( \cosh \frac{\Delta\Gamma t}{2} + \cos \Delta m t \right). \quad (1.32)$$

- <sup>75</sup> The equations above describe the *oscillation* or *mixing* of two neutral mesons.

### 1.3.2 Decay of neutral mesons

The amplitude for the decay of a neutral meson into a final state  $f$  can be obtained from the effective hamiltonian  $\mathcal{H}$ :

$$A_f = \langle f | \mathcal{H} | P^0 \rangle, \quad \bar{A}_f = \langle f | \mathcal{H} | \bar{P}^0 \rangle, \quad (1.33)$$

$$A_{\bar{f}} = \langle \bar{f} | \mathcal{H} | P^0 \rangle, \quad \bar{A}_{\bar{f}} = \langle \bar{f} | \mathcal{H} | \bar{P}^0 \rangle. \quad (1.34)$$

After defining the following parameters:

$$\lambda_f = \frac{q}{p} \frac{\bar{A}_f}{A_f}, \quad \frac{1}{\bar{\lambda}_{\bar{f}}} = \lambda_{\bar{f}} = \frac{q}{p} \frac{\bar{A}_{\bar{f}}}{A_{\bar{f}}}, \quad (1.35)$$

is it possible to write the *decay rates* for neutral mesons decaying into  $f$  or  $\bar{f}$ :

$$\begin{aligned} \frac{d\Gamma(P^0 \rightarrow f)}{dt}(t) = N_f |A_f|^2 \frac{1 + |\lambda_f|^2}{2} e^{-\Gamma t} \\ \left[ \cosh\left(\frac{\Delta\Gamma t}{2}\right) + D_f \sinh\left(\frac{\Delta\Gamma t}{2}\right) + C_f \cos(\Delta m t) - S_f \sin(\Delta m t) \right], \end{aligned} \quad (1.36)$$

$$\begin{aligned} \frac{d\Gamma(\bar{P}^0 \rightarrow f)}{dt}(t) = N_f |A_f|^2 \left| \frac{p}{q} \right|^2 \frac{1 + |\lambda_f|^2}{2} e^{-\Gamma t} \\ \left[ \cosh\left(\frac{\Delta\Gamma t}{2}\right) + D_f \sinh\left(\frac{\Delta\Gamma t}{2}\right) - C_f \cos(\Delta m t) + S_f \sin(\Delta m t) \right], \end{aligned} \quad (1.37)$$

$$\begin{aligned} \frac{d\Gamma(P^0 \rightarrow \bar{f})}{dt}(t) = N_f |\bar{A}_{\bar{f}}|^2 \left| \frac{q}{p} \right|^2 \frac{1 + |\bar{\lambda}_{\bar{f}}|^2}{2} e^{-\Gamma t} \\ \left[ \cosh\left(\frac{\Delta\Gamma t}{2}\right) + D_{\bar{f}} \sinh\left(\frac{\Delta\Gamma t}{2}\right) - C_{\bar{f}} \cos(\Delta m t) + S_{\bar{f}} \sin(\Delta m t) \right], \end{aligned} \quad (1.38)$$

$$\begin{aligned} \frac{d\Gamma(\bar{P}^0 \rightarrow \bar{f})}{dt}(t) = N_f |\bar{A}_{\bar{f}}|^2 \frac{1 + |\bar{\lambda}_{\bar{f}}|^2}{2} e^{-\Gamma t} \\ \left[ \cosh\left(\frac{\Delta\Gamma t}{2}\right) + D_{\bar{f}} \sinh\left(\frac{\Delta\Gamma t}{2}\right) + C_{\bar{f}} \cos(\Delta m t) - S_{\bar{f}} \sin(\Delta m t) \right]. \end{aligned} \quad (1.39)$$

where  $N_f$  is a time-independent normalisation factor and

$$D_f = -\frac{2\Re\lambda_f}{1 + |\lambda_f|^2}, \quad C_f = \frac{1 - |\lambda_f|^2}{1 + |\lambda_f|^2}, \quad S_f = \frac{2\Im\lambda_f}{1 + |\lambda_f|^2}, \quad (1.40)$$

$$D_{\bar{f}} = -\frac{2\Re\bar{\lambda}_{\bar{f}}}{1 + |\bar{\lambda}_{\bar{f}}|^2}, \quad C_{\bar{f}} = \frac{1 - |\bar{\lambda}_{\bar{f}}|^2}{1 + |\bar{\lambda}_{\bar{f}}|^2}, \quad S_{\bar{f}} = \frac{2\Im\bar{\lambda}_{\bar{f}}}{1 + |\bar{\lambda}_{\bar{f}}|^2}. \quad (1.41)$$

<sup>77</sup> are known as *CP-coefficients*.

<sup>78</sup> 1.3.3 CP-violation in neutral meson systems

<sup>79</sup> Three types of CP-violation can occur. They are briefly sketched in Fig. 1.3 and described  
<sup>80</sup> in the following paragraphs.

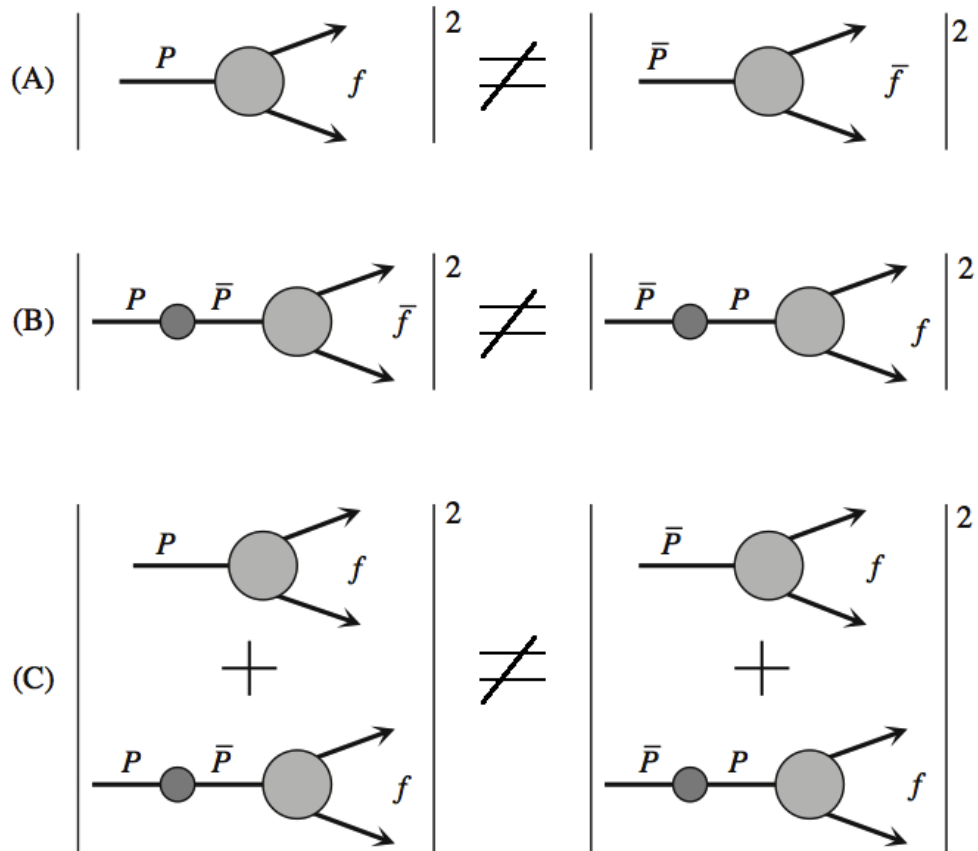


Figure 1.3 – Graphical representation of CP-violation in decay (A), mixing (B) and interference between mixing and decay (C) [20].

<sup>81</sup> CP-violation in decays

CP violation in decays, also known as *direct* CP violation, happens when the decay amplitude for  $P \rightarrow f$  is different from the CP-conjugated process  $\bar{P} \rightarrow \bar{f}$ :

$$\left| \frac{\bar{A}_{\bar{f}}}{A_f} \right| \neq 1. \quad (1.42)$$

This kind of CP-violation occurs if, for each decay, at least two amplitudes with different weak ( $\phi_j$ ) and strong ( $\delta_j$ ) phases contribute:

$$A_f = \sum_j |A_j| e^{i(\delta_j + \phi_j)}, \quad \bar{A}_{\bar{f}} = \sum_j |\bar{A}_j| e^{i(\delta_j - \phi_j)}. \quad (1.43)$$

In fact, the strong phases are invariant under CP-conjugation, whereas the weak phases get the opposite sign. The following asymmetry between final states can be measured to determine direct CP-violation experimentally for *charged mesons*, where mixing effects are absent:

$$\mathcal{A}_{f^\pm} = \frac{\Gamma(P^- \rightarrow f^-) - \Gamma(P^+ \rightarrow f^+)}{\Gamma(P^- \rightarrow f^-) + \Gamma(P^+ \rightarrow f^+)} = \frac{\left| \frac{\bar{A}_{\bar{f}}}{A_f} \right|^2 - 1}{\left| \frac{\bar{A}_{\bar{f}}}{A_f} \right|^2 + 1} \quad (1.44)$$

### 82 CP-violation in mixing

CP-violation in mixing, also called *indirect* CP violation, occurs when the oscillation rate for  $\bar{P}^0 \rightarrow P^0$  is different from the CP-conjugated process  $P^0 \rightarrow \bar{P}^0$ . These two oscillation probabilities are given by Eq. 1.30 and Eq. 1.31 respectively. It turns out that they are identical unless

$$\left| \frac{q}{p} \right| \neq 1. \quad (1.45)$$

From Eq. 1.22, it can be seen that CP violation in mixing occurs when the relative phase  $\phi_M - \phi_\Gamma$  is different from any multiple of  $\pi$ . It is possible to measure the  $|q/p|$  ratio by comparing the oscillation rates in semileptonic decays of neutral mesons  $P^0 \rightarrow l^+ X$  and  $\bar{P}^0 \rightarrow l^- X$ , where no direct CP violation occurs. The decays where oscillation occurred are identified by reconstructing "wrong sign" leptons:

$$\mathcal{A}_{SL} = \frac{\frac{d\Gamma(\bar{P}^0 \rightarrow l^+ X)}{dt} - \frac{d\Gamma(P^0 \rightarrow l^- X)}{dt}}{\frac{d\Gamma(\bar{P}^0 \rightarrow l^+ X)}{dt} + \frac{d\Gamma(P^0 \rightarrow l^- X)}{dt}} = \frac{1 - |q/p|^4}{1 + |q/p|^4} \quad (1.46)$$

### 83 CP-violation in the interference between mixing and decay

This type of decay occurs when a neutral meson can decay directly to a given final state,  $P^0 \rightarrow f$ , or via a mixing,  $P^0 \rightarrow \bar{P}^0 \rightarrow f$ . This can happen only if the final state  $f$  is common to both  $P^0$  and  $\bar{P}^0$ . This type of CP-violation can occur also if other sources of CP-violation (mixing or decay) are absent. In general, the interference between mixing

and decay can be accessed by studying the following asymmetries:

$$\mathcal{A}_f(t) = \frac{\frac{d\Gamma(P^0 \rightarrow f)}{dt} - \frac{d\Gamma(\bar{P}^0 \rightarrow f)}{dt}}{\frac{d\Gamma(P^0 \rightarrow f)}{dt} + \frac{d\Gamma(\bar{P}^0 \rightarrow f)}{dt}} \quad (1.47)$$

$$\mathcal{A}_{\bar{f}}(t) = \frac{\frac{d\Gamma(P^0 \rightarrow \bar{f})}{dt} - \frac{d\Gamma(\bar{P}^0 \rightarrow \bar{f})}{dt}}{\frac{d\Gamma(P^0 \rightarrow \bar{f})}{dt} + \frac{d\Gamma(\bar{P}^0 \rightarrow \bar{f})}{dt}} \quad (1.48)$$

A relevant example is the case of neutral  $B$  mesons, where  $|q/p| = 1$ . Using Eq. 1.36, 1.37, 1.38 and 1.39, the asymmetries 1.47 and 1.48 take the following forms:

$$\mathcal{A}_f(t) = \frac{C_f \cos(\Delta m t) - S_f \sin(\Delta m t)}{\cosh\left(\frac{\Delta \Gamma t}{2}\right) + D_f \sinh\left(\frac{\Delta \Gamma t}{2}\right)}, \quad (1.49)$$

$$\mathcal{A}_{\bar{f}}(t) = \frac{-C_{\bar{f}} \cos(\Delta m t) + S_{\bar{f}} \sin(\Delta m t)}{\cosh\left(\frac{\Delta \Gamma t}{2}\right) + D_{\bar{f}} \sinh\left(\frac{\Delta \Gamma t}{2}\right)}. \quad (1.50)$$

<sup>84</sup> So, the CP-coefficients can be directly measured from a time-dependent analysis of the  $B$  decays.



## 2 The Large Hadron Collider and the <sup>87</sup> LHCb experiment

**2.1 The Large Hadron Collider**

The *Large Hadron Collider* (LHC) is a circular collider with a circumference of 26.66 Km. It's located at CERN, near Geneva, between Switzerland and France. The LHC is designed to produce proton-proton ( $pp$ ) collisions with a *luminosity* of  $10^{34} \text{ cm}^{-2}\text{s}^{-1}$  and a center of mass energy of 14 TeV. In the first data taking period before the first long shutdown, called Run 1 (2010-2012), the center of mass energy reached 7 TeV (2010-2011) and 8 TeV (2012).

The proton bunches, produced from hydrogen gas and made up with  $10^{11}$  protons, pass through different intermediate accelerating stages (Fig. 2.1):

- LINAC 2 (50 MeV);
- Proton Synchrotron Booster (1.4 GeV);
- Proton Synchrotron (25 GeV);
- Super Proton Synchroton (450 GeV).

Finally, they are injected clockwise and counter-clock wise into LHC and accelerated to their final energy. At LHC, in addition to LHCb, there are two general-purpose detectors (ATLAS and CMS), a detector dedicated to quark matter and quark-gluon plasma Physics (ALICE) and other smaller experiments (TOTEM, LHCf, MoEDAL) dedicated to different topics.

The LHC can also accelerate particles other than protons, such as lead or xenon, in order to collect data samples for specific studies.

## 2.1. The Large Hadron Collider

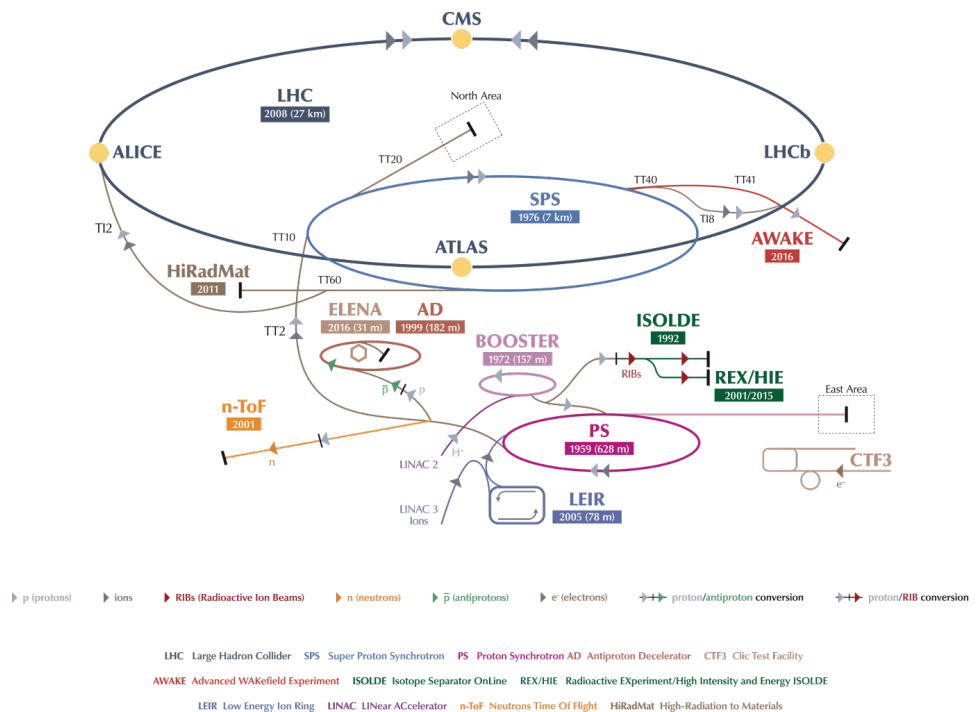


Figure 2.1 – Overview of the CERN accelerators complex.

<sup>108</sup>

## 2.2 The LHCb experiment

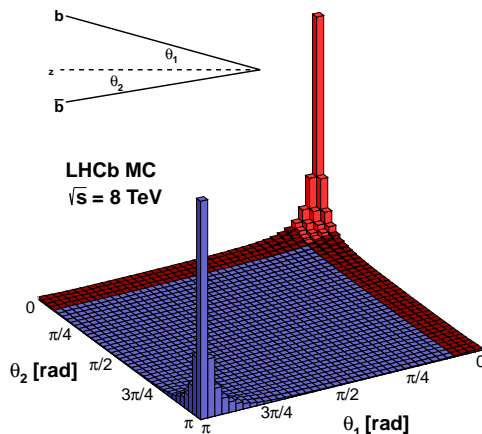
<sup>109</sup> The *Large Hadron Collider beauty* (LHCb) experiment [21] is a single-arm forward  
<sup>110</sup> spectrometer (see Fig. 2.3) that exploits the forward production of the  $b$ - and  $\bar{c}$ - quarks  
<sup>111</sup> pairs from  $pp$  collisions (Fig. 2.2). The LHCb angular coverage is comprised between  
<sup>112</sup> 15 mrad and 250 (300) mrad in the vertical (horizontal) plane. The LHCb coordinate  
<sup>113</sup> system consists of an orthogonal set of coordinates,  $x$ ,  $y$ ,  $z$ , where  $z$  is aligned with the  
<sup>114</sup> beam pipe,  $y$  is perpendicular to the LHCb cavern ground and  $x$  is orthogonal to the  
<sup>115</sup> other two.


Figure 2.2 –  $b$  and  $\bar{b}$  pair simulated production angles with respect to the beam direction at  $\sqrt{s} = 8 \text{ TeV}$ .

<sup>116</sup> The LHCb experiment is composed by different sub-detectors. The tracking system  
<sup>117</sup> includes a vertex and tracking detector called *VErtex LOcator* (VELO), the *Tracker*  
<sup>118</sup> *Turicensis* (TT), located upstream a magnetic dipole with an integrated field of 4 Tm, the  
<sup>119</sup> *Inner Tracker* (IT), situated downstream the magnet in three separated stations around  
<sup>120</sup> the beryllium beam-pipe, and the *Outer Tracker* (OT), installed in the same stations of  
<sup>121</sup> the IT. The *Particle IDentification* (PID) system comprises two *Ring Imaging CHerenkov*  
<sup>122</sup> detectors (RICH), an *Electromagnetic CALorimeter* (ECAL), which also includes a *Pre-*  
<sup>123</sup> *Showr* (PS) and *Scintillator Pad Detector* (SPD), a *Hadronic CALorimeter* (HCAL)  
<sup>124</sup> and five *muon detectors* (M1-M5).

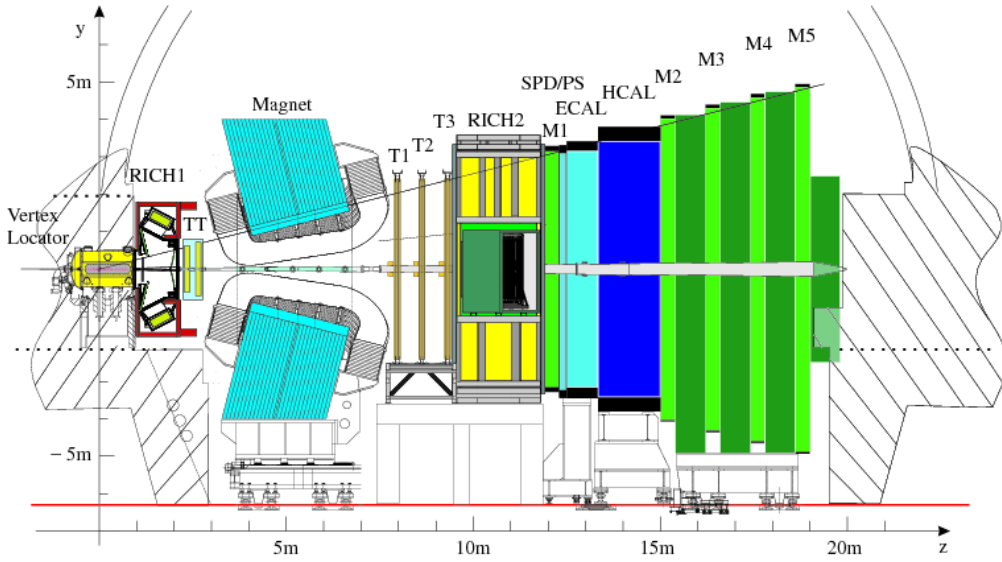


Figure 2.3 – Side view of the LHCb detector.

### <sup>125</sup> 2.2.1 The tracking system

#### <sup>126</sup> The VErtex LOcator (VELO)

<sup>127</sup> The VELO [22] (Fig. 2.4) is a silicon micro-strip detector for charged particles surrounding  
<sup>128</sup> the interaction point which identifies decay vertices and performs the first track recon-  
<sup>129</sup> struction step. The sensitive region of the VELO is composed of n-on-n silicon micro-strip  
<sup>130</sup> half-disk sensors with two different read-out strip geometries, called  $r$ -type and  $\phi$ -type,  
<sup>131</sup> which measure the radial ( $r$ ) and angular ( $\phi$ ) position in polar coordinates. The VELO  
<sup>132</sup> consists of 21 stations. Each station has two independent halves that can be moved apart  
<sup>133</sup> during the beam injection period and then closed again when the beam orbit is stabilised.  
<sup>134</sup> Each half-station is composed by one  $r$ -type and one  $\phi$ -type sensor. The total length of  
<sup>135</sup> the VELO detector is about 1 m.

<sup>136</sup> The silicon sensors, which provide an excellent measurement of vertex positions and  
<sup>137</sup> impact parameters (IP), are 8.4 cm in diameter and have an inner hole with radius  
<sup>138</sup> 0.8 cm. The IP resolution of a track is measured to be  $\sigma_{\text{IP}} = 11.6 \pm 23.4/p_T \mu\text{m}$  in  $x$  and  
<sup>139</sup>  $\sigma_{\text{IP}} = 11.2 \pm 23.2/p_T \mu\text{m}$  in  $y$ , where  $p_T$  is the *transverse momentum* (in  $\text{GeV}/c$ ) of the  
<sup>140</sup> particle with respect to the beam axis. The strip pitch ranges from 38 to 108  $\mu\text{m}$  (38 to  
<sup>141</sup> 97  $\mu\text{m}$ ) for  $r$  ( $\phi$ ) sensors, while the sensor thickness is 300  $\mu\text{m}$ .

#### <sup>142</sup> The Tracker Turicensis (TT)

<sup>143</sup> The TT [23] (Fig. 2.5) is a silicon micro-strip detector covering a total area of about  
<sup>144</sup>  $7.9 \text{ m}^2$  upstream the magnet and divided into two separate stations (TTa, TTb). Each

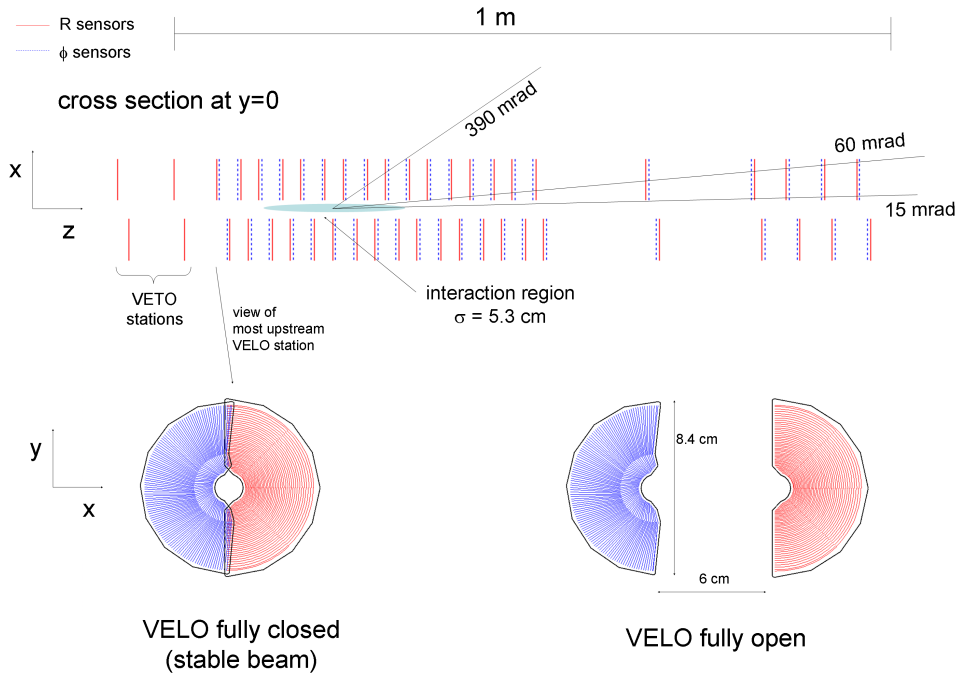


Figure 2.4 – Schematic overview of the VELO detector and its sensors.

station has two layers. The TT helps in improving the track momentum resolution and detecting long-lived particles that decay outside the VELO acceptance. TTa is composed by X-U layers, while TTb includes V-X layers. The X layers have read-out strips aligned vertically, whereas the U and V *stereo* layers are rotated by  $+5^\circ$  and  $-5^\circ$  with respect to the vertical in the  $xy$  plane, respectively.

The TT active area is made of p-on-n silicon micro-strip sensors. Since the sensors are exposed to a significant radiation due to a high track multiplicity, they are cooled to  $0^\circ$  in order to minimise the damage.

The TT read-out module contain from one to four sensors in a row, resulting in read-out strips up to 37 cm long. The strip pitch is 183  $\mu\text{m}$  and the sensor thickness is 500  $\mu\text{m}$ . The hit resolution is about 50  $\mu\text{m}$ .

### 156 The Inner Tracker (IT)

The IT [24] (Fig. 2.6) is also a silicon micro-strip detector. Together with the TT, it's a part of the *Silicon Tracker* (ST). It's dedicated to detect charged particles in the high track density region around the beam-pipe downstream the magnet. It's separated into three stations, where each station consists of four boxes. Each box has four layers made

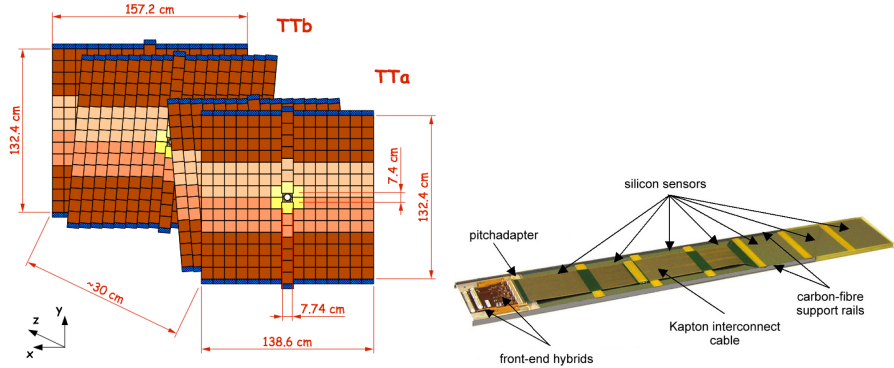


Figure 2.5 – Schematic overview of the TT stations/layers and one of the TT read-out modules.

of seven read-out modules arranged in a X1-U-V-X2 layout similar to that of the TT.  
The total coverage of the IT is about  $4.2 \text{ m}^2$ . The boxes directly above and below the beam-pipe are made of single-sensor modules, called *short modules*, whereas the remaining boxes are made of two bonded silicon sensor modules, called *long modules*. The IT strip pitch is  $198 \mu\text{m}$ , while the p-on-n sensor thickness is  $320$  ( $410$ )  $\mu\text{m}$  for the short (long) modules. The hit resolution is about  $50 \mu\text{m}$ .

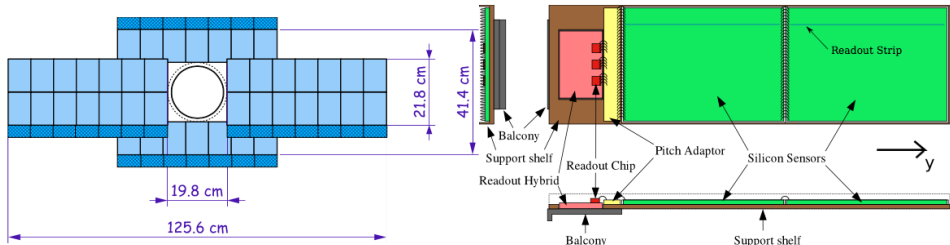


Figure 2.6 – Schematic overview of an IT station and one of the long IT read-out modules.

### 167 The Outer Tracker (OT)

The OT [25] (Fig. 2.8) is a gaseous straw-tube detector filled with an Ar/CO<sub>2</sub>/O<sub>2</sub> (70%/28.5%/1.5%) gas mixture. It's dedicated to the detection of charged particles in the low track density region outside the IT acceptance and covers a large area of about  $340 \text{ m}^2$ . The OT is composed by three stations, where each station has four layers in a X1-U-V-X2 configuration. Each station is separated physically for the left and right sides with respect to the beam-pipe into two C-frames (X1-U) and (V-X2). Each layer is divided into two mono-layers. The OT has different types of modules, the long F modules and the S1, S2, S3 modules that are cut in two pieces to leave space for the IT. The straw tube and anode wire diameters are 5 mm and  $25 \mu\text{m}$  respectively. The hit resolution is

<sup>177</sup> about 200 ?m.

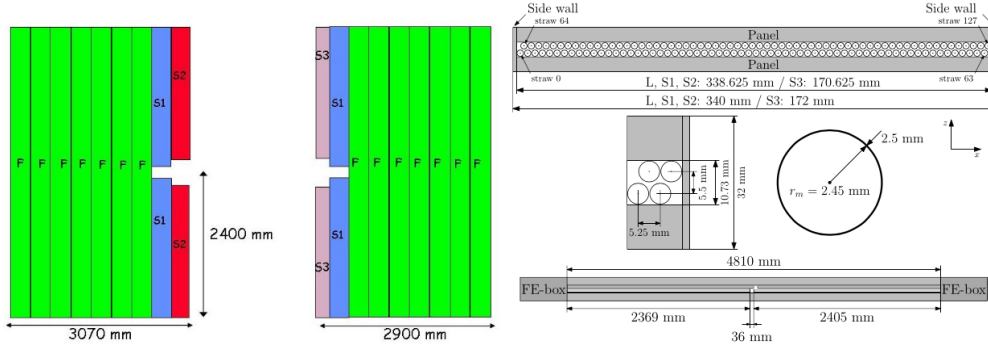


Figure 2.7 – Schematic overview of an OT layer and an OT module layout.

### <sup>178</sup> 2.3 Particle Identification (PID)

#### <sup>179</sup> The Ring Imaging CHerenkov (RICH) detectors

<sup>180</sup> When a charged particle is travelling faster than the speed of light in a medium, Cherenkov  
<sup>181</sup> light is produced at an angle that depends on the velocity of the particle and the refractive  
<sup>182</sup> index of the medium (*radiator*). By knowing the momentum from the tracker and the  
<sup>183</sup> velocity from the RICH detectors, the mass can be determined and therefore provide  
<sup>184</sup> particle identification. Two RICH detectors [26] (Fig. 2.9) are used in order to provide  
<sup>185</sup> PID in different momentum ranges.

<sup>186</sup> RICH1 is responsible for providing PID in the momentum range from 1 to 60 GeV/c. The  
<sup>187</sup> angular acceptance ranges from 25 mrad to 50 (300) mrad in the vertical (horizontal)  
<sup>188</sup> plane. The adopted radiator is a mixture of aerogel and fluorobutane (C<sub>4</sub>F<sub>10</sub>). RICH1 is  
<sup>189</sup> located between the VELO and the TT. The Cherenkov photons are guided to Hybrid  
<sup>190</sup> Photon Detectors (HPD) via dedicated mirrors.

<sup>191</sup> RICH2 is optimised for the momentum range from 15 to 100 GeV/c. The angular accept-  
<sup>192</sup> ance ranges from 15 mrad to 100 (120) mrad in the vertical (horizontal) plane where  
<sup>193</sup> most of the high-momentum tracks are produced. RICH2 uses tetrafluoromethane (CF<sub>4</sub>)  
<sup>194</sup> as radiator.

#### <sup>195</sup> The ELectrromagnetic CALorimeter (ECAL), Pre-Shower (PS) and Scintilla- <sup>196</sup> tor Pad Detector (SPD)

<sup>197</sup> The ECAL [27] is used for the detection and measurement of the energy of electrons and  
<sup>198</sup> photons. The ECAL is built as a sandwich of alternating scintillators and lead layers in  
<sup>199</sup> the *xy* plane. Scintillation light produced by the shower of particles generated by the

## 2.3. Particle Identification (PID)

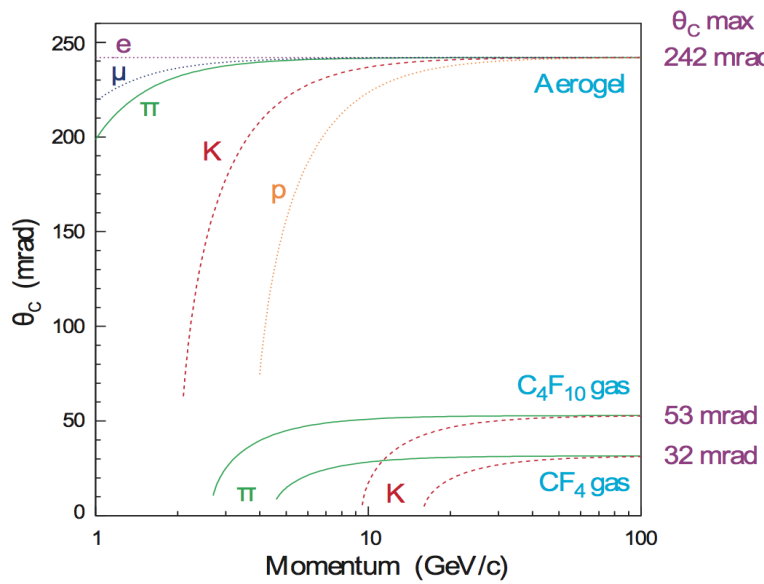


Figure 2.8 – Cherenkov angle as a function of the momentum for different particles and media.

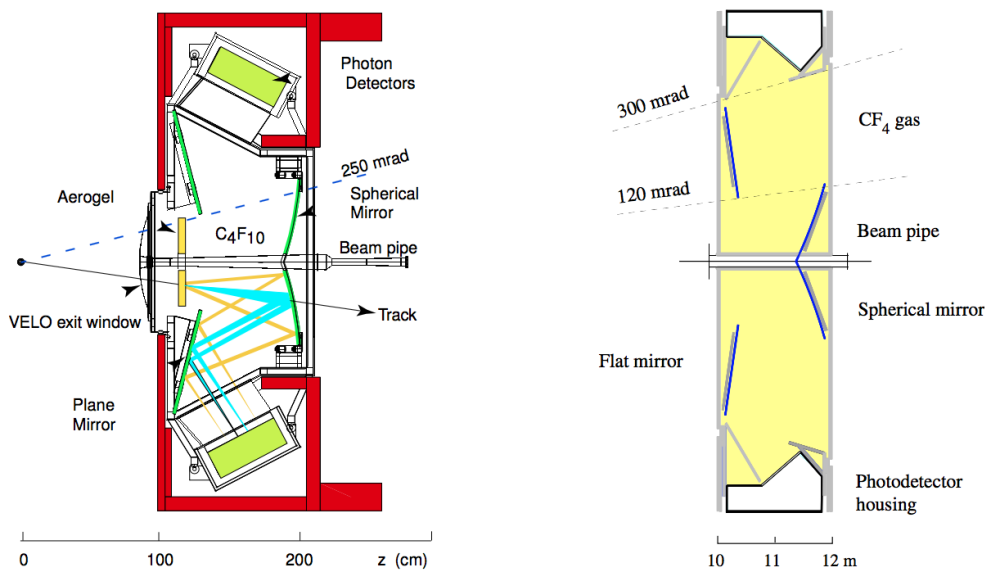


Figure 2.9 – Side view of RICH1 (left) and top view of RICH2 (right).

200 lead plates is read out by Wave-Length Shifter (WLS) fibres coupled to PhotoMultiplier  
201 Tubes (PMTs). The SPD is installed upstream the ECAL to separate electrons from  
202 photons. The PS is installed between the SPD and the ECAL. Both SPD and PS use  
203 scintillator pads read out by WLS fibres coupled to MultiAnode PhotoMultiplier Tubes  
204 (MAPMT). The acceptance range of the ECAL is from 25 mrad up to 300 (250) mrad in  
205 the horizontal (vertical) plane. The relative energy resolution of the ECAL is given by  
206  $\sigma_E/E = 10\%/\sqrt{E} \oplus 1\%$ , where  $E$  is given in GeV.

### 207 The Hadronic CALorimeter (HCAL)

208 The HCAL [27] is used for the detection and measurement of the energy of hadrons (such  
209 as pions and kaons) for the first level trigger. A HCAL cell is a sampling device made  
210 of alternating iron and scintillator tiles, where the latters are located along the beam  
211 direction. The HCAL has the same acceptance coverage of the ECAL. The relative energy  
212 resolution of the HCAL is given by  $\sigma_E/E = (69 \pm 5)\%/\sqrt{E} \oplus (9 \pm 2)\%$ , where  $E$  is given  
213 in GeV.

### 214 Muon detector

215 The muon system [28] (Fig. 2.10) is a gaseous detector divided in five stations (M1 to M5)  
216 interleaved by 80 cm thick iron filters. The gaseous detectors are Multi-Wire Proportional  
217 Chambers (MWPC), except for the innermost part of M1, where triple GEM detectors  
218 are used to cope with the higher track density. The angular acceptance ranges from 20  
219 (16) to 308 (256) mrad in the horizontal (vertical) plane. The muon detector has 1380  
220 chambers and covers a total area of 435 m<sup>2</sup>. Each muon chamber is composed by four  
221 layers of MPWC, except for M1, where two layers are used. The hit efficiency of the  
222 chambers is higher than 99% and allows to achieve a trigger efficiency greater than 95%  
223 for muons. The adopted gas mixture (Ar/CO<sub>2</sub>/CF<sub>4</sub> 40/55/5%) allows a fast triggering  
224 on muons (40 MHz).

#### 225 2.3.1 The trigger system

226 The collision rate of LHC is very high (40 MHz) because more than 99% of the  $pp$  collisions  
227 do not produce interesting events. It's not possible to record events with such a high  
228 rate: therefore, a trigger system [29] is required to reduce the rate from 40 MHz down to  
229 few kHz. The rate reduction is achieved via selection criteria which ensure that events  
230 containing heavy flavour decays are stored. The signatures of these interesting decays  
231 include high  $p_T$  and transverse energy of the decay products, as well as displaced decay  
232 vertices (with large IP) due to the relative long lifetimes of  $b$ - and  $c$ -hadrons. The trigger  
233 is divided into two sequential stages: a hardware stage called Level-0 (L0), and a software  
234 stage called the High Level Trigger (HLT). Different trigger decisions are separated into

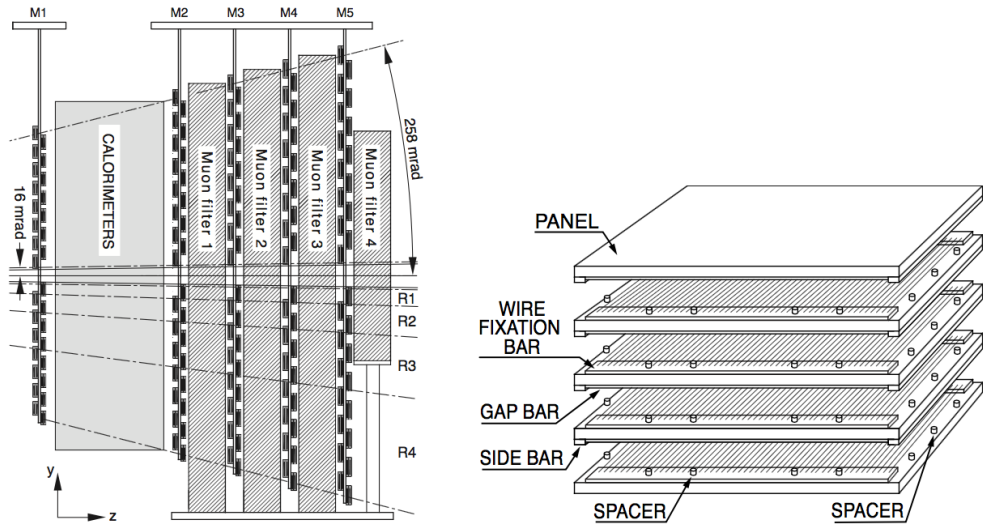


Figure 2.10 – Schematic overview of the muon system and a MWPC.

- 235 various *lines*, each of which provides informations on different physics process (e.g. decay  
 236 topology, presence of muons etc...). All the trigger steps are summarised in Fig. 2.11.
- 237 Two types of trigger response are assigned offline, when some physics channel is analysed.  
 238 The TOS (*Trigger On Signal*) trigger occurs when the event contains the user-defined  
 239 signal channel. The TIS (*Trigger Independent of Signal*) trigger response is given regardless  
 240 of the presence of the signal in that event.
- 241 After the trigger stage, the data go through further offline selection steps, where exclusive  
 242 (e.g.  $B^0 \rightarrow D^- \pi^+$ ,  $B^+ \rightarrow J/\psi K^+$ ) and inclusive (e.g.  $J/\psi \rightarrow \mu^+ \mu^-$ ) decays are  
 243 reconstructed. This offline selection step is known as *stripping*, and each set of selection  
 244 requirement is called *stripping line*.

#### 245 Level-0 (L0)

- 246 The L0 trigger mainly exploits the calorimeters and muon chambers. The idea behind the  
 247 L0 trigger is to select events that contain high pT muons and high ET hadrons, electrons  
 248 and photons, which very likely come from *b*- and *c*-hadron decays. The L0 trigger reduces  
 249 the data rate from 40 MHz down to 1 MHz.

#### 250 High Level Trigger (HLT)

- 251 The HLT is separated into two stages, HLT1 and HLT2, and runs on about 29000  
 252 commercial CPU cores.

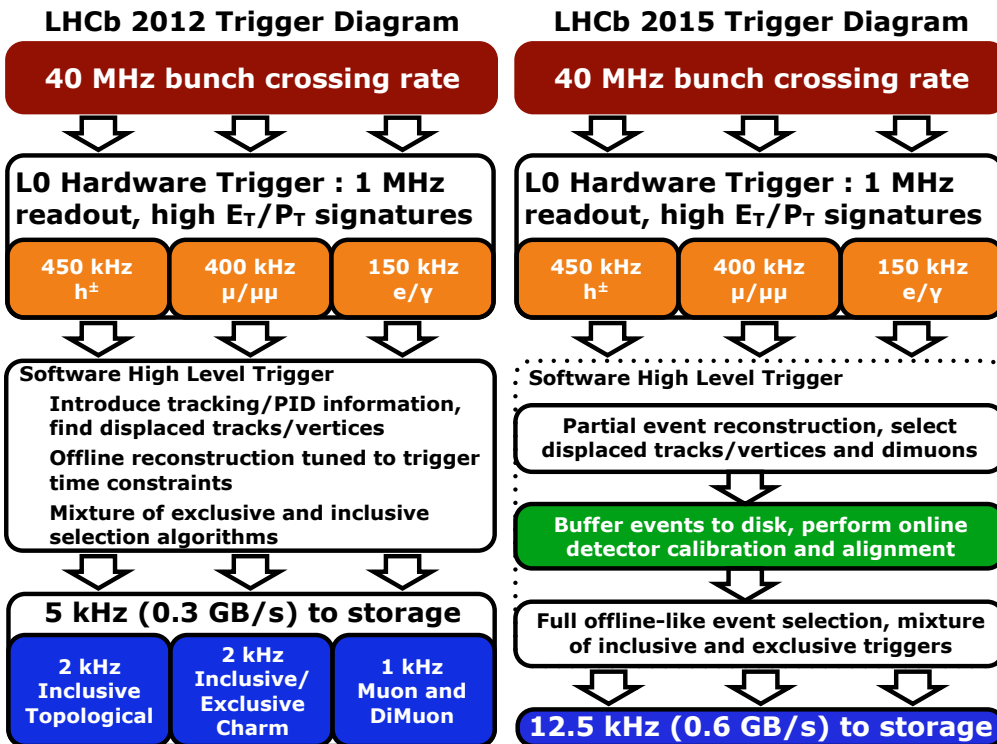


Figure 2.11 – Summary of the trigger strategy followed during Run 1 data-taking period (2011-2012, left) and Run 2 (2015-2017, right). During Run 2, an online detector and calibration alignment was introduced, plus full event selections (both inclusive and exclusive).

- 253 At the HLT1 level, the full detector information is read out, and then vertex/track  
 254 reconstruction and PID are performed. The exploited signatures are mainly the presence  
 255 of high  $p_T$  tracks, high transverse energy calorimeter clusters (photons and  $\pi^0$ ), high  
 256 di-muon invariant mass and tracks with large IP. All the HLT1 trigger lines are *inclusive*,  
 257 meaning that only decay products common to various decay processes are selected rather  
 258 than specific decays. After the HLT1, the rate goes down to about 70 kHz.
- 259 The HLT2 is a combination of mainly inclusive selections and algorithms that reconstruct  
 260 entirely (*exclusively*) some decay processes. The main lines are topological lines using  
 261 Multi-Variate Analysis (MVA) with different sets of kinematic and position features as  
 262 input, exclusive charm lines and high mass displaced di-hadron/lepton lines. After the  
 263 HLT2, the events are finally stored on tape for further offline analysis.

<sup>264</sup> 2.3.2 Event reconstruction, simulation and software

<sup>265</sup> Track and vertex reconstruction

<sup>266</sup> Starting from the *hits* in the tracking detectors, tracks and vertices are reconstructed  
<sup>267</sup> via dedicated algorithms. Different track types are reconstructed, as shown in Fig. 2.12.  
<sup>268</sup> Each track is characterised by hits collected in different sub-detectors. For example,  
<sup>269</sup> downstream tracks, with no hits in the VELO, are typically associated to long-lived  
<sup>270</sup> particles such as  $\Lambda$  and  $K_s^0$ . Because of the presence of a magnetic field, tracks are bend  
<sup>271</sup> in the  $xz$  plane. By knowing the reconstructed particle trajectory and the magnetic field  
<sup>272</sup> map, it is possible to measure the momentum of the particle.

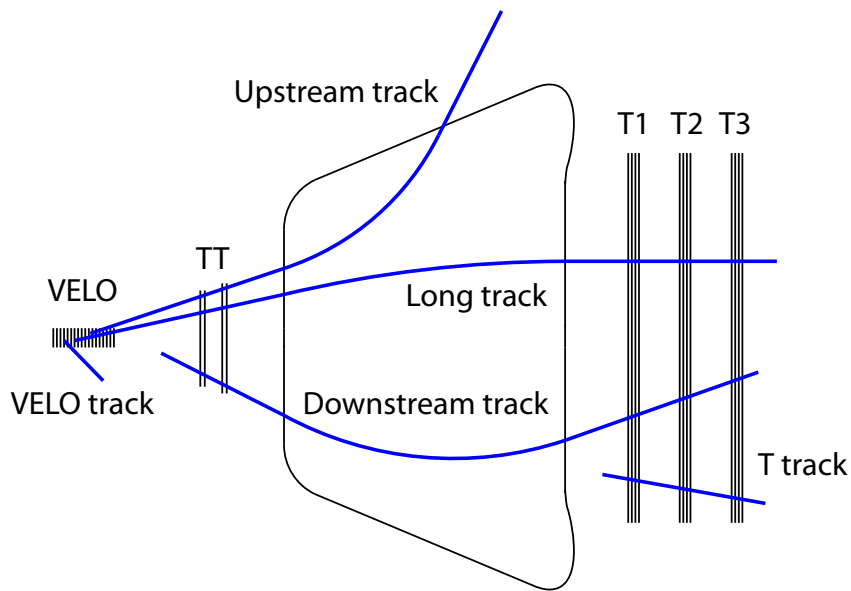


Figure 2.12 – Schematic description of the different track types reconstructed in LHCb.

<sup>273</sup> PID

The Cherenkov radiation emitted by charged particles in the RICH radiators produces *rings* in the RICH acceptance, which are reconstructed via pattern recognition algorithms. For each reconstructed pattern, the *likelihood*  $\mathcal{L}_\pi$  for the ring to be produced by a pion (the most common particle in the LHCb environment) is computed. The momentum of the particle is also used in the likelihood computation. Then, likelihood functions for other hypotheses (kaon, proton, electron, muon) are computed and compared with the

pion likelihood. For a given particle  $X$  ( $X = e, \mu, p, k$ ), the PIDX observable is defined as:

$$\text{PIDX} = \ln \mathcal{L}_X - \ln \mathcal{L}_\pi \quad (2.1)$$

- 274 In typical LHCb analyses, requirements on 2.1 are applied to suppress physical backgrounds  
275 due to wrongly-identified particles.

276 **Simulation**

277 The Monte Carlo (MC) simulation of  $pp$  collision, particle decays, and interaction with  
278 the detector are crucial in the validation of physics analyses. The parton-parton collision  
279 and hadronisation simulation is performed by PYTHIA [30], interfaced to EvtGen [31] for  
280 the decay of the hadrons and leptons for standard productions. The QED corrections to  
281 the decay (i.e. the emission of radiation photons) is generated by the PHOTOS package [32].  
282 The interactions of particles with detector material and their tracking in the magnetic  
283 field are simulated by GEANT4 [33].

284 **2.3.3 Data collected by LHCb**

The collision rate  $R$  [ $\text{s}^{-1}$ ] in LHC can be expressed in terms of the *cross-section*  $\sigma$  [ $\text{cm}^2$ ] and the *luminosity*  $\mathcal{L}$  [ $\text{s}^{-1}\text{cm}^{-2}$ ] as:

$$R = \mathcal{L}\sigma. \quad (2.2)$$

285 For a given data taking interval, the *integrated luminosity*  $L$  [ $\text{cm}^{-2}$ ] is a measure of the  
286 amount of recorded data. The typical unit for luminosity is the inverse *barn*, which  
287 corresponds to  $10^{-24} \text{ cm}^{-2}$ . The LHCb integrated luminosity are of the order of the  
288 inverse *femtobarn* ( $\text{fb}^{-1}$ ); one femtobarn corresponds to the production of about  $10^{11} b\bar{b}$   
289 quark pairs.

290 The LHCb detector collected data produced mainly from  $pp$  collisions in the 2010-2017  
291 period, so far. During the 2011-2012 data taking period, called *Run 1*, about  $3\text{fb}^{-1}$  of data  
292 was collected. The center-of-mass energy  $\sqrt{s}$  of the  $pp$  interactions was 7 TeV and 8 TeV  
293 in 2011 and 2012 respectively, and the time spacing between *bunches* of protons in LHC  
294 was 50 ns. The 2013-2014 period, known as *Long Shutdown 1* (LS1), was dedicated to  
295 some maintenance work for the LHC components. The *Run 2* data taking period started  
296 in 2015, and it is planned to last until the end of 2018. The center-of-mass energy of the  
297  $pp$  collisions during Run 2 is 13 TeV, whereas the time spacing between proton bunches  
298 is 25 ns. In the 2015-2017 data taking period, about  $3.7 \text{ fb}^{-1}$  of data was collected. The  
299 data collected for each year is summarised in Fig. 2.13.

### 2.3. Particle Identification (PID)

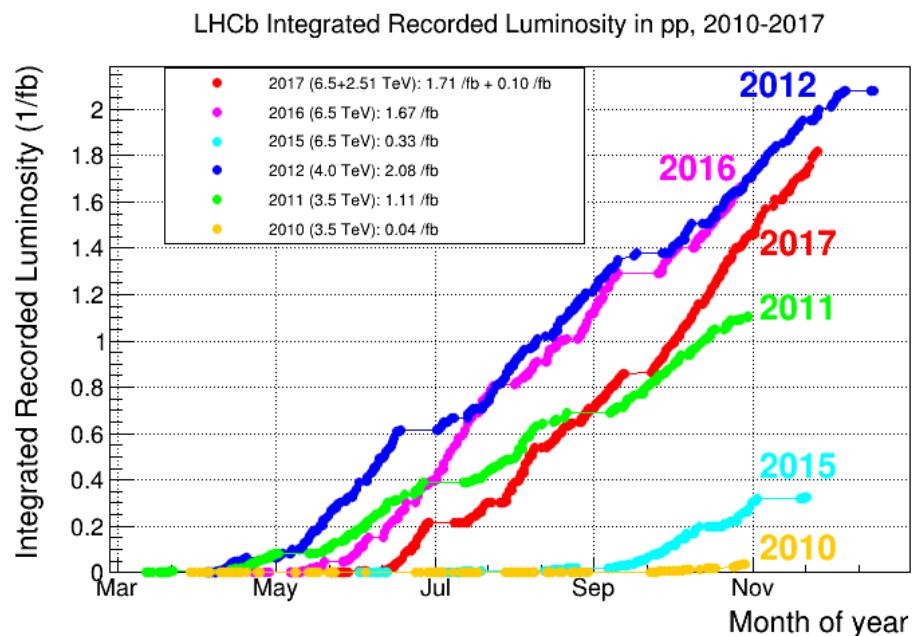


Figure 2.13 – Breakdown of the  $pp$  collision data collected by LHCb.



### **3** Flavour Tagging algorithms and <sup>301</sup> optimisation of the opposite-side electron tagger



## 4 Measurement of CP violation in <sub>303</sub> $B^0 \rightarrow D^\mp \pi^\pm$ decays

304 4.1 Introduction

In this chapter, a decay-time dependent analysis of the decay  $B^0 \rightarrow D^\pm \pi^\mp$  is presented, where the  $D$  meson is reconstructed as  $D^\pm \rightarrow K^\mp \pi^\pm \pi^\pm$ . The pion produced together with the  $D$  meson will be named as *bachelor* or *companion* particle hereafter. The objective of this study is to perform a measurement of CP asymmetries, which allow to constrain the CKM angle  $\gamma$  [14, 15]. Measurements of  $\gamma$  via tree-level decays such as  $B^0 \rightarrow D^\pm \pi^\mp$  are theoretically clean [34, 35, 36]. The CP-violation appears in the interference between the Cabibbo favoured  $b \rightarrow c$  amplitude without mixing,  $A(B^0 \rightarrow D^- \pi^+)$ , and the Cabibbo suppressed  $b \rightarrow u$  amplitude with mixing,  $A(B^0 \rightarrow \bar{B}^0 \rightarrow D^- \pi^+)$ . Two of the corresponding Feynman diagrams for these amplitudes are depicted in fig. 4.1.

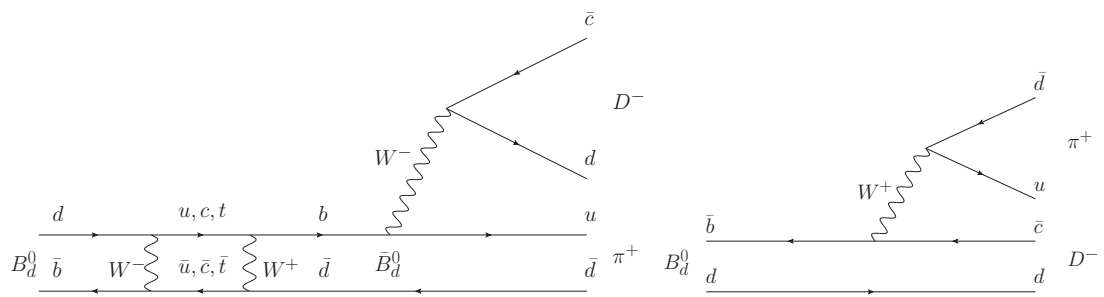


Figure 4.1 – Feynman diagrams contributing to  $B^0 \rightarrow D^\pm \pi^\mp$

The measurement is performed by analysing the four decay-time dependent decay rates  $\frac{d\Gamma(B^0 \rightarrow D^- \pi^+)}{dt}$ ,  $\frac{d\Gamma(B^0 \rightarrow D^+ \pi^-)}{dt}$ ,  $\frac{d\Gamma(\bar{B}^0 \rightarrow D^- \pi^+)}{dt}$  and  $\frac{d\Gamma(\bar{B}^0 \rightarrow D^+ \pi^-)}{dt}$ . Identifying the final state as  $f = D^- \pi^+$  or  $\bar{f} = D^+ \pi^-$ , and assuming CPT symmetry and no CP violation in mixing ( $|q/p| = 1$ ), the time-dependent decay rates for  $B$  mesons initially produced as  $B^0$  or  $\bar{B}^0$  can be written as follows:

$$\frac{d\Gamma(B^0 \rightarrow f)}{dt}(t) = \frac{1}{4\tau_d} e^{-t/\tau_d} [1 + C_f \cos(\Delta m_d t) - S_f \sin(\Delta m_d t)], \quad (4.1)$$

$$\frac{d\Gamma(\bar{B}^0 \rightarrow f)}{dt}(t) = \frac{1}{4\tau_d} e^{-t/\tau_d} [1 - C_f \cos(\Delta m_d t) + S_f \sin(\Delta m_d t)], \quad (4.2)$$

$$\frac{d\Gamma(B^0 \rightarrow \bar{f})}{dt}(t) = \frac{1}{4\tau_d} e^{-t/\tau_d} [1 - C_{\bar{f}} \cos(\Delta m_d t) + S_{\bar{f}} \sin(\Delta m_d t)], \quad (4.3)$$

$$\frac{d\Gamma(\bar{B}^0 \rightarrow \bar{f})}{dt}(t) = \frac{1}{4\tau_{\bar{f}}} e^{-t/\tau_d} [1 + C_{\bar{f}} \cos(\Delta m_d t) - S_{\bar{f}} \sin(\Delta m_d t)], \quad (4.4)$$

where  $\Delta m_d$  and  $\tau_d = 1/\Gamma_d$  are given by Eq. 1.23 and 1.24, while  $\Delta\Gamma_d = 0$ . The

CP-coefficients  $C_{f/\bar{f}}$  and  $S_{f/\bar{f}}$ , defined in Eq. 1.40 and 1.41, can be expressed as

$$S_f = \frac{2r_{D\pi} \sin[\delta_B - (\gamma + 2\beta)]}{1 + r_{D\pi}^2}, \quad S_{\bar{f}} = \frac{2r_{D\pi} \sin[\delta_B + (\gamma + 2\beta)]}{1 + r_{D\pi}^2}, \quad (4.5)$$

$$C_f = -C_{\bar{f}} = C = \frac{1 - r_{D\pi}^2}{1 + r_{D\pi}^2}, \quad (4.6)$$

314 where  $\beta$  (Eq. 1.9) is related to the  $B^0$  mixing phase,  $r_{D\pi} = |A(\bar{B}^0 \rightarrow D^- \pi^+)/A(B^0 \rightarrow D^- \pi^+)|$   
 315 is the magnitude of the ratio between doubly Cabibbo suppressed and favoured amplitudes,  
 316 and  $\delta_B$  is the strong phase difference between these amplitudes.

317 A measurement of  $\gamma$  can be obtained by measuring the CP-coefficients and taking external  
 318 measurement of  $\beta$  and  $r_{D\pi}$  as input. The angle  $\beta$  is known with very high precision, both  
 319 theoretically and experimentally [37]. An estimation of  $r_{D\pi}$  was performed by BaBar  
 320 and Belle experiments [38, 39], by measuring the branching fraction of  $B^0 \rightarrow D_s^{(*)+} \pi^-$   
 321 decays and assuming SU(3) symmetry, yielding an average of about 1.7% with a relative  
 322 error around 15%, mainly due to SU(3) symmetry breaking. For this analysis,  $C_f$  ( $C_{\bar{f}}$ ) is  
 323 simply fixed to 1 ( $-1$ ) due to a lack of *sensitivity*.

324 The small value for the  $r_{D\pi}$  parameter, which reduces the sensitivity on  $S_{f/\bar{f}}$ , make this  
 325 measurement challenging compared to similar analyses like  $B_s^0 \rightarrow D_s^\mp K^\pm$ ; however, the  
 326 expected signal yield (about  $5 \times 10^5$  signal events) is sufficiently large to compensate for  
 327 this lack of sensitivity.

328 Measurements of  $\sin(2\beta + \gamma)$  in  $B^0 \rightarrow D^{(*)\pm} \pi^\mp$  were performed by the BaBar and Belle  
 329 experiments [40, 41, 42, 43]. A measurement of  $2\beta_s - \gamma$  was performed by LHCb in  
 330  $B_s^0 \rightarrow D_s^\mp K^\pm$  decays by analysing  $1 \text{ fb}^{-1}$  of data [44].

### 331 Analysis strategy

332 The measurement is performed in terms of a flavour tagged, decay-time dependent analysis  
 333 of the Run 1 dataset. The dataset includes two sub-samples recorded with opposite  
 334 directions of the magnetic field ("up" and "down") in the spectrometer dipole. The  
 335 selection of the data, which is explained in detail in Sec. 4.2, includes the use of vetoes  
 336 to reduce the number of components that must be modelled in the sample, and a BDT  
 337 to reduce the amount of *combinatorial* background. The expected sample composition  
 338 after the selection is discussed in Sec. 4.3 based on studies with simulated samples. A  
 339 fit to the invariant mass distribution of the resulting dataset is performed to extract  
 340 sWeights for the signal component. The fit is described in detail in Sec. 4.4. The training  
 341 and calibration of the flavour tagging algorithms, which infer the initial flavour of the  
 342 reconstructed  $B^0$  candidates, is summarised in Sec. ???. The final estimation of the  
 343 CP-coefficients is the result of an unbinned, sWeighted likelihood fit to the distributions  
 344 of the decay time and the flavour tagging observables.

## 345 4.2 Data sample and selection

346 The sample of data is passed through the following selection steps:

- 347 1. stripping and trigger requirements;
- 348 2. a *cut-based* preselection;
- 349 3. vetoes for misidentified backgrounds and wrongly associated *primary vertices* (PVs);
- 350 4. a multivariate classification (MVA);
- 351 5. a final randomised multiple candidate selection.

352 In what follows, the details of each step are provided.

### 353 4.2.1 Stripping and trigger requirements

354 Signal  $B^0 \rightarrow D^\pm\pi^\mp$  candidates are reconstructed using a dedicated stripping line (called  
 355 `B02DPiD2HHHBeauty2CharmLine`). Each event is required to have less than 500 Long tracks. The criteria that the charged tracks have to fulfill are listed in Tab. 4.1. Three

Table 4.1 – Stripping requirements applied in the selection of charged tracks. The more stringent requirements for the bachelor track are given in brackets.

$\chi^2/\text{ndof}$	$< 3.0 (< 2.5)$
momentum $p$	$> 1 \text{ GeV}/c (> 5 \text{ GeV}/c)$
transverse momentum $p_T$	$> 100 \text{ MeV}/c (> 500 \text{ MeV}/c)$
IP $\chi^2$ w.r.t. any PV	$> 4.0$
ghost probability	$< 0.4$

356 of these hadrons have to form a common vertex to build a  $D$  meson. The (transverse)  
 357 momentum of one of the daughter hadrons has to exceed ( $500 \text{ MeV}/c$ )  $5 \text{ GeV}/c$  and its  
 358 track  $\chi^2/\text{ndof}$  has to be less than 2.5. The further requirements on the  $D^\mp$  combination are  
 359 given in Tab. 4.2. The  $B$  candidates are built by combining a  $D$  candidate and a bachelor  
 360 particle if the requirements listed in Tab. 4.3 are fulfilled. Finally, a bagged boosted  
 361 decision tree (BDT) classifier, which is trained on simulated candidates, is applied [45]. A  
 362 minimum value of 0.05 is required for the output value of the BDT. Stripping candidates  
 363 are then filtered according to how they were selected at the trigger level: no specific  
 364 requirements are made at L0; at HLT1,  $B$  candidates are required to be TOS on the  
 365 `Hlt1TrackAllL0Decision` trigger line; at HLT2,  $B$  candidates are required to be TOS on the  
 366 one of the following lines: `Hlt2Topo2BodyBBDTDecision`, `Hlt2Topo3BodyBBDTDecision`  
 367 or `Hlt2Topo4BodyBBDTDecision`. The details of these trigger lines are described in  
 368 Refs. [46, 47].

Table 4.2 – Stripping requirements on the  $D^\mp$  combination. DOCA is the Distance Of Closest Approach of the daughter particles w.r.t. each other, and DIRA indicates the cosine of the angle between the momentum of the  $D$  meson and the direction from the best PV to the decay vertex.

$\sum p_T(hhh)$	> 1800 MeV/ $c$
DOCA	< 0.5 mm
$m_D^\mp$	1769.62 to 2068.49 MeV/ $c^2$
$D^\mp \chi_{\text{vtx}}^2/\text{ndof}$	< 10.0
vertex separation $\chi^2$ to any PV	> 36
DIRA	> 0.0

Table 4.3 – Stripping requirements on the  $B^0$  combination.

SV $\chi^2/\text{ndof}$	< 10.0
reconstructed decay time $t$	> 0.2 ps
IP $\chi^2$ w.r.t. the associated PV	< 25.0
DIRA	> 0.999

370 Figure 4.2 shows the  $B$  and  $D$  mass distributions of the reconstructed candidates after  
 371 the stripping and trigger selection. In the  $B$  mass distribution the signal peak is already  
 372 visible at around 5280 MeV/ $c^2$ . The structure at masses lower than the  $B$  peak originates  
 373 from partially reconstructed  $B^0 \rightarrow D\rho$  and  $B^0 \rightarrow D^*\pi$  decays. The  $D$  mass distributions  
 features a clearly visible  $D$  peak at 1870 MeV/ $c^2$  and a  $D^*$  peak around 2010 MeV/ $c^2$ .

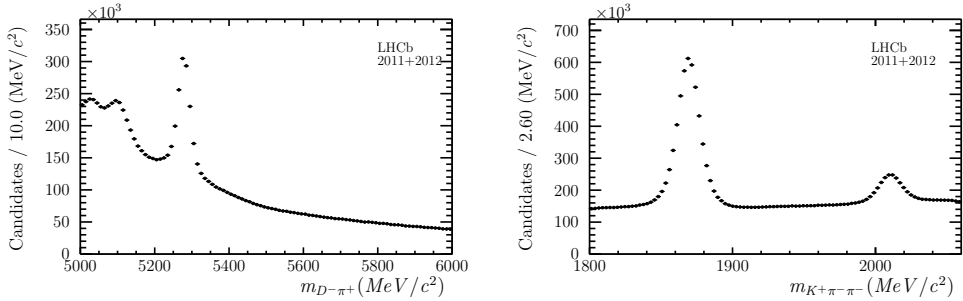


Figure 4.2 –  $B$  and  $D$  mass distributions of the reconstructed candidates after the stripping and trigger selection.

374

### 375 4.2.2 Preselection and samples definition

376 Additional preselection criteria (shown in Tab. 4.4) are applied offline. In order to  
 377 obtain the correct correlations between and uncertainties on vertex positions, particle  
 378 momenta, flight distances, decay times, and invariant masses, a Kalman filter, known as

379 DecayTreeFitter (DTF), is used [48]. The decay time related observables are derived  
 380 from a DTF fit where the knowledge about the primary vertex has been used to constrain  
 381 the production vertex of the  $B^0$  meson. To determine the momenta and the invariant  
 382 mass of the  $B^0$  meson, the invariant mass of the  $D$  meson is constrained to the PDG  
 value ( $m_{D^\pm}^{\text{PDG}} = 1869.61 \text{ MeV}/c^2$  [19]) in a separate DTF fit. The PIDK variable 2.1 is

Table 4.4 – Offline preselection criteria

Cuts on $B^0$ candidate	
decay time	$> 0.2 \text{ ps}$
Cuts on $D$ meson	
$ m(K^+\pi^-\pi^-) - m_D $	$< 35 \text{ MeV}/c^2$
Cuts on $D$ daughters	
PIDK for pions	$< 8$
PIDK for kaon	$> -2$

383 used to identify the kaon and the pions from the  $D$  decays, and to identify the bachelor  
 384 pion from the  $B$  decay. The requirement on the PIDK of the bachelor pion define two  
 385 categories of candidates: those of the so-called the *pion sample* ( $\text{PIDK} \leq 5.0$ ) and those  
 386 of the *kaon sample* ( $\text{PIDK} > 5.0$ ). This distinction will be useful in the fit to the  $B$   
 387 mass distribution for determining the sample composition described in Sec. 4.4. All the  
 388 following step of the selection are applied to data without distinction in pion and kaon  
 389 samples.

### 391 4.2.3 Veto for physics backgrounds

392 Misidentification of kaons and protons as pions lead to exclusive backgrounds in the data  
 393 sample. These are suppressed by means of explicit *veto*s.

394 In order to reduce contributions from semileptonic decays such as  $B^0 \rightarrow D^- (\rightarrow K^+\pi^-\pi^-) \mu^-\bar{\nu}_\mu$ ,  
 395 the bachelor pion is required to have no hits in the muon chambers.

396 For the  $D^\pm$  mesons which are reconstructed in the  $D^\pm \rightarrow K^\mp\pi^\pm\pi^\pm$  final state, a  $p \rightarrow \pi$   
 397 mis-ID can lead to background contributions from  $\Lambda_b^0 \rightarrow \Lambda_c^\pm (\rightarrow K^\mp\pi^\pm p) \pi^\mp$ . To reduce  
 398 these contributions, the proton mass hypothesis is applied separately to both pions from  
 399 the  $D^\pm$  final state. The invariant mass of the three hadrons is recalculated and if the  
 400 candidate is inside a  $30 \text{ MeV}/c^2$  window around the  $\Lambda_c$  mass,  $m_{\Lambda_c} = 2286.46 \text{ MeV}/c^2$  [19],  
 401 it is required to have  $\text{PIDp} < -8.0$  and if it is inside a  $50 \text{ MeV}/c^2$  window around the  $\Lambda_c$   
 402 mass it is required to have  $\text{PIDp} < -5.0$ . A plot showing the distributions before and  
 403 after applying the veto is given in Fig. 4.3. This requirement shows a signal efficiency  
 404 of  $(93.48 \pm 0.06)\%$ . For the rejection of  $\Lambda_b^0 \rightarrow \Lambda_c^\pm\pi^\mp$ , the efficiency on a signal MC  
 405 for this decay is checked. After stripping and preselection alone,  $(99.720 \pm 0.004)\%$  of

## 4.2. Data sample and selection

406 the  $\Lambda_b^0 \rightarrow \Lambda_c^\pm \pi^\mp$  candidates are rejected; this veto rejects another  $(76.6 \pm 0.6)\%$  of the  
 407  $\Lambda_b^0 \rightarrow \Lambda_c^\pm \pi^\mp$  candidates.

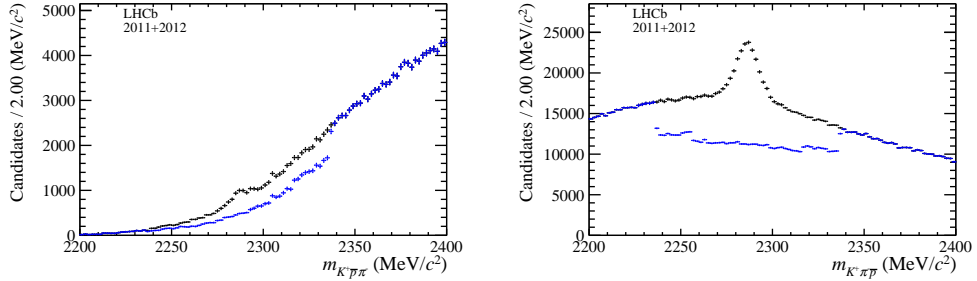


Figure 4.3 – Plots of the invariant mass of the  $K\pi p$  combinations for both daughter pions of the  $D$  meson misidentified as protons. The distribution is given without (black) and with (blue) the  $\Lambda_c^\pm$  veto described in the text. The distributions look different for both plots because they are sorted by  $p_T$ . (Left the proton mass hypothesis is applied to pions with lower  $p_T$ , right to pions with higher  $p_T$ ).

408 In the same way as protons are misidentified as pions, it is possible for kaons to be  
 409 misidentified as pions. Such a mis-ID would lead to background contributions from  
 410  $B_s^0 \rightarrow D_s^\pm (\rightarrow K^\mp K^\pm \pi^\pm) \pi^\mp$ . To check for these contributions, the kaon mass hypothesis  
 411 is applied separately to both pions from the  $D^\pm$  final state. The invariant mass of the  
 412 resulting  $K^\mp K^\pm \pi^\pm$  system is recalculated and plotted for two different ranges of the  $B^0$   
 413 mass: The first range, from 5330 to 5400 MeV/ $c^2$ , covers the invariant mass signal region  
 414 of the  $B_s^0$  meson as possible background contribution. The second range, from 5500 to  
 415 5700 MeV/ $c^2$  is the upper mass *sideband* for this possible background contamination. As  
 416 can be seen in Fig. 4.4 the distribution which covers the invariant mass of the  $B_s^0$  meson  
 417 does not show any significant peaking structure compared to the upper mass sideband  
 418 region. The visible differences are expected as the distributions arise from different  
 419 kinematic ranges. To double check for possible resonant contributions from a kaon mis-ID,  
 420 the decay of the  $D$  meson after applying the kaon mass hypothesis is investigated. Possible  
 421 resonant decays of the  $D$  meson can take place via a  $K^*$  or  $\phi$  resonance. These resonances  
 422 would be visible in the  $K\pi$  and  $KK$  invariant mass distributions, which are plotted in  
 423 the same two ranges in fig. 4.5. As the distributions in the signal and background range  
 424 look compatible, the  $D_s^+$  contamination is negligible and no veto is applied.

425 In the same way as for the  $D$  meson daughters, it is also possible that the bachelor  
 426 pion candidate is actually a misidentified kaon. This mis-ID could lead to background  
 427 contributions of  $B^0 \rightarrow D^0 (\rightarrow K^\mp \pi^\pm) K^+ \pi^-$ . The same background contribution could  
 428 arise if one  $D$  meson daughter pion is misidentified as a kaon and combined with the  
 429 bachelor pion. To check for this contribution, the kaon mass hypothesis is applied to  
 430 the bachelor pion and the  $D$  meson daughter pions, and the invariant mass distributions  
 431 for the four possible  $K\pi$  systems are plotted after applying the BDT classifier described  
 432 in Sec. 4.2.5 (fig. 4.6). As the distributions show no significant peaking structures, this

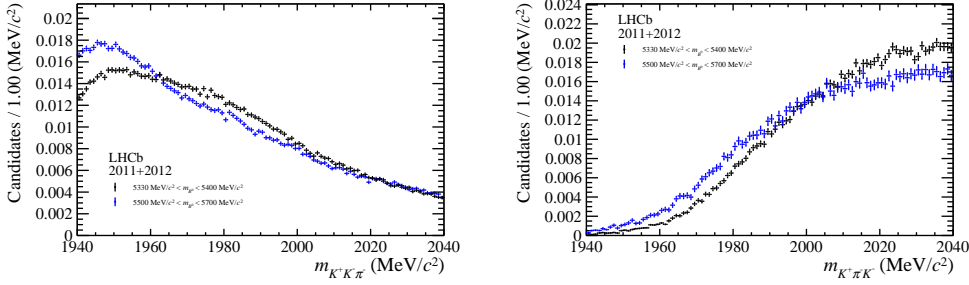


Figure 4.4 – Plots of the invariant mass of the  $KK\pi$  combinations for both daughter pions of the  $D$  meson misidentified as kaons. The distribution is given in the  $B^0$  meson mass range from 5300 to 5400  $\text{MeV}/c^2$  (black) and in the  $B^0$  meson mass range from 5400 to 5500  $\text{MeV}/c^2$  (blue) after applying the  $\Lambda_c^+$  veto. The distributions look different for both plots because they are sorted by  $p_T$ . (Left the kaon mass hypothesis is applied to pions with lower  $p_T$ , right to pions with higher  $p_T$ ).

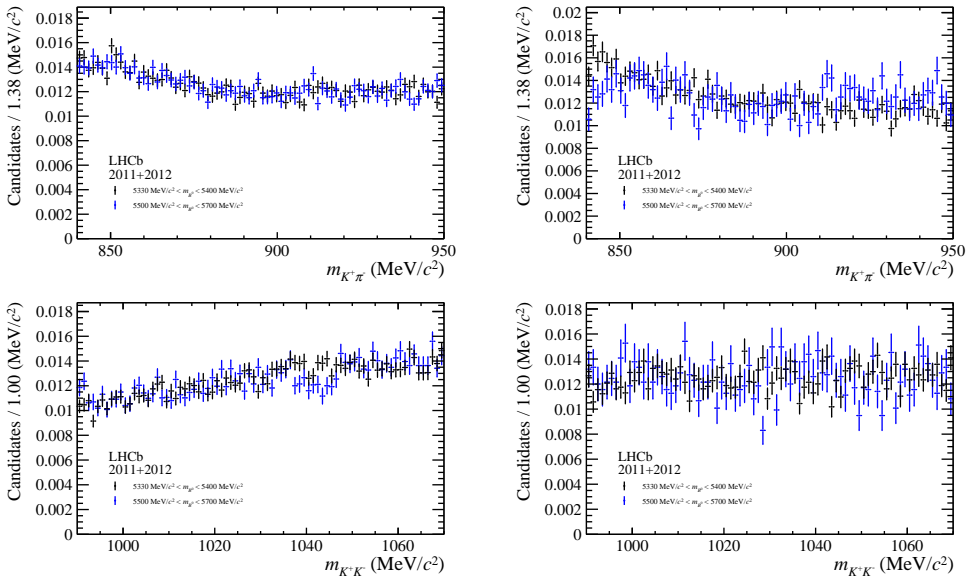


Figure 4.5 – Plots of the invariant mass of the  $K\pi$  combination (top) and for the  $KK$  combination (bottom) for both daughter pions of the  $D$  meson. The distributions are shown in the  $B^0$  meson mass range from 5330 to 5400  $\text{MeV}/c^2$  (black) and in the  $B^0$  meson mass range from 5500 to 5700  $\text{MeV}/c^2$  (blue) as described in the text. Additionally, for all plots a cut on the  $D_s^+$  mass hypothesis from 1940 to 2040  $\text{MeV}/c^2$  is applied. The distributions look different for both plots because they are sorted by  $p_T$ . (Left the kaon mass hypothesis is applied to pions with lower  $p_T$ , right to pions with higher  $p_T$ ).

contribution is neglected at this stage and no specific cuts are applied.

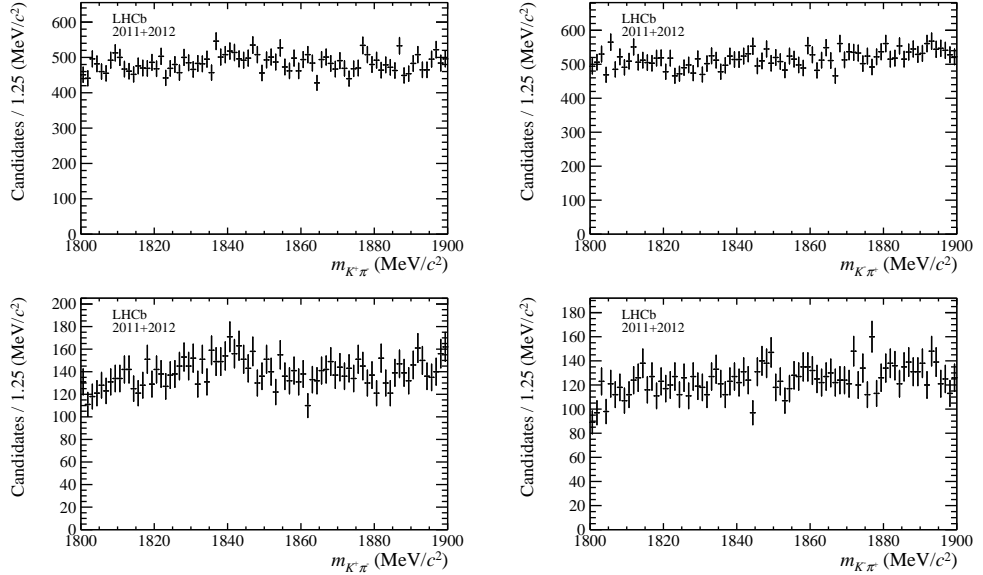


Figure 4.6 – Plots of the invariant mass of the four possible  $K\pi$  combinations after applying a kaon mass hypothesis to the bachelor pion. In the top plots the bachelor pion is combined with the  $D$  meson daughter pion with lower  $p_T$ , in the bottom plots the combination with the  $D$  meson daughter pion with the higher  $p_T$  is shown. In the left plots the kaon mass hypothesis is applied to the bachelor pions and in the right plots to the  $D$  meson daughter pions.

433

#### 434 4.2.4 Wrongly associated PVs

435 Given an average number of  $pp$  interactions per bunch crossing of  $\nu = 2.5$ , a large fraction  
 436 of events have more than one reconstructed PV. The PV to which the  $B^0$  candidate  
 437 has the smallest  $\chi_{\text{IP}}^2$  (*best* PV) is chosen. Furthermore, It is possible that more than  
 438 one  $B^0$  candidate is reconstructed per event: in this case, the  $B^0$  candidate is chosen  
 439 randomly following the prescription of Ref. [49], which allows to prevent any bias due to  
 440 an arbitrary choice.

441 In events where the association of the  $B^0$  candidate to the best PV  $B^0$  is wrong, the  
 442 decay time of this candidate will be incorrect. These wrongly associated candidates are  
 443 responsible for a large tail that can be observed in the decay time distribution, particularly  
 444 in signal MC where the true decay time is known. Weighting each candidate with an  
 445 exponential with the true lifetime shows an excess of candidates at high decay times.  
 446 To remove these incorrect associations in MC, one can compare the  $z$ -position of the  
 447 associated PV with the  $z$  position of the true PV and reject the candidate if the distance  
 448 between those positions exceeds 5 times its uncertainty (fig. 4.7). In real data, the the

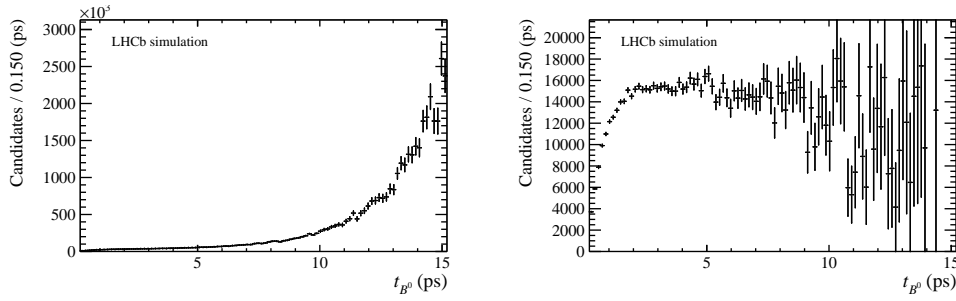


Figure 4.7 – Left: Signal MC decay time distribution weighted with an exponential with the true lifetime. At high decay times an excess of candidates can be observed. Right: Signal MC decay time distribution weighted with an exponential with the true lifetime. In addition, it is required that the difference of the PV  $z$  position with the true PV  $z$  position is within 5 times the PV uncertainty. As the excess of candidates at high decay times vanishes (from left to right), it can be concluded that these candidates are wrongly associated to their PV.

449 true PV in unknown, so a selection cut on the smallest  $B^0$  impact parameter  $\chi^2_{\text{DTF},\text{PV}}$  (called  $\text{MinIP}\chi^2$ ) with respect to any other PV in the event is applied (fig. 4.8). Events

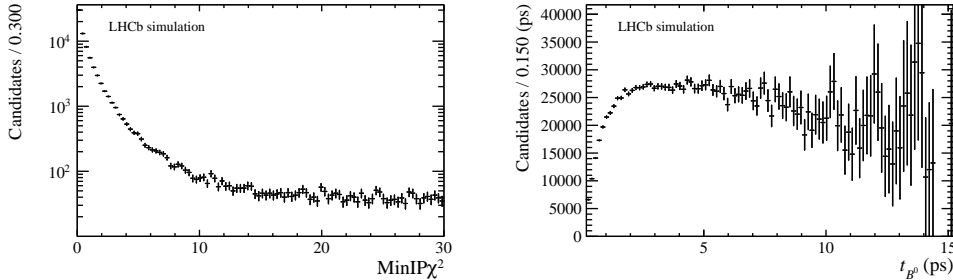


Figure 4.8 – Left: distribution of the smallest  $B^0$  impact parameter  $\chi^2_{\text{DTF}}$  with respect to any other primary vertex in the event. Right: Signal MC decay time distribution weighted with an exponential with the true lifetime after requiring that the smallest  $B^0$  impact parameter  $\chi^2_{\text{DTF}}$  to any other PV in the event is larger than 16.5.

450  
 451 with only a single PV are not affected. The main advantage of this  $\text{MinIP}\chi^2$  variable  
 452 is that all PVs are treated equally, without any biasing choice. The requirement on  
 453  $\text{MinIP}\chi^2$  is optimised to retain 98 % of the truth-matched signal candidates in MC. The  
 454 optimal cut is then found at  $\text{MinIP}\chi^2 > 16.5$ . A plot showing the weighted decay time  
 455 distribution after applying the cut on the smallest  $B^0$  impact parameter  $\chi^2_{\text{DTF},\text{PV}}$  to any  
 456 other PV is given in Fig. 4.8.

## 457 4.2.5 Development of an MVA classifier

458 The combinatorial background, consisting of fake signal candidates created from random  
 459 combinations of tracks, is rejected by using a Boosted Decision Tree (BDT) classifier [50,  
 460 51]. The signal input to the training stage consists of signal MC candidates simulated  
 461 under 2012 data taking conditions, while the upper mass side band above  $5500 \text{ MeV}/c^2$   
 462 from the 2012 data sample is used as template for the combinatorial background. The  
 463 BDT is trained on one half of these samples, the other half being used to test the  
 464 performance of the BDT. Before the BDT training, all previous steps (the cut-based  
 465 preselection, the mass vetoes and the wrongly associated PV veto) are applied. To reduce  
 466 the number of input features, the ones with a correlation larger than 97 % are removed.  
 The 16 final input features are listed in Tab. 4.5. The correlation matrices between the

Table 4.5 – List of input features used in the training of the BDT

$B^0$ candidate	$\cos \propto [ PV, B^0 Vtx , \vec{p}(B^0)]$ $\chi^2$ on $B^0$ vertex
	$\chi^2_{\text{IP}}$ w.r.t. $B^0$ vertex
	$\chi^2_{\text{IP}}$ w.r.t. associated PV
	radial flight distance
$D$ candidate	flight distance $\chi^2$ w.r.t. $B^0$ vertex
	$\chi^2/\text{ndof}$ on $D$ vertex
	transverse momentum
	$\cos \propto [ B^0 Vtx, D Vtx , \vec{p}(D)]$
bachelor $\pi$	$\chi^2_{\text{IP}}$ w.r.t. the associated PV
	transverse momentum
	track $\chi^2/\text{ndof}$
$D$ daughters	$\chi^2_{\text{IP}}$ of associated primary vertex
DTF	$\chi^2$ of DTF with PV constraint

467  
 468 input features in the signal and the background sample are shown in Fig.4.9, while the  
 469 distributions of the input features can be found in Appendix 4.5.1.

470 The BDT implementation of TMVA [52] is used. The BDT is built out of 1700 trees,  
 471 with a depth limited to four. For each node, at least 2.5 % of the training events have to  
 472 be present. The variables are scanned at 20 points to find the optimal cut value. The  
 473 chosen boosting method is the AdaBoost [53] algorithm with a boost factor  $\beta = 0.5$ . The  
 474 number of trees and the maximal depth of trees have been increased iteratively until no  
 475 significant increase of the performance or overtraining was observed. The BDT is tested  
 476 on the events which are not used in the training. The plot of this overtraining check is  
 477 given in Fig.4.10.

## Chapter 4. Measurement of CP violation in $B^0 \rightarrow D^\mp \pi^\pm$ decays



Figure 4.9 – Correlation matrices of the input features used in the training of the BDT for signal (left) and background (right).

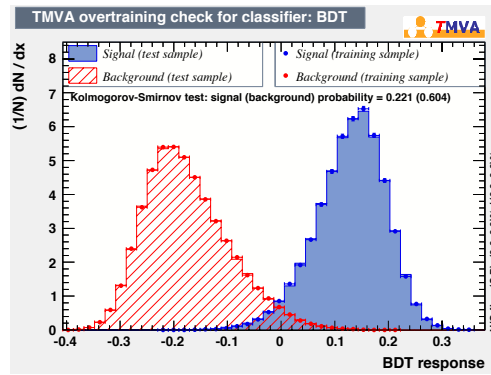


Figure 4.10 – Comparison of BDT response on training and test sample.

## 478 4.2.6 BDT selection optimisation

479 To estimate the best requirement on the output of the BDT classifier, the statistical  
 480 uncertainty of the CP-coefficients derived from the analysis of simulated samples is used  
 481 as the figure of merit (FoM). To determine the sensitivity, the preselection, the mass  
 482 vetoes and the wrongly associated PV veto are applied and the BDT classifier is calculated  
 483 for every candidate. The BDT cut point is then scanned with a step size of 0.01 from  
 484  $-0.15$  to  $0.10$  and a step size of 0.05 in the outer regions. For each cut point of the BDT  
 485 classifier, a simulated (*toy*) sample is generated. This simulated sample contains the same  
 486 signal and combinatorial background yields as determined from the real dataset via a  
 487 maximum likelihood fit of the  $B^0$  mass distribution. Finally, a time-dependent analysis of  
 488 each toy dataset is performed in order to estimate the statistical uncertainty on  $S_f$  and  
 489  $S_{\bar{f}}$ . These statistical uncertainties as a function of the BDT cut are shown in Fig. 4.11.  
 Based on these distributions, the BDT cut point is chosen to be at 0.05.

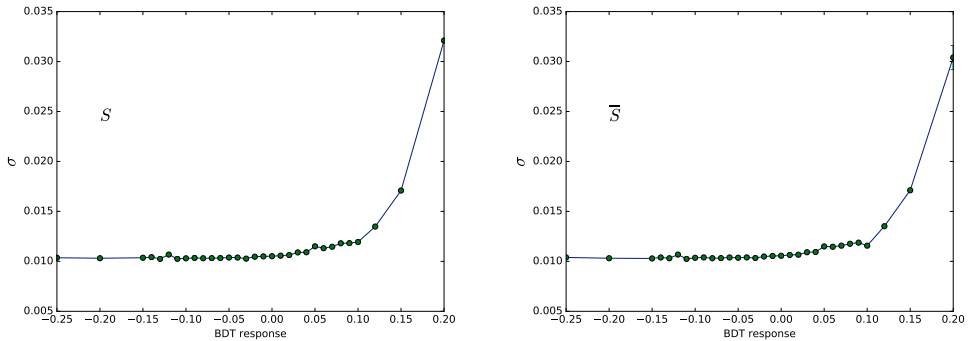


Figure 4.11 – Sensitivity of  $S_f$  (left) and  $S_{\bar{f}}$  (right) as a function of the BDT output classifier.

490

## 491 4.2.7 Multiple candidates

492 After the stripping selection, approximately 9 % of events contain at least two  $B^0$   
 493 candidates, and 18 to 20 % of all  $B^0$  candidates share an event. If the offline selection is  
 494 also applied, around 0.4 % of events contain multiple  $B^0$  candidates, and 0.8 % of all  $B^0$   
 495 candidates share an event. More details are given in Appendix 4.5.2. In order to be  
 496 consistent with the prescription used in the stripping and trigger requirements, only the  
 497 best PV is chosen; all events in which the best PV is no longer present after the offline  
 498 selection are removed. Finally, since the remaining  $B^0$  candidates are considered to be  
 499 equally likely signal candidates, one remaining  $B^0$  candidate is chosen randomly.

### 4.2.8 Selection performance

The offline selection performances are listed in Tab. 4.6. They are determined by using data candidates of the 2012 sample with an invariant  $B^0$  mass above 5500 MeV/ $c^2$  to represent combinatorial background, and signal MC candidates (see Sec. 4.3) to represent the signal. In fig. 4.12 a comparison of the mass distribution of the selected 2011 and 2012 data is shown. Additionally, the BDT performances are quoted in Tab. 4.7 split

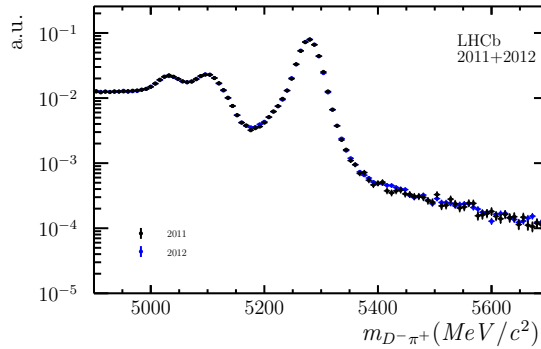


Figure 4.12 –  $B$ mass distributions for the 2011 (blue) and 2012 (black) samples after the full offline selection.

Table 4.6 – Offline selection performances. The signal efficiencies and background rejections of the different selection steps are given with respect to the previous selection step, while the last row shows the overall selection performance.

Selection step	$\varepsilon_{\text{sig}}$	$1 - \varepsilon_{\text{bkg}}$
preselection	$(93.61 \pm 0.06) \%$	$(85.20 \pm 0.02) \%$
$\Lambda_c^\pm$ -veto	$(93.48 \pm 0.06) \%$	$(9.85 \pm 0.03) \%$
semileptonic veto	$(98.96 \pm 0.03) \%$	$(7.66 \pm 0.03) \%$
mass vetoes combined	$(92.51 \pm 0.07) \%$	$(16.77 \pm 0.04) \%$
wrongly associated PVs veto	$(97.75 \pm 0.04) \%$	$(15.81 \pm 0.04) \%$
BDT selection	$(83.63 \pm 0.10) \%$	$(97.18 \pm 0.01) \%$
total	$(70.7 \pm 0.1) \%$	$(99.911 \pm 0.002) \%$

by both polarity and year of data taking. Finally, in order to check the contribution of non-resonant decays  $B^0 \rightarrow K^+\pi^-\pi^-\pi^+$ , the  $B^0$  and  $D^-$  invariant mass distributions are analysed after applying the full offline selection in two ways. First, the  $D^-$  mass distribution after applying a signal window cut on the  $B^0$  mass is plotted (Fig. 4.13). From this plot, the maximal contamination with non-resonant decays can be estimated as roughly 1 %. Then, the  $B^0$  distribution after excluding the  $D^-$  signal window is plotted. To quantify the non-resonant  $B^0 \rightarrow K^+\pi^-\pi^-\pi^+$  decays, the sum of an exponential and a

## 4.2. Data sample and selection

Table 4.7 – BDT performance split by polarity and year of data taking. The given efficiencies contain signal and background.

	2011, MU	2011, MD	2012, MU	2012, MD
# cand. before BDT	398 357	569 853	1 301 800	1 316 597
# cand. after BDT	210 844	285 137	601 345	609 880
$\varepsilon_{\text{sig+bkg}}$	(50.67 $\pm$ 0.08) %	(50.04 $\pm$ 0.07) %	(46.19 $\pm$ 0.04) %	(46.32 $\pm$ 0.04) %

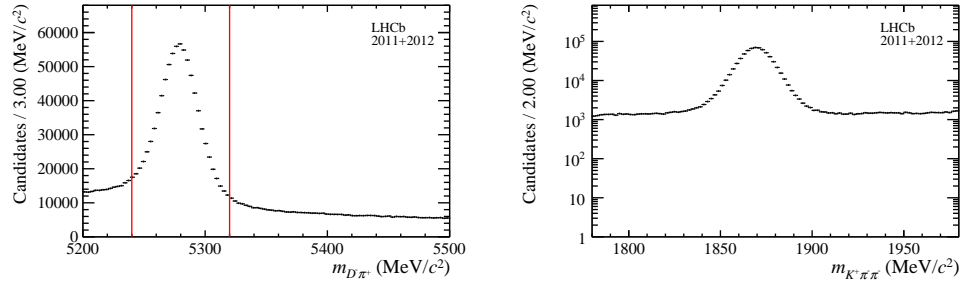


Figure 4.13 – Left:  $B^0$  mass distribution. The red vertical lines indicate the selected signal window. Right: resulting  $D^-$  mass distribution.

513 Gaussian with a fixed shape is used to fit the resulting  $B^0$  mass distribution, as shown in  
 514 Fig. 4.14. As the fitted  $B^0$  yield is  $645 \pm 242$ , the non-resonant contribution is assumed  
 to be negligible.

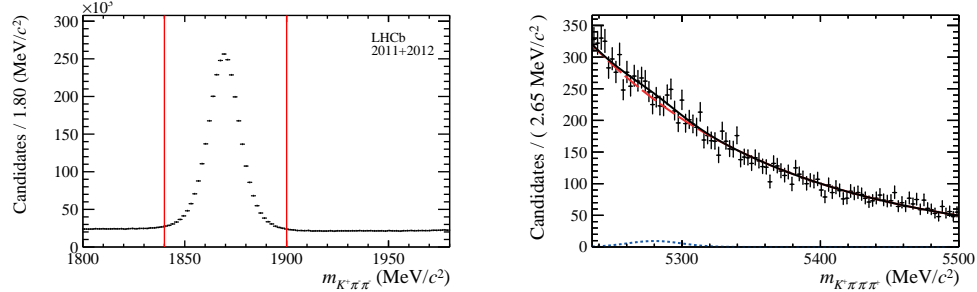


Figure 4.14 – Left:  $D^-$  mass distribution, The red vertical lines indicate the excluded range. Right: resulting  $B^0$  mass distribution with the fitting function overlaid.

515

### 516 4.3 Simulation and expected sample composition

517 Simulated samples are used to (i) gain a detailed overview of all sources of  $b$ -hadron  
 518 decays that contribute to the sample and (ii) model the relevant distributions studied  
 519 in the analysis. Simulated data undergoes the same processing of reconstruction and  
 520 selection as real data. Each sample is split into "up" and "down" magnet polarities and  
 521 into 2011 and 2012 data taking conditions subsamples, in proportions similar to those  
 522 present in real data.

523 The used simulated samples are listed in Tab. 4.8, together with the number of true signal  
 524 events passing the final selection and the corresponding total efficiencies. Any PID cut  
 on the bachelor cut is applied in order to compute these efficiencies.

Sample	Event type	$N_{\text{sel}}$	Efficiency [%]
$B^0 \rightarrow D\pi$	11164003	101096	$1.966 \pm 0.006$
$B^0 \rightarrow DK$	11264011	19300	$1.833 \pm 0.013$
$B^0 \rightarrow D\rho$	11164401	2408	$0.1178 \pm 0.0024$
$B^0 \rightarrow D^*\pi$	11164404	14901	$0.721 \pm 0.006$
$B_s^0 \rightarrow D_s^+\pi^-$	13264021	7942	$0.1531 \pm 0.0017$
$\Lambda_b^0 \rightarrow \Lambda_c^0\pi^-$	15164001	325	$0.0155 \pm 0.0009$
$B^0 \rightarrow DK^*$	11164470	361	$0.0358 \pm 0.0019$

Table 4.8 – Samples of simulated data used in the analysis, number of candidates,  $N_{\text{sel}}$ , after selection, and selection efficiency. Efficiencies include generator level, stripping, offline selection and tagging efficiencies.

525

#### 526 4.3.1 PIDK correction

527 The PIDK distributions in data and MC differ. To correct for that, the PIDK distributions  
 528 in MC are resampled using the PIDK distributions of dedicated calibration samples as  
 529 (binned) probability density functions. These calibration samples consist of kinematically-  
 530 clean  $D^* \rightarrow D^0(\rightarrow K^-\pi^+)\pi^+$  data, for which no requirement on RICH information is  
 531 applied in the reconstruction.

532 The need for this resampling is due to the fact that, if the same cut is applied on data and  
 533 MC, the resulting distributions in other observables may differ if the PIDK distributions  
 534 in data and MC are different. Moreover, a correct PIDK distribution in MC allow to  
 535 properly estimate (on MC) the efficiency or misidentification rate for a given PIDK cut,  
 536 which is an essential ingredient in the fit to the  $B$  invariant mass distribution (as described  
 537 in Sec. 4.4).

538 The following strategy is adopted. A two-dimensional binning in momentum,  $p$ , and  
 539 pseudorapidity,  $\eta$ , is defined. For each bin, the corresponding PIDK distribution in the

### 4.3. Simulation and expected sample composition

---

540 calibration sample is built and for each event in the MC sample, a random PIDK value is  
541 sampled from the PIDK distribution associated to the corresponding bin in the calibration  
542 sample. More details are given in Appendix 4.6.

543 Because of the  $\Lambda_c$  veto described in Sec. 4.2.3, the PIDp variable for the  $D$  daughter  
544 particles is resampled as well in a similar manner using  $\Lambda^0 \rightarrow p\pi^-$  decays as calibration  
545 samples.

#### 546 4.3.2 Surviving physics backgrounds

547 Some physics background candidates that survive the selection chain described in the  
548 previous section are expected. In the pion sample, these are:

- 549     •  $B^0 \rightarrow D^\mp K^\pm$ : Peaking background due to the bachelor kaon being wrongly  
550         identified as a pion.
- 551     •  $B^0 \rightarrow D^\mp \rho^\pm (\rightarrow \pi^\pm \pi^0)$ : Low mass background due to missing a pion in the  
552         reconstruction.
- 553     •  $B^0 \rightarrow D^{\mp *}( \rightarrow D^\mp \gamma/\pi^0) \pi^\pm$ : Low mass background due to a missed neutral  
554         particle.

555 In the kaon sample, the following backgrounds are expected:

- 556     •  $B^0 \rightarrow D^\mp \pi^\pm$ : Signal candidates having the bachelor pion wrongly identified as a  
557         kaon.
- 558     •  $B^0 \rightarrow D^\mp \rho^\pm (\rightarrow \pi^\pm \pi^0)$ : Low mass background where, in addition to the missed  
559         pion in the final state, a reconstructed pion is wrongly identified as a kaon.
- 560     •  $B^0 \rightarrow D^\mp K^{\pm *} (\rightarrow \pi^0 K^\pm)$ : Low mass background where the neutral pion is missed  
561         in the final state.

562 The fraction of the backgrounds expected in the pion sample with respect to the  $B^0 \rightarrow D\pi$   
563 signal are reported in Tab. 4.9. These fractions are computed using the branching fractions  
564 of the expected decay as inputs and from the ratio of efficiencies estimated from MC  
565 (when relevant we consider also the ratio of the fragmentation probabilities of  $b$  quarks to  
566 different  $b$  hadron). These expectation will be compared with the results from the fit to  
567 data described in the next section.

568 The  $B_s \rightarrow D_s \pi$  and  $\Lambda_b \rightarrow \Lambda_c (\rightarrow p K \pi) \pi$  backgrounds are suppressed to a negligible  
569 fraction by the offline selection described in Sec. 4.2, and are thus ignored in the description

Decay	$\mathcal{B}$ [%]	$\epsilon_{\text{bkg}}$ [%]	$f_{Bz/B_s^0/\Lambda_b^0}$ [%]	$f_{\text{bkg}}$ [%]
$B^0 \rightarrow DK$	$0.00186 \pm 0.00020$	$0.684 \pm 0.008$	$33.9 \pm 3.9$	$2.61 \pm 0.31$
$B^0 \rightarrow D\rho(\rightarrow \pi\pi)$	$0.071 \pm 0.011$	$0.1149 \pm 0.0024$	$33.9 \pm 3.9$	$16.7 \pm 2.8$
$B^0 \rightarrow D^*(\rightarrow D\gamma/\pi^0)\pi$	$0.0080 \pm 0.0004$	$0.705 \pm 0.006$	$33.9 \pm 3.9$	$11.6 \pm 0.8$
$\Lambda_b \rightarrow \Lambda_c(\rightarrow pK\pi)\pi$	$0.032 \pm 0.004$	$0.0150 + / - 0.0008$	$21.2 \pm 6.9$	$0.62 \pm 0.24$
$B_s \rightarrow D_s\pi$	$0.019 \pm 0.013$	$0.1493 \pm 0.0017$	$11.1 \pm 1.4$	$1.9 \pm 1.3$

Table 4.9 – Background contributions expected in the pion sample. The  $B^0 \rightarrow D\pi$  branching ratio and total selection efficiency in the pion sample are  $(0.254 \pm 0.014)\%$  and  $(1.966 \pm 0.006)\%$  respectively.

570 of the sample composition. Moreover, in the kaon sample, the  $B^0 \rightarrow D^*\pi$  and  $B^0 \rightarrow D^*K$   
 571 components, which are expected to be negligible, are neglected as well <sup>1</sup>.

---

<sup>1</sup>More precisely, these components are taken into account by the PDF describing  $B^0 \rightarrow DK^*(\rightarrow \pi^0 K)$ , since they are expected to sit in the same mass region.

---

## 572 4.4 Fits to the $B^0$ invariant mass

573 The *sPlot* technique [54] is applied in order to statistically disentangle signal from  
 574 background for the decay time fit. The  $D\pi$  invariant mass, where the  $D$  mass is constrained  
 575 to its known value in order to improve the mass resolution, is adopted as discriminating  
 576 observable thanks to its low correlation with the  $B^0$  decay time (see Appendix 4.7).

In a first step, a binned extended maximum likelihood fit (“Fit A”) is performed in order to define the PDFs describing signal and background components. The choice of a binned fit is justified by the very high statistics of the data sample. The invariant mass range of the fit is [5090, 6000] MeV/ $c^2$ . Only tagged candidates are considered, i.e. candidates with at least a nonzero tagging decision among OS or SS taggers. The reason for this is that untagged candidates do not contribute to the sensitivity on CP-coefficients. The fit is performed simultaneously for the pion sample and the kaon sample (see section 4.2.2). This approach is adopted in order to control the contamination of  $B^0 \rightarrow DK$  background in the pion sample. The number of  $B^0 \rightarrow DX$  candidates in the  $Y$  sample (with  $X, Y = \pi, K$ ),  $N_{B^0 \rightarrow DX}^Y$ , can be defined via the following relations:

$$\begin{aligned} N_{B^0 \rightarrow D\pi}^K &= \frac{\epsilon_{\text{PID}}(B^0 \rightarrow D\pi)_K}{\epsilon_{\text{PID}}(B^0 \rightarrow D\pi)_\pi} \times N_{B^0 \rightarrow D\pi}^\pi \\ &= \frac{1 - \epsilon_{\text{PID}}(B^0 \rightarrow D\pi)_\pi}{\epsilon_{\text{PID}}(B^0 \rightarrow D\pi)_\pi} \times N_{B^0 \rightarrow D\pi}^\pi, \end{aligned} \quad (4.7)$$

$$\begin{aligned} N_{B^0 \rightarrow DK}^\pi &= \frac{\epsilon_{\text{PID}}(B^0 \rightarrow DK)_\pi}{\epsilon_{\text{PID}}(B^0 \rightarrow DK)_K} \times N_{B^0 \rightarrow DK}^K \\ &= \frac{1 - \epsilon_{\text{PID}}(B^0 \rightarrow DK)_K}{\epsilon_{\text{PID}}(B^0 \rightarrow DK)_K} \times N_{B^0 \rightarrow DK}^K. \end{aligned} \quad (4.8)$$

577 The quantities  $\epsilon_{\text{PID}}(B^0 \rightarrow DX)_Y$  are the fractions of true  $B^0 \rightarrow DX$  candidates that  
 578 are selected in the  $Y$  sample by applying the relative PIDK cut. These fractions (or  
 579 efficiencies) are estimated on  $B^0 \rightarrow D\pi$  and  $B^0 \rightarrow DK$  MC samples where the PIDK  
 580 distributions are resampled from calibration data, as described in section 4.3.1; the results  
 581 of these estimations are reported in table 4.10.

Table 4.10 – Fractions of true  $B^0 \rightarrow D\pi$  and  $B^0 \rightarrow DK$  decays that are selected in the  $\pi$  or  $K$  sample.

Sample	PIDK cut	fraction
$B^0 \rightarrow D\pi$	< 5.0 ( $\pi$ sample)	$0.979 \pm 0.004$
$B^0 \rightarrow D\pi$	> 5.0 ( $K$ sample)	$0.0211 \pm 0.0005$
$B^0 \rightarrow DK$	< 5.0 ( $\pi$ sample)	$0.373 \pm 0.005$
$B^0 \rightarrow DK$	> 5.0 ( $K$ sample)	$0.637 \pm 0.007$

Finally, an unbinned extended maximum likelihood fit (“Fit B”) is performed on data using the reduced mass interval [5220, 5600] MeV/ $c^2$  in order to extract *sWeights*. In this second fit, all the parameters are fixed to the values found in Fit A, except for the normalisations. The reduced mass window avoids diluting the *sWeights* with components that are neither combinatoric nor close to the signal component and therefore cannot be meaningfully subtracted. This has the added advantage of reducing the dataset size used in the decay time fit.

#### 4.4.1 Probability density functions

Before Fit A, the PDFs used to describe both the pion and kaon sample composition are first estimated on MC samples. The parameters of the combinatorial background PDFs are instead determined directly on data. The PDFs used for the pion sample are:

- $B^0 \rightarrow D\pi$ : sum of a double-sided Hypatia [55] and a Johnson SU [56] functions ( $PDF_{B^0 \rightarrow D\pi}^\pi$ ).
- $B^0 \rightarrow DK$ : double-sided Hypatia function ( $PDF_{B^0 \rightarrow DK}^\pi$ ).
- $B^0 \rightarrow D\rho$ : Johnson SU function ( $PDF_{B^0 \rightarrow D\rho}^\pi$ ).
- $B^0 \rightarrow D^*\pi$ : sum of a single-sided Crystal Ball function [57] and a Gaussian function ( $PDF_{B^0 \rightarrow D^*\pi}^\pi$ ).
- Combinatorial: sum of an exponential and a constant function.

For the kaon sample they are:

- $B^0 \rightarrow D\pi$ : double-sided Hypatia function ( $PDF_{B^0 \rightarrow D\pi}^K$ ).
- $B^0 \rightarrow DK$ : single-sided Hypatia function ( $PDF_{B^0 \rightarrow DK}^K$ ).
- $B^0 \rightarrow D\rho$ : double Gaussian function ( $PDF_{B^0 \rightarrow D\rho}^K$ ).
- $B^0 \rightarrow DK^*$ : Gaussian function ( $PDF_{B^0 \rightarrow DK^*}^K$ ).
- Combinatorial: sum of an exponential and a constant function.

The definitions of all the PDFs listed above are reported in Appendix 4.8. The fits to the MC samples are shown in figs. 4.15 and 4.16.

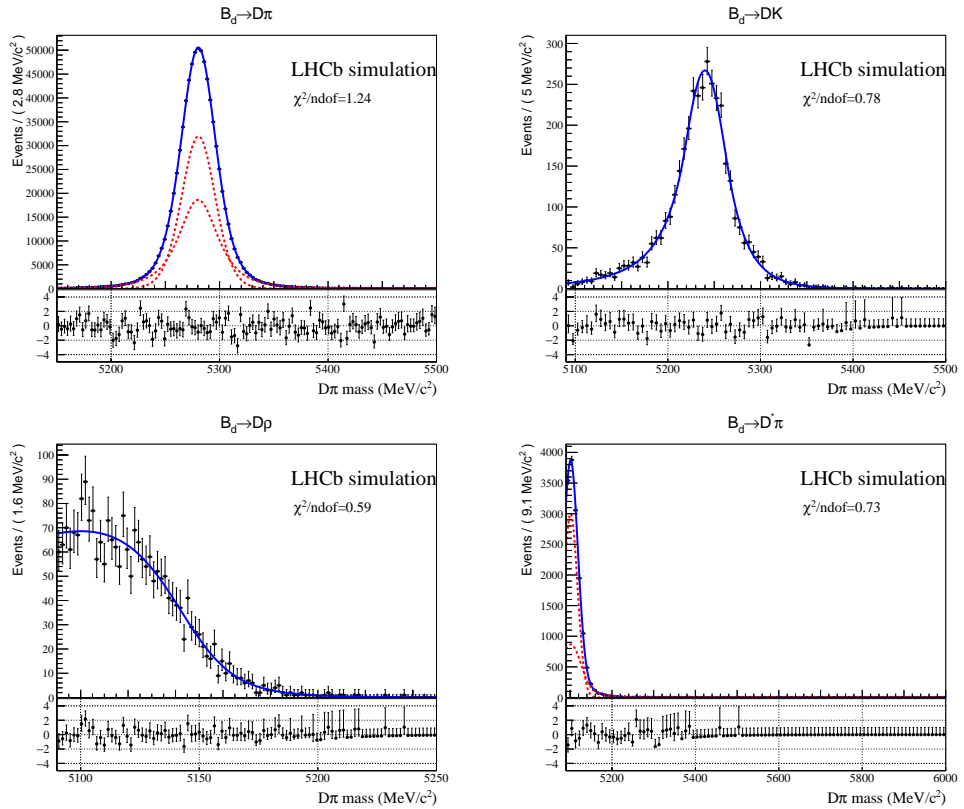


Figure 4.15 – Fits to MC samples of PDFs describing the  $\pi$  sample composition.

#### 608 4.4.2 Fit to data

In order to perform Fit A, two extended PDFs are defined as follows:

$$\begin{aligned} PDF_\pi &= N_{B^0 \rightarrow D\pi}^\pi PDF_{B^0 \rightarrow D\pi}^\pi + N_{B^0 \rightarrow DK}^\pi PDF_{B^0 \rightarrow DK}^\pi \\ &+ N_{B^0 \rightarrow D^*\pi}^\pi PDF_{B^0 \rightarrow D^*\pi}^\pi + N_{B^0 \rightarrow D\rho}^\pi PDF_{B^0 \rightarrow D\rho}^\pi \\ &+ N_{\text{comb}}^\pi PDF_{\text{comb}}^\pi. \end{aligned} \quad (4.9)$$

$$\begin{aligned} PDF_K &= N_{B^0 \rightarrow DK}^K PDF_{B^0 \rightarrow DK}^K + N_{B^0 \rightarrow D\pi}^K PDF_{B^0 \rightarrow D\pi}^K \\ &+ N_{B^0 \rightarrow D^*K}^K PDF_{B^0 \rightarrow D^*K}^K + N_{B^0 \rightarrow D\rho}^K PDF_{B^0 \rightarrow D\rho}^K \\ &+ N_{\text{comb}}^K PDF_{\text{comb}}^K. \end{aligned} \quad (4.10)$$

609 Two likelihood functions are defined using data and PDFs related to both sample,  $\mathcal{L}_\pi$   
610 and  $\mathcal{L}_K$ , and the product  $\mathcal{L}_\pi \mathcal{L}_K$  is maximised during the fit.

611 The following strategy is adopted to perform Fit A:

- 612 • The mean and width parameters ( $\mu_{B^0 \rightarrow D\pi}^\pi, \sigma I_{B^0 \rightarrow D\pi}^\pi, \sigma J_{B^0 \rightarrow D\pi}^\pi, \mu_{B^0 \rightarrow DK}^K, \sigma_{B^0 \rightarrow DK}^K$ )

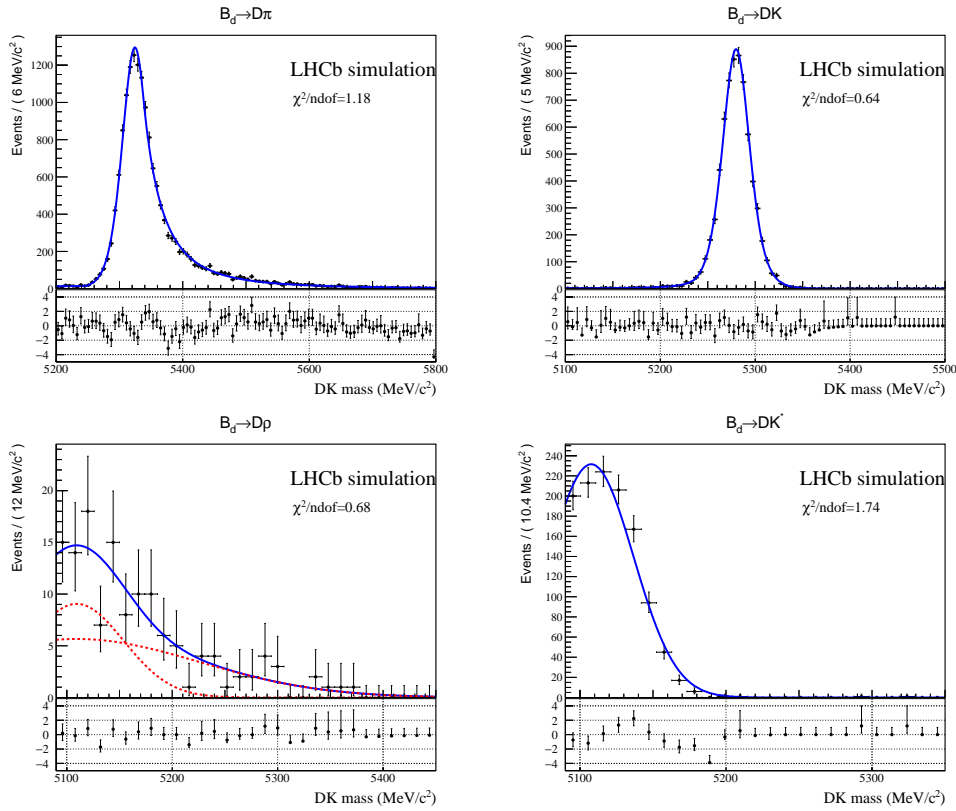


Figure 4.16 – Fits to MC samples of PDFs describing the  $K$  sample composition.

of  $PDF_{B^0 \rightarrow D\pi}^\pi$  and  $PDF_{B^0 \rightarrow DK}^K$  are floated in the fit.

- The tail parameters ( $a1_{B^0 \rightarrow D\pi}^\pi, a2_{B^0 \rightarrow D\pi}^\pi, n1_{B^0 \rightarrow D\pi}^\pi, n2_{B^0 \rightarrow D\pi}^\pi$ ) of  $PDF_{B^0 \rightarrow D\pi}^\pi$  are constrained in the following way:  $a1_{B^0 \rightarrow D\pi}^\pi, a2_{B^0 \rightarrow D\pi}^\pi$  are set to the values found on MC and both multiplied by a floating scale factor  $sa_{B^0 \rightarrow D\pi}^\pi$ ; the same constraint is applied to  $n1_{B^0 \rightarrow D\pi}^\pi, n2_{B^0 \rightarrow D\pi}^\pi$ , where the scale factor is labelled as  $sn_{B^0 \rightarrow D\pi}^\pi$
- The yield parameters  $N_{B^0 \rightarrow D\pi}^K$  and  $N_{B^0 \rightarrow DK}^\pi$  are constrained according to eqs. (4.7) and (4.8). The efficiencies  $\epsilon_{PID}(B^0 \rightarrow D\pi)_{D\pi}$  and  $\epsilon_{PID}(B^0 \rightarrow DK)_{DK}$  are Gaussian-constrained independently in the fit, using the values reported in Tab. 4.10 as constraint parameters. The yield  $N_{B^0 \rightarrow D\rho}^K$  is fixed to be 0.92 times the yield  $N_{B^0 \rightarrow DK^*}^K$ , the latter being floated in the fit. This is done according to the expected  $B^0 \rightarrow D\rho$  to  $B^0 \rightarrow DK^*$  ratio in the kaon sample, which is  $0.92 \pm 0.21$ . All the other yields appearing in Eqs. 4.9 and 4.10 are floated in the fit.
- The mean parameters ( $\mu_{B^0 \rightarrow D^*\pi}^\pi, \mu_{B^0 \rightarrow D\rho}^\pi$ ) of  $PDF_{B^0 \rightarrow D^*\pi}^\pi, PDF_{B^0 \rightarrow D\rho}^\pi$ , are constrained to be shifted from  $\mu_{B^0 \rightarrow D\pi}^\pi$  (in the  $\pi$  sample) and  $\mu_{B^0 \rightarrow DK}^K$  (in the  $K$  sample) by the same amount found in MC <sup>2</sup>. The mean parameters ( $\mu_{B^0 \rightarrow DK^*}^K$ ,

<sup>2</sup>The shift of the component with respect to the  $B^0 \rightarrow D\pi$  peak in the  $\pi$  sample/ $B^0 \rightarrow DK$  peak in the  $K$  sample is denoted as  $\Delta\mu_{comp}^{K/\pi}$ .

#### 4.4. Fits to the $B^0$ invariant mass

628        $\mu_{B^0 \rightarrow DK}^\pi, \mu_{B^0 \rightarrow D\pi}^K)$  of  $PDF_{B^0 \rightarrow DK}^K, PDF_{B^0 \rightarrow DK^*}^\pi, PDF_{B^0 \rightarrow DK}^\pi, PDF_{B^0 \rightarrow D\pi}^K$  are floated in the  
629       fit instead.

- 630       • The exponent parameters ( $c_{\text{comb}}^{\pi/K}$ ) and fractions ( $f_{\text{comb}}^{\pi/K}$ ) of  $PDF_{\text{comb}}^{\pi/K}$  are floated in  
631       the fit.

632       The projections of the fitted  $PDF_\pi$  and  $PDF_K$  PDFs in the  $D\pi$  and  $DK$  invariant mass  
633       observables (Fit A) are shown in fig. 4.17, together with the  $\pi$  and  $K$  data samples. A  
634       list of all the parameters fixed in the Fit A is given in Tab. ???. The fitted parameters  
      (including yields and PID efficiencies) are listed in Tab. 4.13.

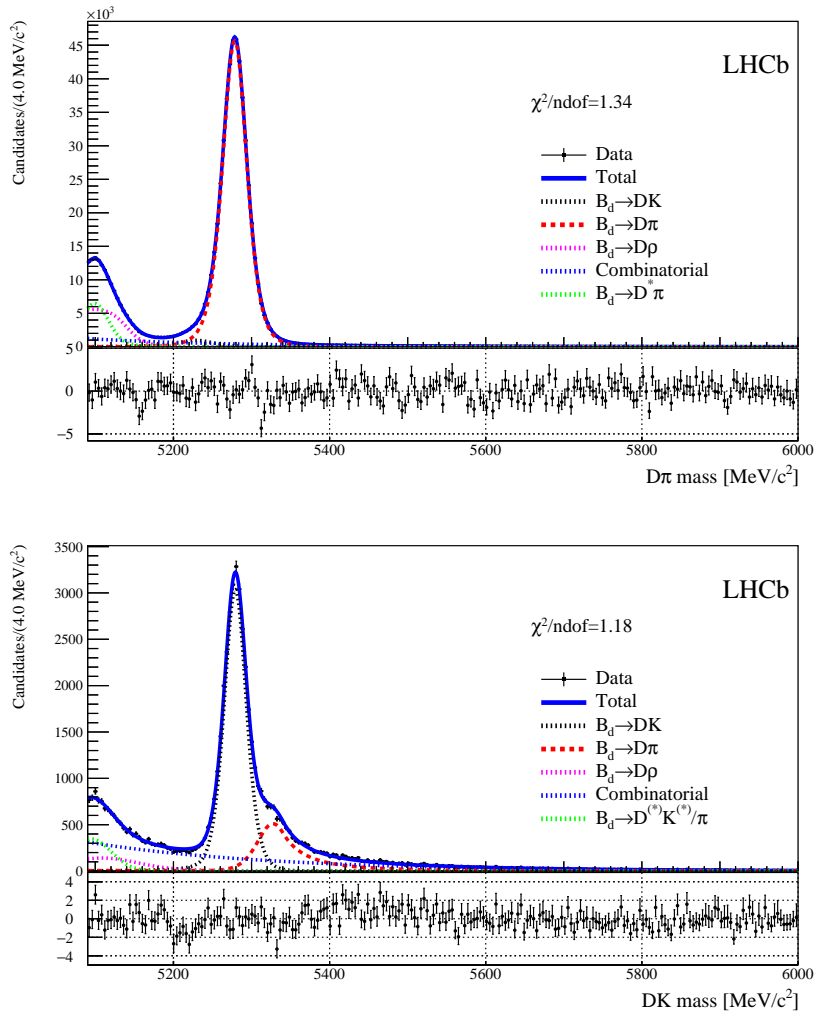


Figure 4.17 – Projections of the PDFs describing the  $\pi$  and  $K$  sample compositions fitted to the  $\pi$  and  $K$  data samples (Fit A).

Table 4.11 – Parameters of  $PDF_\pi$  fixed in Fit A. These values are obtained in the fits to MC samples described in Sec. 4.4.1.

Parameter name	Value	Comment
$a1_{B^0 \rightarrow D\pi}^\pi$	$0.722 \pm 0.091$	fitted in MC and constrained in data
$a2_{B^0 \rightarrow D\pi}^\pi$	$0.96 \pm 0.12$	fitted in MC and constrained in data
$n1_{B^0 \rightarrow D\pi}^\pi$	$5.92 \pm 0.92$	fitted in MC and constrained in data
$n2_{B^0 \rightarrow D\pi}^\pi$	$5.83 \pm 0.38$	fitted in MC and constrained in data
$\beta_{B^0 \rightarrow D\pi}^\pi$	0.0	fixed
$\lambda_{B^0 \rightarrow D\pi}^\pi$	$-1.240 \pm 0.060$	fitted in MC
$\zeta_{B^0 \rightarrow D\pi}^\pi$	0.0	fixed
$f_{B^0 \rightarrow D\pi}^\pi$	$0.436 \pm 0.060$	fixed
$\sigma_{B^0 \rightarrow DK}^\pi$	$23.43 \pm 0.42 \text{ MeV}/c^2$	fitted in MC
$a1_{B^0 \rightarrow DK}^\pi$	$0.898 \pm 0.025$	fitted in MC
$a2_{B^0 \rightarrow DK}^\pi$	$1.092 \pm 0.033$	fitted in MC
$n1_{B^0 \rightarrow DK}^\pi$	$3.83 \pm 0.40$	fitted in MC
$n2_{B^0 \rightarrow DK}^\pi$	$22.0 \pm 7.6$	fitted in MC
$\beta_{B^0 \rightarrow DK}^\pi$	0.0	fixed
$\lambda_{B^0 \rightarrow DK}^\pi$	$-24 \pm 10$	fitted in MC
$\zeta_{B^0 \rightarrow DK}^\pi$	0.0	fixed
$\nu_{B^0 \rightarrow D\rho}^\pi$	$-2.01 \pm 0.15$	fitted in MC
$\mu_{B^0 \rightarrow D\rho}^\pi$	$4828 \pm 80 \text{ MeV}/c^2$	fitted in MC and constrained into $\Delta\mu_{B^0 \rightarrow D\rho}^\pi$
$\sigma_{B^0 \rightarrow D\rho}^\pi$	$550 \pm 190 \text{ MeV}/c^2$	fitted in MC
$\tau_{B^0 \rightarrow D\rho}^\pi$	$1.163 \pm 0.090$	fitted in MC
$\alpha_{B^0 \rightarrow D^*\pi}^\pi$	$-1.443 \pm 0.031$	fitted in MC
$n_{B^0 \rightarrow D^*\pi}^\pi$	$4.65 \pm 0.30$	fitted in MC
$\mu_{B^0 \rightarrow D^*\pi}^\pi$	$5100.93 \pm 0.23 \text{ MeV}/c^2$	fitted in MC and constrained into $\Delta\mu_{B^0 \rightarrow D^*\pi}^\pi$
$\sigma G_{B^0 \rightarrow D^*\pi}^\pi$	$16.52 \pm 0.20 \text{ MeV}/c^2$	fitted in MC
$\sigma C B_{B^0 \rightarrow D^*\pi}^\pi$	$25.84 \pm 0.48 \text{ MeV}/c^2$	fitted in MC
$f_{B^0 \rightarrow D^*\pi}^\pi$	$0.302 \pm 0.011$	fitted in MC

Table 4.12 – Fixed parameters of  $PDF_K$  in Fit A. These values are obtained from the fits to MC samples described in Sec. 4.4.1.

Parameter name	Value	Comment
$\sigma_{B^0 \rightarrow D\pi}^K$	$23.97 \pm 0.46 \text{ MeV/c}^2$	fitted in MC
$a1_{B^0 \rightarrow D\pi}^K$	$3.14 \pm 0.14$	fitted in MC
$a2_{B^0 \rightarrow D\pi}^K$	$0.569 \pm 0.039$	fitted in MC
$n1_{B^0 \rightarrow D\pi}^K$	$0.05 \pm 0.11$	fitted in MC
$n2_{B^0 \rightarrow D\pi}^K$	$2.81 \pm 0.12$	fitted in MC
$\beta_{B^0 \rightarrow D\pi}^K$	0.0	fixed
$\lambda_{B^0 \rightarrow D\pi}^K$	$-3.77 \pm 0.57$	fitted in MC
$\zeta_{B^0 \rightarrow D\pi}^K$	0.0	fixed
$\sigma_{B^0 \rightarrow DK}^K$	$17.32 \pm 0.26 \text{ MeV/c}^2$	fitted in MC
$a_{B^0 \rightarrow DK}^K$	$2.34 \pm 0.19$	fitted in MC
$n_{B^0 \rightarrow DK}^K$	$1.56 \pm 0.33$	fitted in MC
$\beta_{B^0 \rightarrow DK}^K$	0.0	fixed
$\lambda_{B^0 \rightarrow DK}^K$	$-3.45 \pm 0.34$	fitted in MC
$\zeta_{B^0 \rightarrow DK}^K$	0.0	fixed
$f_{B^0 \rightarrow D\rho}^K$	$0.58 \pm 0.17$	fitted in MC
$\mu_{B^0 \rightarrow D\rho}^K$	$5109 \pm 24 \text{ MeV/c}^2$	fitted in MC and constrained into $\Delta\mu_{B^0 \rightarrow D\rho}^K$
$\sigma_{B^0 \rightarrow D\rho}^K$	$117 \pm 18 \text{ MeV/c}^2$	fitted in MC
$\sigma2_{B^0 \rightarrow D\rho}^K$	$45 \pm 16 \text{ MeV/c}^2$	fitted in MC

#### 636 4.4.3 $s$ Weight calculation

After that Fit A is performed, all the floating shape parameters in  $PDF_\pi$  are fixed, all the background components in the  $\pi$  sample are combined into a single PDF, and the  $B$  mass range is restricted to  $[5220, 5600] \text{ MeV/c}^2$ . Concretely,  $PDF_\pi$  is redefined as follows:

$$PDF_\pi = N_{B^0 \rightarrow D\pi}^\pi PDF_{B^0 \rightarrow D\pi}^\pi + N_{\text{bkg}}^\pi PDF_{\text{bkg}}^\pi. \quad (4.11)$$

The  $N_{\text{bkg}}^\pi$  coefficient describes the total number of background events in the new range. The  $PDF_{\text{bkg}}^\pi$  term is defined as:

$$\begin{aligned} PDF_{\text{bkg}}^\pi &= f_{\text{comb}}^\pi PDF_{\text{comb}}^\pi \\ &+ f_{B^0 \rightarrow DK}^\pi PDF_{B^0 \rightarrow DK}^\pi + f_{B^0 \rightarrow D\rho}^\pi PDF_{B^0 \rightarrow D\rho}^\pi \\ &+ (1 - f_{\text{comb}}^\pi - f_{B^0 \rightarrow DK}^\pi - f_{B^0 \rightarrow D\rho}^\pi) PDF_{B^0 \rightarrow D^*\pi}^\pi. \end{aligned} \quad (4.12)$$

Table 4.13 – Floating parameters of  $PDF_\pi$  and  $PDF_K$  in Fit A.

Parameter number	Parameter name	Fitted value	MC value
0	$\mu_{B^0 \rightarrow DK}^\pi$	$5228.25 \pm 0.90$	$5239.96 \pm 0.52$
1	$\sigma_{B^0 \rightarrow DK}^K$	$17.18 \pm 0.15$	$17.32 \pm 0.26$
2	$\mu_{B^0 \rightarrow DK^*}^K$	$5094.7 \pm 3.9$	$5107.7 \pm 2.2$
3	$\sigma_{B^0 \rightarrow DK^*}^K$	$25.6 \pm 2.6$	$28.9 \pm 1.2$
4	$c1_{\text{comb}}^\pi$	$-0.00111 \pm 0.00069$	/
5	$c2_{\text{comb}}^\pi$	$-0.00581 \pm 0.00021$	/
6	$f_{\text{comb}}^\pi$	$0.105 \pm 0.034$	/
7	$c_{\text{comb}}^K$	$-0.004394 \pm 0.000066$	/
8	$\mu_{B^0 \rightarrow DK}^K$	$5279.20 \pm 0.14$	$5279.84 \pm 0.20$
9	$\mu_{B^0 \rightarrow D\pi}^\pi$	$5278.348 \pm 0.031$	$5280.291 \pm 0.025$
10	$sa_{B^0 \rightarrow D\pi}^\pi$	$0.674 \pm 0.019$	1.0
11	$sn_{B^0 \rightarrow D\pi}^\pi$	$2.88 \pm 0.88$	1.0
12	$\sigma I_{B^0 \rightarrow D\pi}^\pi$	$37.86 \pm 0.68$	$43.9 \pm 4.9$
13	$\sigma J_{B^0 \rightarrow D\pi}^\pi$	$16.98 \pm 0.17$	$16.82 \pm 0.15$
14	$\mu_{B^0 \rightarrow D\pi}^K$	$5327.39 \pm 0.78$	$5324.37 \pm 0.44$
15	$\epsilon_{\text{PID}}(B^0 \rightarrow DK)_K$	$0.6279 \pm 0.0058$	$0.637 \pm 0.007$
16	$\epsilon_{\text{PID}}(B^0 \rightarrow D\pi)_\pi$	$0.98052 \pm 0.00040$	$0.979 \pm 0.004$
17	$N_{B^0 \rightarrow DK}^K$	$28859 \pm 241$	/
18	$N_{B^0 \rightarrow DK^*}^K$	$3169 \pm 110$	/
19	$N_{B^0 \rightarrow D\rho}^\pi$	$73600 \pm 1239$	/
20	$N_{B^0 \rightarrow D^*\pi}^\pi$	$52479 \pm 819$	/
21	$N_{\text{comb}}^K$	$17453 \pm 341$	/
22	$N_{\text{comb}}^\pi$	$56608 \pm 1306$	/
23	$N_{B^0 \rightarrow D\pi}^\pi$	$483767 \pm 1003$	/

For each background component in the  $\pi$  sample, the fraction  $f_{\text{comp}}^\pi$  is determined by the following expression:

$$f_{\text{comp}}^\pi = \frac{N_{\text{comp}}^\pi \int_{5220 \text{ MeV}/c^2}^{5600 \text{ MeV}/c^2} PDF_{\text{comp}}^\pi dm}{\sum_i N_i^\pi}, \quad (4.13)$$

where the index  $i$  in the denominator runs over all the background components in the  $\pi$  sample (combinatorial,  $B^0 \rightarrow DK$ ,  $B^0 \rightarrow D\rho$ ,  $B^0 \rightarrow D^*\pi$ ).

As cross-check, the fitted yields of  $B^0 \rightarrow DK$ ,  $B^0 \rightarrow D\rho$  and  $B^0 \rightarrow D^*\pi$  in the pion sample are compared with the expected yields from Table 4.9, which are obtained, for each background, by multiplying the fitted  $B^0 \rightarrow D\pi$  yield in the pion sample by the  $f_{\text{bkg}}$  fractions. These yields are reported in Table 4.14.

Once  $PDF_\pi$  is redefined as described above, an unbinned extended maximum likelihood fit (Fit B) is performed to the  $\pi$  sample. The only floating parameters are the yields

Table 4.14 – Expected and fitted yields for the physical background components in the pion sample. The uncertainties on the expected yields are propagated from 4.9.

Decay	Expected yield [ $10^4$ ]	Fitted yield [ $10^4$ ]
$B^0 \rightarrow DK$	$1.26 + / - 0.15$	$1.65 + / - 0.05$
$B^0 \rightarrow D\rho$	$8.1 + / - 1.4$	$7.36 + / - 0.12$
$B^0 \rightarrow D^*\pi$	$5.6 + / - 0.4$	$5.25 + / - 0.08$

Table 4.15 – Floating parameters of  $PDF_\pi$  in Fit B.

Parameter	Value
$N_{B^0 \rightarrow D\pi}^\pi$	$479325 \pm 729$
$N_{\text{bkg}}^\pi$	$34102 \pm 299$

645  $N_{B^0 \rightarrow D\pi}^\pi$  and  $N_{\text{bkg}}^\pi$ . The result of the fit is reported in Table 4.15.

646 Fit B is used as starting point to apply the *sPlot* technique and extract *sWeights* used  
 647 to subtract the total background component from the  $\pi$  sample. The projection of the  
 648 fitted  $PDF_\pi$  in Fit B, and a comparison between the weighted and unweighted datasets  
 649 projected over the  $B$  decay time and  $D$  invariant mass observables, are reported in  
 650 Fig 4.18. The distribution of *sWeights* is shown in fig. 4.19.

#### 651 4.4.4 Fit split by subsample

652 In order to validate the data sample, selection and fit procedure, the mass fit is repeated  
 653 in smaller subsamples. These subsamples are divided per year of data taking (2011, 2012),  
 654 magnet polarity (up, down) and final state ( $D^+\pi^-$ ,  $D^-\pi^+$ ).

655 In order to cope with the reduced statistics in the 2011 subsample and simplify the “Fit  
 656 A” strategy, the  $PDF_{\text{comb}}^K$  PDF is taken as simple exponential (instead of an exponential  
 657 plus constant function).

658 The projections of the PDFs describing the pion and kaon samples for each data subsample  
 659 (“Fit A”) are illustrated in Figs. 4.20 and 4.21 respectively.

660 The “Fit B” strategy is repeated exactly as before for each subsample. The corresponding  
 661 signal and background fitted yields are listed in Table 4.16. The sum of the yields for each  
 662 subsample has to be compared with the total signal yield in the total sample (reported in  
 663 Table 4.15), which is  $(4.793 \pm 0.007)10^5$ .

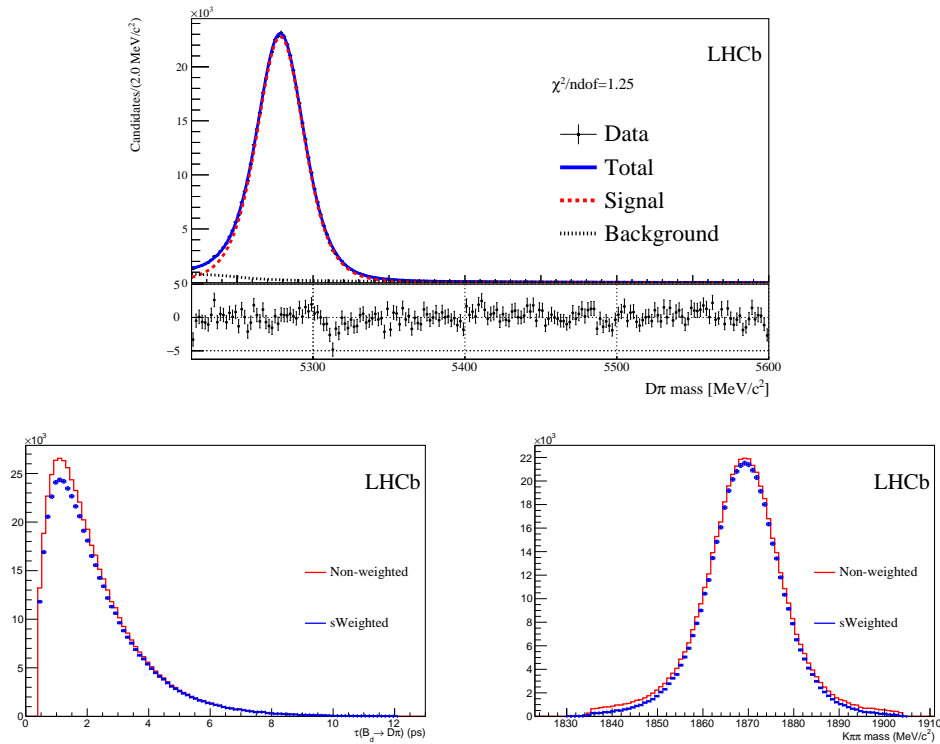


Figure 4.18 – *sWeighted* and unweighted  $\pi$  sample projected over  $B$  decay time and  $D$  invariant mass observables.

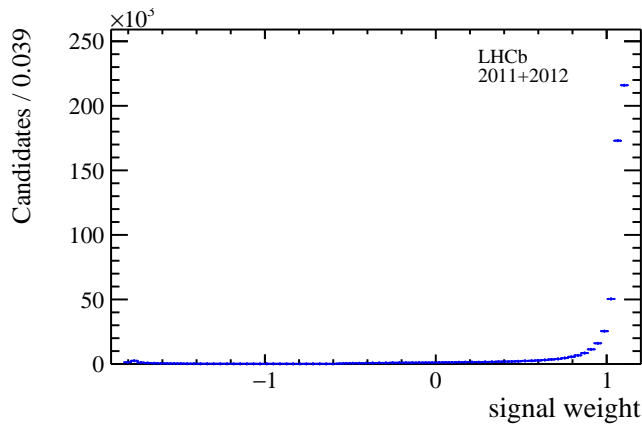


Figure 4.19 – Distribution of calculated *sWeights* by Fit B. No obvious outliers are visible.

#### 4.4. Fits to the $B^0$ invariant mass

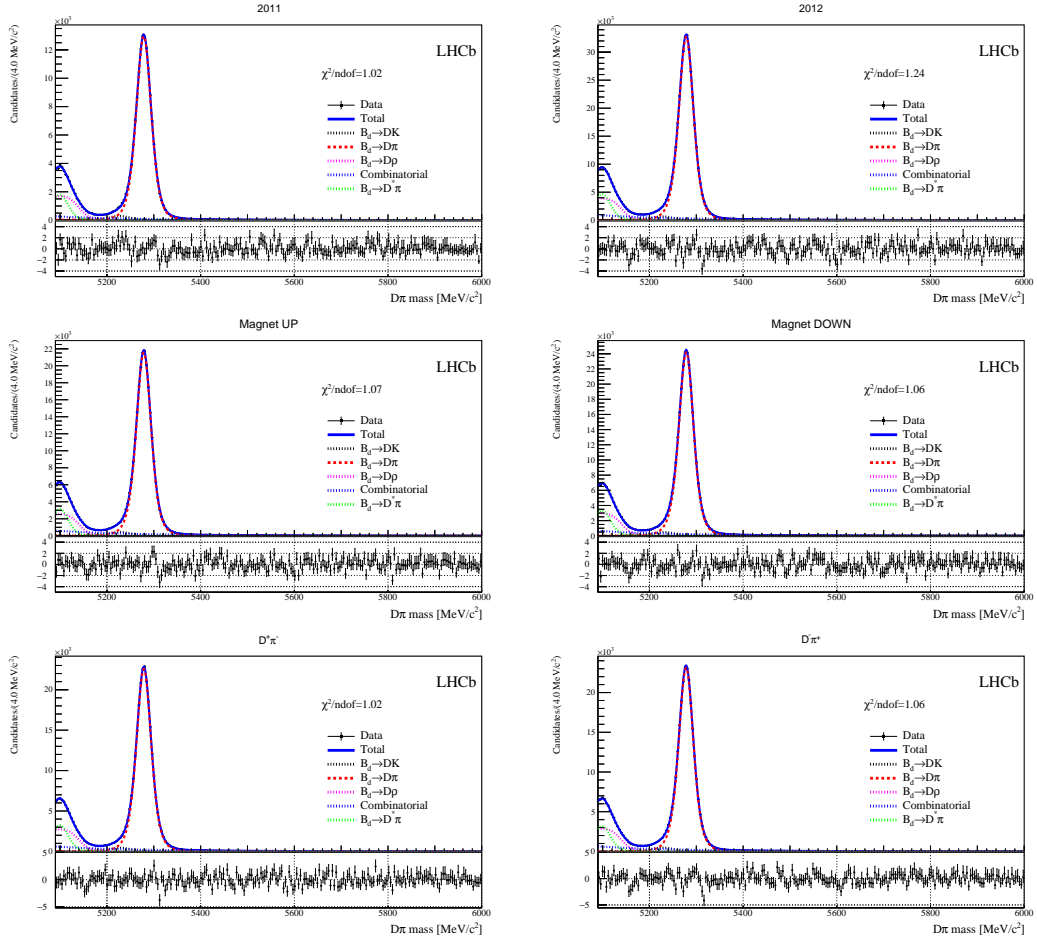


Figure 4.20 – Projections of the PDFs describing the pion sample for each data subsample.

Table 4.16 – Signal yields (in units of  $10^5$ ) in the pion sample for each subsample (obtained from “Fit B”).

	2011	2012	Sum
	$1.383 \pm 0.004$	$3.424 \pm 0.006$	$4.807 \pm 0.007$
Magnet Up	Magnet Down		Sum
$2.263 \pm 0.005$	$2.523 \pm 0.005$	$4.786 \pm 0.007$	
$D^- \pi^+$	$D^+ \pi^-$		Sum
$2.421 \pm 0.005$	$2.373 \pm 0.005$	$4.794 \pm 0.007$	

## Chapter 4. Measurement of CP violation in $B^0 \rightarrow D^\mp \pi^\pm$ decays

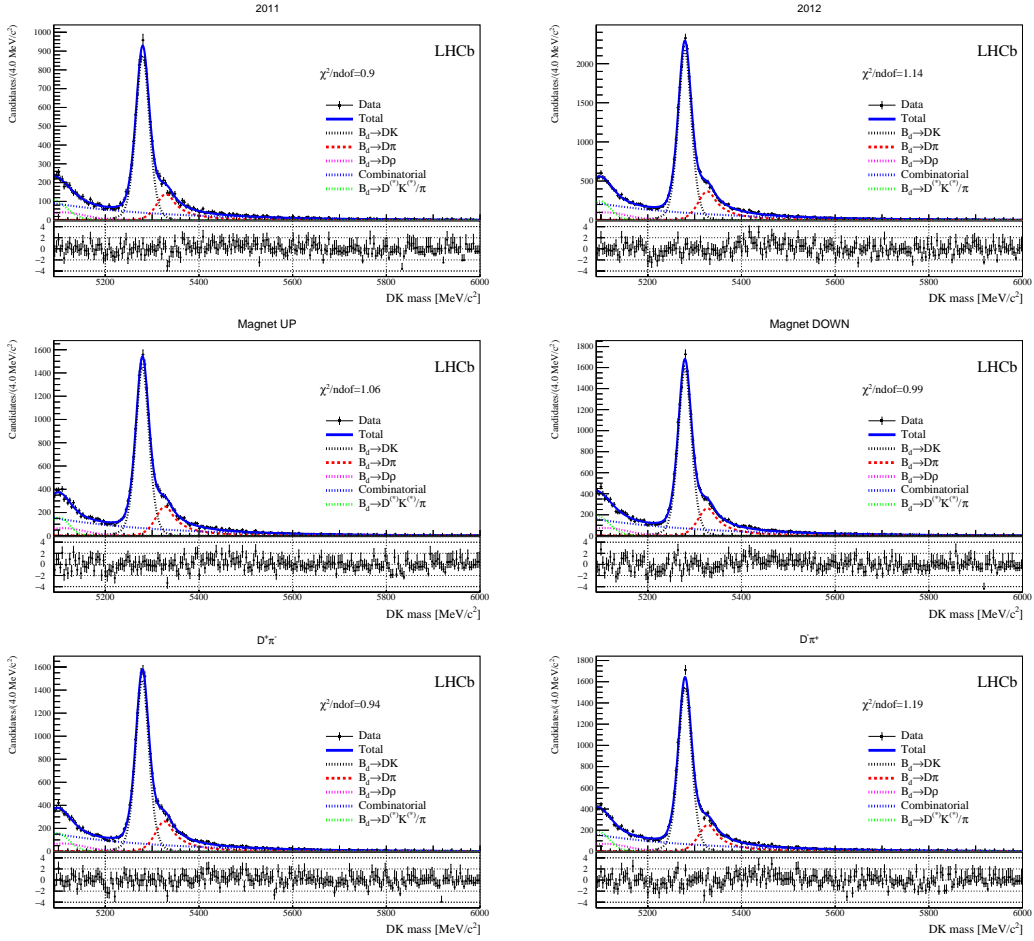


Figure 4.21 – Projections of the PDFs describing the kaon sample for each data subsample.

## Appendix

665 **4.5 Selection studies**

666 **4.5.1 BDT input features**

667 In the following section, the distributions of the input features for the BDT are shown.  
 668 Fig. 4.22 shows the cosine of the direction angle of the  $B^0$ , the  $\chi^2$  of the  $B^0$  vertex, the  
 669  $\chi^2/\text{ndof}$  of the  $D$  vertex, the  $D$  radial flight distance, the  $D$  flight distance  $\chi^2$  w.r.t. the  
 670  $B^0$  vertex and the transverse momentum of the  $D$ . In Fig. 4.23, the  $D$  IP $\chi^2$  with respect  
 671 to the associated PV and the  $B^0$  vertex, the cosine of the direction angle of the  $D$ , the  
 672 IP $\chi^2$  with respect to the associated PV of the bachelor pion, the track  $\chi^2/\text{ndof}$  of the  
 673 bachelor pion and the transverse momentum of the bachelor pion are shown. In Fig. 4.24,  
 674 the IP $\chi^2$  of the associated primary vertex of the  $D$  daughters and the  $\chi^2$  of the decay  
 tree fit with PV constraint are presented.

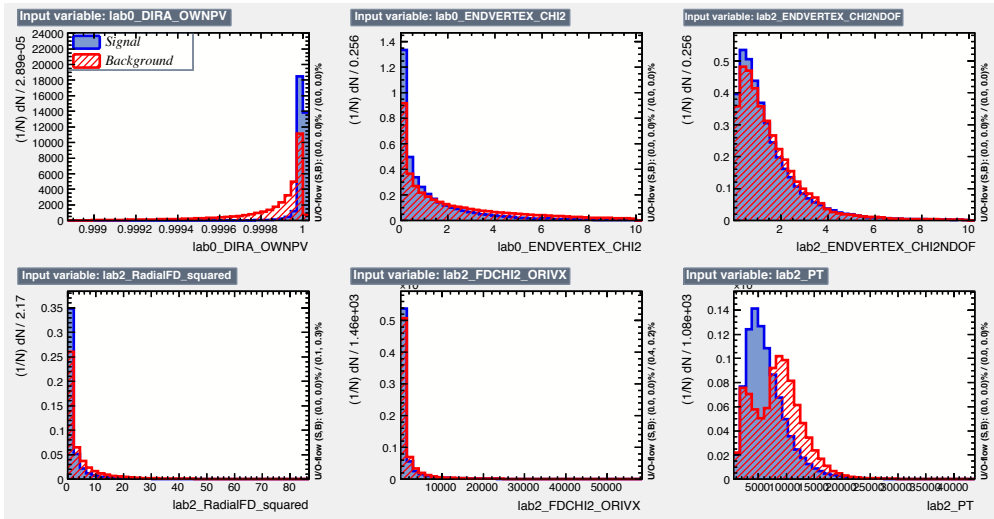


Figure 4.22 – Input features used in the BDT training. From top left to bottom right the cosine of the direction angle of the  $B^0$ , the  $\chi^2$  of the  $B^0$  vertex, the  $\chi^2/\text{ndof}$  of the  $D$  vertex, the  $D$  radial flight distance, the  $D$  flight distance  $\chi^2$  with respect to the  $B^0$  vertex and the transverse momentum of the  $D$  are shown.

675

676 **4.5.2 Multiple candidates**

677 In Tab. 4.17 a summary of multiple candidates left after the stripping selection is given,  
 678 while Tab. 4.18 reports the number of multiple candidates after both stripping and offline  
 679 selection.

## 4.5. Selection studies

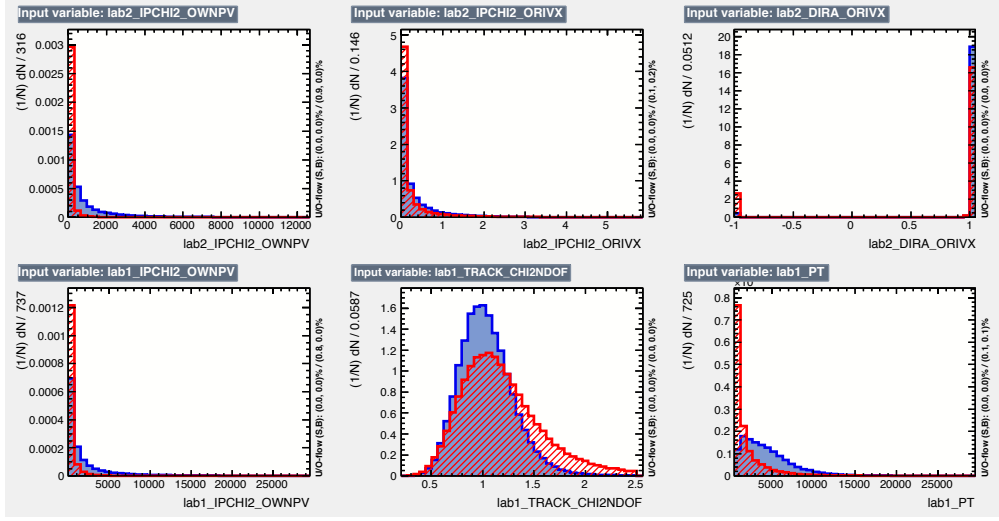


Figure 4.23 – Input features used in the BDT training. From top left to bottom right the  $D$  IP $\chi^2$  with respect to the associated PV and the  $B^0$  vertex, the cosine of the direction angle of the  $D$ , the IP $\chi^2$  with respect to the associated PV of the bachelor pion, the track  $\chi^2/\text{ndof}$  of the bachelor pion and the transverse momentum of the bachelor pion are shown.

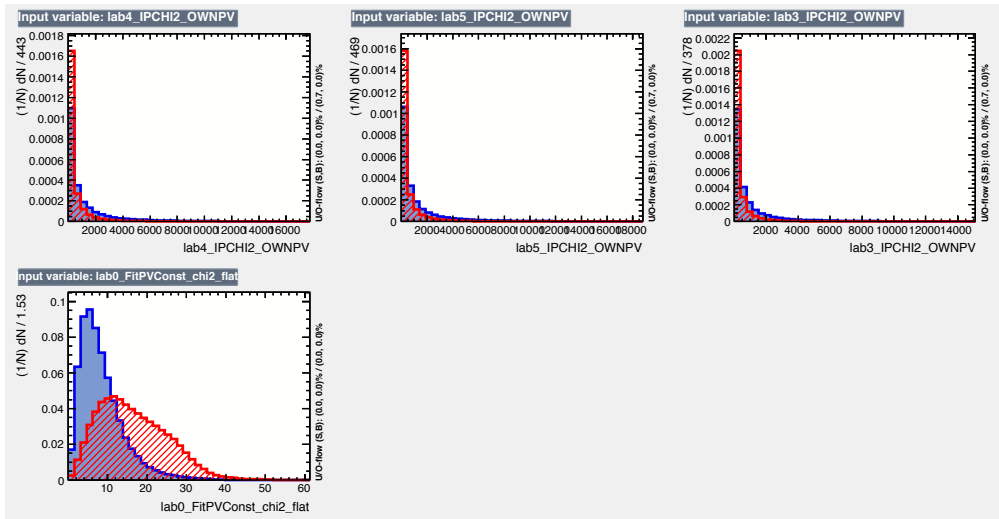


Figure 4.24 – Input features used in the BDT training. From top left to bottom right the IP $\chi^2$  of the associated primary vertex of the  $D$  daughters and the  $\chi^2$  of the decay tree fit with PV constraint are shown.

## Chapter 4. Appendix

---

Table 4.17 – Number of multiple  $B^0 \rightarrow D^\mp\pi^\pm$  candidates left after the stripping selection. The numbers in the first row represent the fraction of  $B^0$  candidates that are not unique in a given event. The numbers in the second row show the fraction of events with multiple  $B^0$  candidates. Additionally, a listing of the occurrence of events with different numbers of multiple  $B^0$  candidates is given. The last row shows the fraction of  $B^0$  candidates that need to be discarded to maintain one candidate per event.

	2011		2012	
fraction of multiple $B^0$ candidates	18.3 %		19.5 %	
fraction of events with multiple $B^0$ candidates	9.0 %		9.6 %	
	# $B^0$ cands	#events	# $B^0$ cands	#events
	1	5940804	1	16407228
	2	483991	2	1426286
	3	73902	3	226205
	4	20093	4	62640
	5	6132	5	19213
	6	2505	6	8044
	7	1087	7	3326
	8	528	8	1686
	9	251	9	839
	10	146	10	461
	11	78	11	279
	12	40	12	178
	13	28	13	109
	14	32	14	85
	15	10	15	53
	16	12	16	24
	17	7	17	16
	18	4	18	20
	19	5	19	9
	20	1	20	11
	21	3	21	5
	22	2	22	3
	23	0	23	2
	24	2	24	2
	25	1	25	1
	26	0	26	4
	30	0	30	1
	33	0	33	1
	40	1	40	0
	41	0	41	1
fraction of $B^0$ candidates to discard	10.1 %		11.0 %	

Table 4.18 – Number of multiple candidates left after both stripping and offline selection. The numbers in the first row represent the fraction of  $B^0$  candidates pairs that are not unique in an event. The numbers in the second row show the fraction of events with multiple  $B^0$  candidates. Additionally, a listing of the occurrence of events with different numbers of multiple  $B^0$  candidates is given. After that, the number of  $B^0$  candidates to discard is given.

	2011	2012		
fraction of multiple $B^0$ candidates	0.8 %	0.8 %		
fraction of events with multiple $B^0$ candidates	0.4 %	0.4 %		
	# $B^0$ cands	#events	# $B^0$ cands	#events
	1	483074	1	1200956
	2	1886	2	4962
	3	38	3	98
	4	4	4	9
	5	1	5	3
fraction of $B^0$ candidates to discard	0.4 %	0.4 %		

## 680 4.6 Particle Identification plots

681 The  $p$ ,  $\eta$  distributions and the PIDK efficiency, misidentification rates before the resampling  
 682 in bins of  $p$ ,  $\eta$  are shown in Figs. 4.25 and 4.26 for the bachelor particle of the signal,  
 and in Fig. 4.27 for the  $D^-$  daughters.

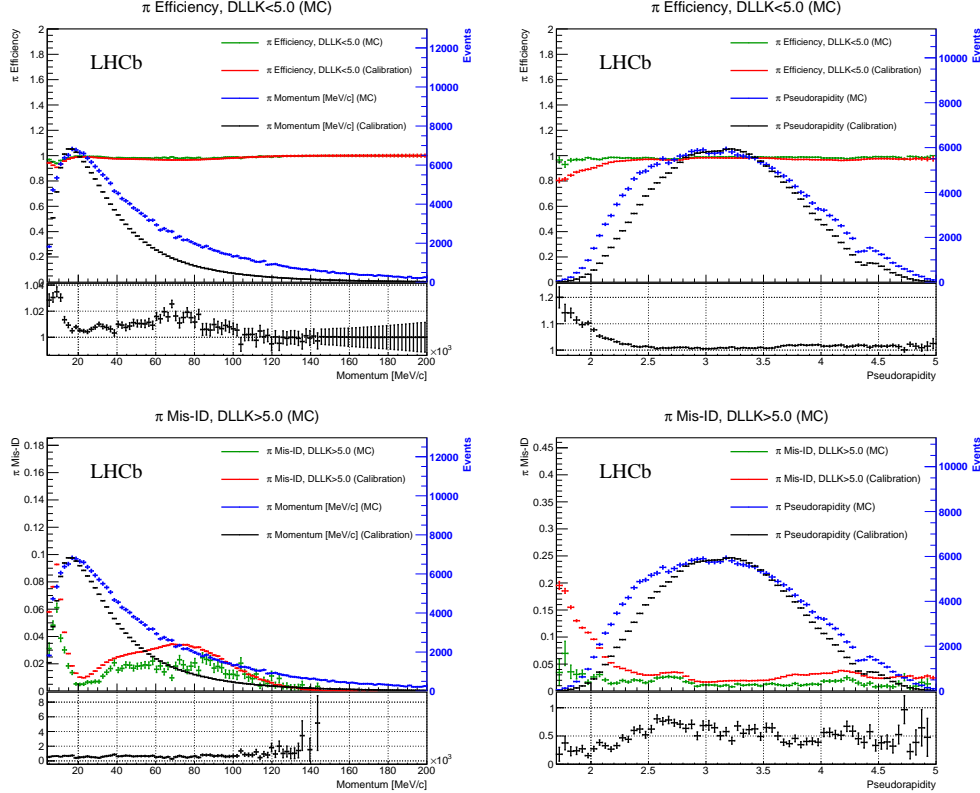


Figure 4.25 – PIDK efficiency or misidentification rates for bachelor pions and  $p$ ,  $\eta$  distributions before the resampling. Plots from calibration samples and Monte Carlo ( $B^0 \rightarrow D\pi$ ) are superimposed. The ratio of the efficiency or misidentification rate between Monte Carlo and calibration sample is shown in the lower pad (black).

## 4.6. Particle Identification plots

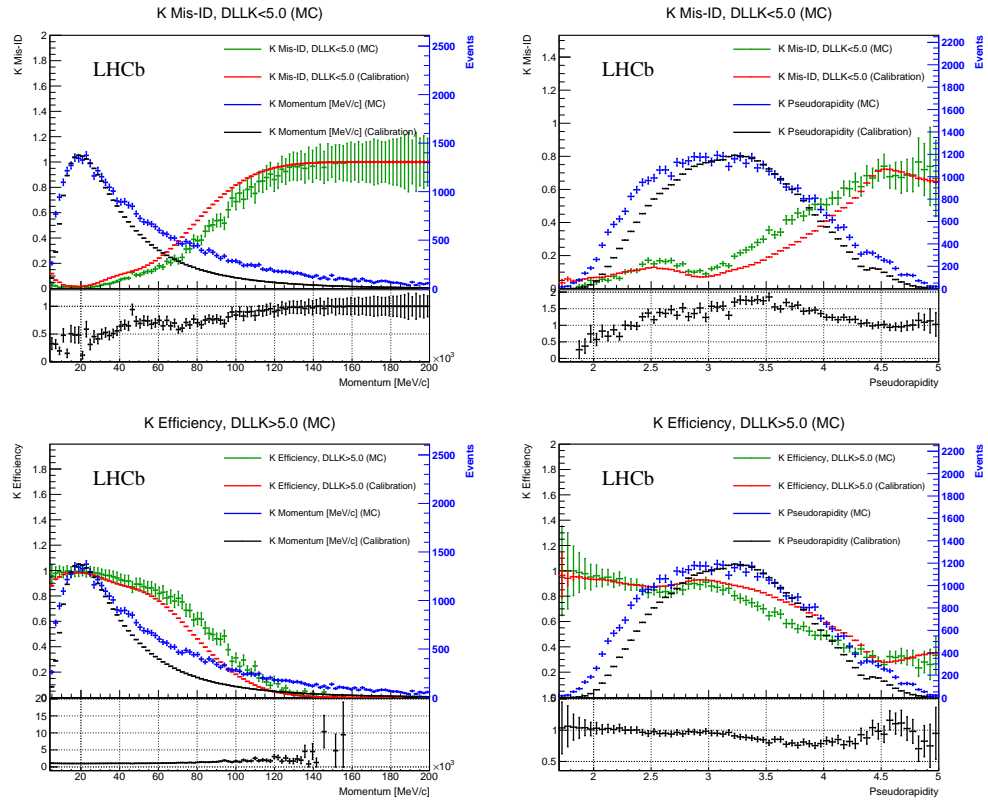


Figure 4.26 – PIDK efficiency or misidentification rates for bachelor kaons and  $p$ ,  $\eta$  distributions before the resampling. Plots from calibration samples and Monte Carlo ( $B^0 \rightarrow DK$ ) are superimposed. The ratio of the efficiency or misidentification rate between Monte Carlo and calibration sample is shown in the lower pad (black).

## Chapter 4. Appendix

---

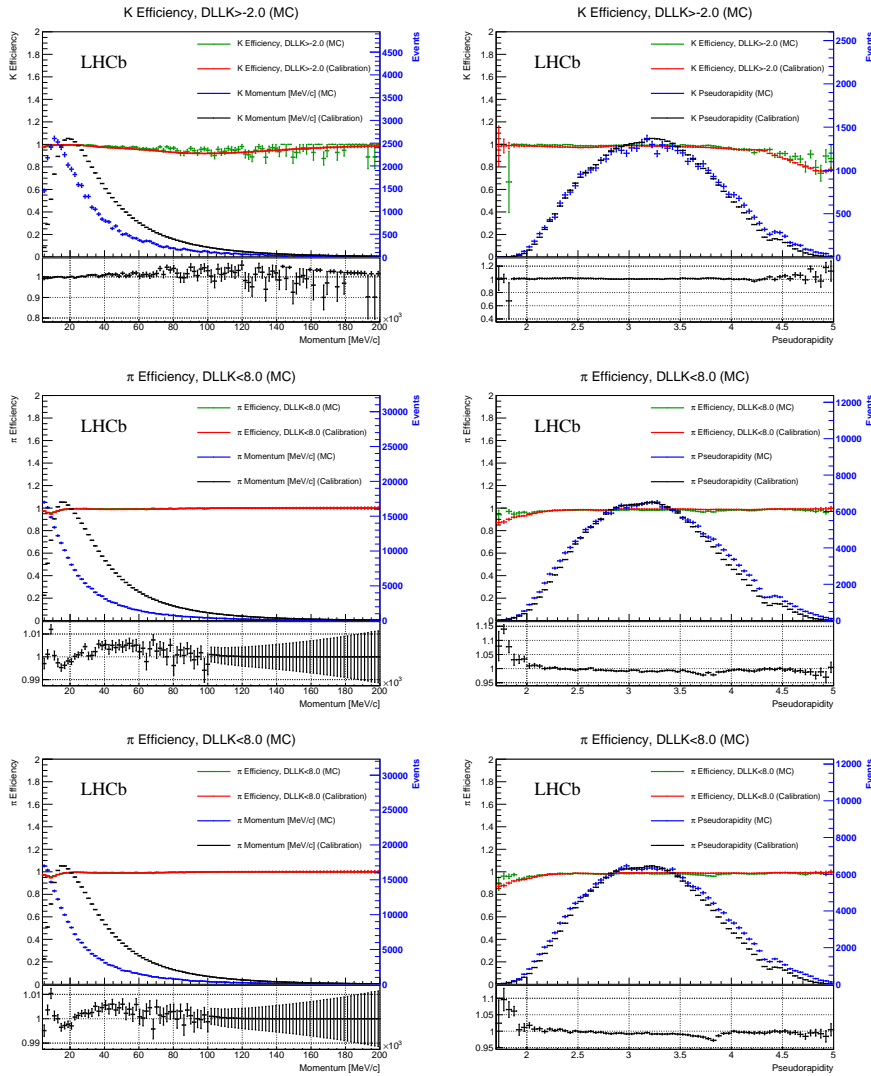


Figure 4.27 – PIDK efficiency, misidentification rates for  $D^-$  daughters (pions, kaons) and  $p, \eta$  distributions before the resampling. Plots from calibration samples and Monte Carlo ( $B_d \rightarrow DK$  and  $B_d \rightarrow D\pi$ ) are superimposed.

## 684 4.7 Invariant mass fit studies

685 The low correlation between the  $B^0$  invariant mass and decay time is shown by comparing  
 686 the distribution of the decay time in bins of the invariant mass after applying the full  
 687 selection. This is done separately for signal and background. For the signal distribution  
 688 simulated data is used and the decay time is shown in six bins of the invariant mass.  
 (fig. 4.28). In order to account for the combinatorial background, the upper mass sideband

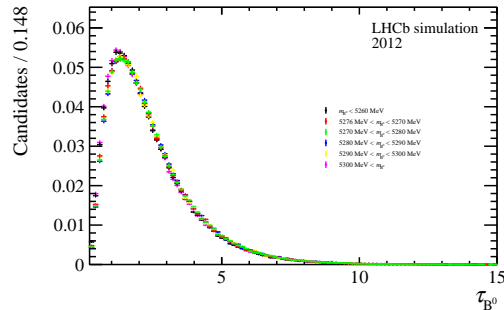


Figure 4.28 – Signal decay time distribution in divided in six bins of the invariant mass. The shapes are shown normalised.

689  
 690 is chosen as a proxy. Fig. 4.29 shows the decay time in four bins of the invariant mass.  
 691 The physics background contribution in the signal region is considered to be small enough,  
 so that even a large correlation does not matter. Given the small differences for all

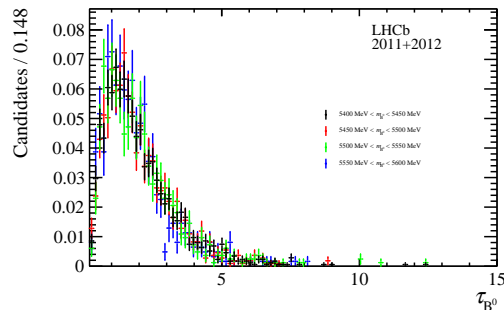


Figure 4.29 – Upper mass side band decay time distribution in divided in four bins of the invariant mass. The shapes are shown normalised.

692  
 693 distributions, the correlations between decay time and invariant mass is assumed to be  
 694 small enough that it's possible to use the invariant mass in the *sPlot* [54] technique for  
 695 disentangling signal from background.

## 696 4.8 PDFs definitions

697 Throughout the text, each parameter  $p$  defined inside a PDF used for the mass fit is  
698 labelled as  $p_c^s$ , where  $s = \pi, K$  indicates the sample and  $c = B^0 \rightarrow D\pi, B^0 \rightarrow D\rho \dots$   
699 indicates the component. For sake of clarity, the  $s$  and  $c$  labels are dropped in the  
700 equations that follow. The *observable* is always indicated as  $m$ . The  $\propto$  symbol indicates  
701 that all PDFs are defined up to a normalisation constant, which depends on the interval  
702 chosen for  $m$ .

- Exponential function

$$E(m, c) \propto e^{-cm}. \quad (4.14)$$

- Gaussian function

$$G(m, \mu, \sigma) \propto e^{-\frac{(m-\mu)^2}{2\sigma^2}}.$$

- Double Gaussian function

$$DG(m, \mu, \sigma_1, \sigma_2, f) \propto fe^{-\frac{(m-\mu)^2}{2\sigma_1^2}} + (1-f)e^{-\frac{(m-\mu)^2}{2\sigma_2^2}}.$$

- Single-sided Crystal ball function

Having defined the following parameters:

$$A = \left( \frac{n}{|\alpha|} \right)^n e^{-\frac{|\alpha|^2}{2}}, \quad B = \frac{n}{|\alpha|} - |\alpha|,$$

the single-sided Crystal Ball function is expressed as follows:

$$CB(m, \mu, \sigma, \alpha, n) \propto \begin{cases} e^{-\frac{(m-\mu)^2}{2\sigma^2}}, & \text{if } \frac{m-\mu}{\sigma} > -\alpha, \\ A \left( B - \frac{m-\mu}{\sigma} \right)^{-n}, & \text{if } \frac{m-\mu}{\sigma} \leq -\alpha. \end{cases}$$

- Double-sided Hypatia function

Having defined:

$$h(m, \mu, \sigma, \lambda, \zeta, \beta) \propto \left( (m - \mu)^2 + A_\lambda(\zeta) \sigma^2 \right)^{\frac{1}{2}\lambda - \frac{1}{4}} e^{\beta(m-\mu)} K_{\lambda - \frac{1}{2}} \left( \zeta \sqrt{1 + \left( \frac{m - \mu}{A_\lambda(\zeta) \sigma} \right)^2} \right),$$

and its first derivative with respect to  $m$ ,  $h'$ , then the double-sided Hypatia function  $H$  is expressed as follows:

$$H(m, \mu, \sigma, \lambda, \zeta, \beta, a_1, n_1, a_2, n_2) \propto$$

$$\begin{cases} h(m, \mu, \sigma, \lambda, \zeta, \beta), & \text{if } \frac{m-\mu}{\sigma} > -a_1 \text{ or } \frac{m-\mu}{\sigma} < a_2, \\ \frac{h(\mu-a_1\sigma, \mu, \sigma, \lambda, \zeta, \beta)}{\left(1-m/\left(n^{\frac{h(\mu-a_1\sigma, \mu, \sigma, \lambda, \zeta, \beta)}{h'(\mu-a_1\sigma, \mu, \sigma, \lambda, \zeta, \beta)}-a_1\sigma}\right)\right)^{n_1}}, & \text{if } \frac{m-\mu}{\sigma} \leq -a_1, \\ \frac{h(\mu-a_2\sigma, \mu, \sigma, \lambda, \zeta, \beta)}{\left(1-m/\left(n^{\frac{h(\mu-a_2\sigma, \mu, \sigma, \lambda, \zeta, \beta)}{h'(\mu-a_2\sigma, \mu, \sigma, \lambda, \zeta, \beta)}-a_2\sigma}\right)\right)^{n_2}}, & \text{if } \frac{m-\mu}{\sigma} \geq a_2. \end{cases}$$

The  $K_\lambda$  functions are special Bessel functions of third kind, whereas  $A_\lambda$  is defined as:

$$A_\lambda^2 = \frac{\zeta K_\lambda(\zeta)}{K_{\lambda+1}(\zeta)}.$$

703     • **Single-sided Hypatia function**

704     A single-sided Hypatia function is obtained from a double-sided Hypatia function  
705     in the limit  $a_2 \rightarrow +\infty$ ,  $n_2 = 0$  (and by labelling  $a_1$  and  $n_1$  as  $a$  and  $n$  respectively).

• **Johnson SU function**

Having defined the following parameters:

$$w = e^{\tau^2}$$

$$\omega = -\nu\tau,$$

$$c = \frac{1}{\sqrt{\frac{1}{2}(w-1)(w \cosh 2\omega + 1)}},$$

$$z = \frac{m - (\mu + c + \sigma\sqrt{w} \sinh \omega)}{c\sigma},$$

$$r = -\nu + \frac{\sinh^{-1} z}{\tau},$$

the Johnson SU function is expressed as follows:

$$J(m, \mu, \sigma, \nu, \tau) \propto \frac{1}{2\pi c(\nu, \tau)\sigma} e^{-\frac{1}{2}r(m, \mu, \sigma, \nu, \tau)^2} \frac{1}{\tau\sqrt{z(m, \mu, \sigma, \nu, \tau)^2 + 1}}.$$



# Bibliography

- 707 [1] A. Salam, *Weak and electromagnetic interactions*, Proceedings of the 8th Nobel Sym-  
708 posium on Elementary particle theory, relativistic groups and analyticity, Stockholm,  
709 Sweden (1968).
- 710 [2] S. Weinberg, *A model of leptons*, Phys. Rev. Lett. **19** (1968) 1264.
- 711 [3] S. L. Glashow, *Partial symmetries of weak interactions*, Nucl. Phys. **22** (1961) 579.
- 712 [4] E. Fermi, *Sulla quantizzazione del gas perfetto monoatomico*, Rendiconti Lincei **3**  
713 (1926) 145.
- 714 [5] P. A. M. Dirac, *On the Theory of Quantum Mechanics*, Proceedings of the Royal  
715 Society A. **112** (**762**) (1926) 661.
- 716 [6] S. Bose, *Plancks Gesetz und Lichtquantenhypothese*, Zeitschrift für Physik **26** (1924)  
717 178.
- 718 [7] LHCb collaboration, R. Aaij *et al.*, *Observation of the resonant character of the*  
719 *Z(4430)<sup>-</sup> state*, Phys. Rev. Lett. **112** (2014) 222002, [arXiv:1404.1903](https://arxiv.org/abs/1404.1903).
- 720 [8] LHCb collaboration, R. Aaij *et al.*, *Observation of J/ψ p resonances consistent with*  
721 *pentaquark states in Λ\_b^0 → J/ψ p K^- decays*, Phys. Rev. Lett. **115** (2015) 072001,  
722 [arXiv:1507.03414](https://arxiv.org/abs/1507.03414).
- 723 [9] F. Englert and R. Brout, *Broken Symmetry and the Mass of Gauge Vector Bosons*,  
724 Phys. Rev. Lett. **13** (1964) 321.
- 725 [10] P. Higgs, *Broken Symmetries and the Masses of Gauge Bosons*, Phys. Rev. Lett. **13**  
726 (1964) 508.
- 727 [11] G. S. Guralnik, C. R. Hagen, and T. W. B. Kibble, *Global Conservation Laws and*  
728 *Massless Particles*, Phys. Rev. Lett. **13** (1964) 585.
- 729 [12] The ATLAS collaboration, *Observation of a new particle in the search for the*  
730 *Standard Model Higgs boson with the ATLAS detector at the LHC*, Phys. Lett. B  
731 **716** (2012) 1.

## Bibliography

---

- 732 [13] The CMS collaboration, *Observation of a new boson at a mass of 125 GeV with the*  
733 *CMS experiment at the LHC*, Phys. Lett. B **716** (2012) 30.
- 734 [14] N. Cabibbo, *Unitary symmetry and leptonic decays*, Phys. Rev. Lett. **178** (1963)  
735 531.
- 736 [15] M. Kobayashi and T. Maskawa, *CP violation in the Renormalizable Theory of Weak*  
737 *Interaction*, Progr. Theor. Phys. **49** (1973) 652.
- 738 [16] L. L. Chau and W. Y. Keung, *Comments on the Parametrization of the Kobayashi-*  
739 *Maskawa Matrix*, Phys. Rev. Lett. **53** (1984) 1802.
- 740 [17] L. Wolfenstein, *Parametrization of the Kobayashi-Maskawa matrix*, Progr. Theor.  
741 Phys. **49** (1973) 652.
- 742 [18] CKMfitter group, J. Charles *et al.*, *CP Violation and the CKM Matrix: Assessing*  
743 *the Impact of the Asymmetric B Factories*, Eur. Phys. J. **C41** (2005) 1,  
744 updated results and plots available at <http://ckmfitter.in2p3.fr>.
- 745 [19] Particle Data Group, C. Patrignani *et al.*, *Review of Particle Physics*, Chin. Phys. C.  
746 **C40** (2016) 100001.
- 747 [20] I. Bigi and A. I. Sanda, *CP Violation*, Cambridge Monographs on Particle Physics,  
748 Nuclear Physics and Cosmology, 2009.
- 749 [21] LHCb collaboration, R. Aaij *et al.*, *LHCb detector performance*, Int. J. Mod. Phys.  
750 **A30** (2015) 1530022.
- 751 [22] R. Aaij *et al.*, *Performance of the LHCb Vertex Locator*, JINST **9** (2014) P09007.
- 752 [23] LHCb collaboration, R. Antunes Nobrega *et al.*, *LHCb reoptimized detector design and*  
753 *performance: Technical Design Report*, CERN-LHCC-2003-030. LHCb-TDR-009.
- 754 [24] LHCb collaboration, A. Franca Barbosa *et al.*, *LHCb inner tracker: Technical Design*  
755 *Report*, CERN-LHCC-2002-029. LHCb-TDR-008.
- 756 [25] LHCb collaboration, P. R. Barbosa Marinho *et al.*, *LHCb outer tracker: Technical*  
757 *Design Report*, CERN-LHCC-2001-024. LHCb-TDR-006.
- 758 [26] A. Powell *et al.*, *Particle identification at LHCb*, Proceedings of ICHEP2010 **020**  
759 (2010), LHCb-PROC-2011-008.
- 760 [27] LHCb collaboration, S. Amato *et al.*, *LHCb calorimeters: Technical Design Report*,  
761 CERN-LHCC-2000-036.
- 762 [28] A. A. Alves Jr *et al.*, *Performance of the LHCb muon system*, JINST **8** (2013)  
763 P02022.

- 764 [29] LHCb collaboration, R. Antunes Nobrega *et al.*, *LHCb trigger system: Technical*
- 765 *Design Report*, CERN-LHCC-2003-031.
- 766 [30] S. Torbjörn *et al.*, *An Introduction to PYTHIA 8.2*, Comput. Phys. Commun. **191**
- 767 (2015) 159.
- 768 [31] D. J. Lange, *The EvtGen particle decay simulation package*, Nucl. Instrum. Meth.
- 769 **A462** (2001) 152.
- 770 [32] P. Golonka and Z. Was, *PHOTOS Monte Carlo: a precision tool for QED corrections*
- 771 *in Z and W decays*, Eur. Phys. J. **C45** (2006) 97.
- 772 [33] S. Agostinelli *et al.*, *Geant4: a simulation toolkit*, Nucl. Instrum. Meth. **A506** (2003)
- 773 250.
- 774 [34] I. Dunietz and R. G. Sachs, *Asymmetry between inclusive charmed and anticharmed*
- 775 *modes in  $B^0, \bar{B}^0$  decay as a measure of CP violation*, Phys. Rev. **D37** (1988) 3186.
- 776 [35] R. Aleksan, I. Dunietz, and B. Kayser, *Determining the CP violating phase gamma*,  
Z Phys. **C54** (1992) 653.
- 777 [36] R. Fleischer, *New strategies to obtain insights into CP violation through  $B_{(s)} \rightarrow$*   
 *$D_{(s)}^\pm K^\mp, D_{(s)}^{*\pm} K^\mp, \dots$  and  $B_{(d)} \rightarrow D^\pm \pi^\mp, D^{*\pm} \pi^\mp, \dots$  decays*, Nucl. Phys. **B671**
- 778 (2003) 459.
- 779 [37] LHCb collaboration, R. Aaij *et al.*, *Measurement of the time-dependent CP asymme-*
- 780 *tries in  $B_s^0 \rightarrow J/\psi K_s^0$* , JHEP **06** (2015) 131, [arXiv:1503.07055](https://arxiv.org/abs/1503.07055).
- 781 [38] BaBar collaboration, B. Aubert *et al.*, *Measurement of the Branching Fractions of*
- 782 *the Rare Decays  $B^0 \rightarrow D_s^{*+} \pi^-$ ,  $B^0 \rightarrow D_s^{*+} \rho^-$ , and  $B^0 \rightarrow D_s^{*-} K^{*+}$* , Phys. Rev.
- 783 **D78** (2008) 032005.
- 784 [39] Belle collaboration, A. Das *et al.*, *Measurements of Branching Fractions for  $B^0 \rightarrow$*   
 *$D_s^+ \pi^-$  and  $\bar{B}^0 \rightarrow D_s^+ K^-$* , Phys. Rev. **D82** (2010) 051103.
- 785 [40] BaBar collaboration, B. Aubert *et al.*, *Measurement of time-dependent CP-violating*
- 786 *asymmetries and constraints on  $\sin(2\beta + \gamma)$  with partial reconstruction of  $B \rightarrow D^{*\mp} \pi^\pm$*
- 787 *decays*, Phys. Rev. **D71** (2005) 112003.
- 788 [41] BaBar collaboration, B. Aubert *et al.*, *Measurement of time-dependent CP asymme-*
- 789 *tries in  $B^0 \rightarrow D^{*\pm} \pi^\mp$  and  $B^0 \rightarrow D^\pm \rho^\mp$  decays*, Phys. Rev. **D76** (2006) 111101.
- 790 [42] Belle collaboration, F. J. Ronga *et al.*, *Measurement of CP violation in  $B^0 \rightarrow D^{*-} \pi^+$*
- 791 *and  $B^0 \rightarrow D^- \pi^+$  decays*, Phys. Rev. **D73** (2006) 092003.
- 792 [43] Belle collaboration, S. Bahinipati *et al.*, *Measurements of time-dependent CP asym-*
- 793 *metries in  $B^0 \rightarrow D^{*\mp} \pi^\pm$  decays using a partial reconstruction technique*, Phys. Rev.
- 794 **D84** (2011) 021101.

## Bibliography

---

- 798 [44] LHCb collaboration, R. Aaij *et al.*, *Measurement of CP asymmetry in  $B_s^0 \rightarrow D_s^\mp K^\pm$  decays*, JHEP **11** (2014) 060.
- 800 [45] L. Breiman, *Bagging Predictors*, Machine Learning **24** (1996) 123.
- 801 [46] LHCb collaboration, *A single track HLT1 trigger*, LHCb-PUB-2011-003.
- 802 [47] LHCb collaboration, *The LHCb inclusive B triggers*, LHCb-INT-2011-030.
- 803 [48] W. D. Hulsbergen *et al.*, *Decay chain fitting with a Kalman filter*, Nucl. Instrum. Meth. (2005), no. A552 566.
- 804 [49] P. Koppenburg, *Dealing with Multiple Candidates*, .
- 805 [50] L. Breiman, J. H. Friedman, R. A. Olshen, and C. J. Stone, *Classification and regression trees*, Wadsworth international group, Belmont, California, USA, 1984.
- 806 [51] B. P. Roe *et al.*, *Boosted decision trees as an alternative to artificial neural networks for particle identification*, Nucl. Instrum. Meth. **A543** (2005) 577, arXiv:physics/0408124.
- 807 [52] A. Hoecker *et al.*, *TMVA: Toolkit for Multivariate Data Analysis*, PoS **ACAT** (2007) 040, arXiv:physics/0703039.
- 808 [53] R. E. Schapire and Y. Freund, *A decision-theoretic generalization of on-line learning and an application to boosting*, Jour. Comp. and Syst. Sc. **55** (1997) 119.
- 809 [54] M. Pivk and F. R. L. Diberder, *sPlot: a statistical tool to unfold data distributions*, Nucl. Instrum. Meth. **A555** (2005) 356.
- 810 [55] D. M. Santos and F. Dupertuis, *Mass distributions marginalized over per-event errors*, Nucl. Instrum. Meth. (2014), no. A764 150.
- 811 [56] N. L. Johnson, *Systems of Frequency Curves Generated by Methods of Translation*, Biometrika (1949), no. 36 149.
- 812 [57] T. Skwarnicki, *A study of the radiative cascade transitions between the Upsilon-prime and Upsilon resonances*, PhD thesis, Institute of Nuclear Physics, Krakow, 1986, DESY-F31-86-02.